

Diss. ETH No. 19916

Tensor network states

A dissertation submitted to

ETH ZURICH

for the degree of
Doctor of Sciences

presented by

Roman Bela Bauer

Dipl. Phys. ETH
16.07.1984
citizen of
Germany

accepted on the recommendation of
Prof. Dr. M. Troyer, examiner
Prof. Dr. F. Verstraete, co-examiner

2011

Cover picture by courtesy of M. Dolfi.

Abstract

Emergent phenomena of interacting quantum many-body systems arguably pose some of the greatest challenges to modern theoretical physics. Many of these systems are characterized by drastic changes in their properties as they are driven into a regime where quantum effects and interactions become relevant. Examples are the fractional quantum Hall effect and high-temperature superconductors, to name just two. New theoretical tools are necessary to study such systems, as even simple model Hamiltonians are not fully understood after decades of intense research. Numerical simulations are emerging as an indispensable tool alongside more traditional analytic approaches and have seen immense progress in recent years.

In this thesis, we study tensor network states, a new class of numerical methods that have been developed in recent years drawing on insights from quantum information theory. Combining renormalization group methods with knowledge about the entanglement structure of ground states of quantum systems, tensor network states aim to efficiently describe ground states of strongly correlated quantum systems.

Center stage is taken by the *projected entangled-pair states*. This ansatz for two-dimensional systems is discussed in detail and its capabilities are assessed by comparison to established methods and by exploring a frustrated system. We then develop a general formalism to exploit Abelian symmetries in a tensor network algorithm and demonstrate its application to projected entangled-pair states.

A large part of this thesis is devoted to the discussion of a class of supersymmetric models for interacting lattice fermions. After introducing the concept of supersymmetry in quantum mechanics and an extensive overview of conformal field theory and its relation to numerical simulations, we study the critical theory of the supersymmetric model on the square ladder. We use two tensor network state algorithms, the *density-matrix renormalization group* and *multi-scale entanglement renormalization* along with exact diagonalization to explore this challenging system.

In the final two chapters, we discuss two applications of tensor network states, namely simulations of the $SU(3)$ Heisenberg model in two dimensions using two different tensor network state algorithms with the goal of illuminating the nature of its ground state, and the indistinguishability, a measure to detect phase transitions and classify wave functions which is particularly suitable for calculations based on tensor network states.

Zusammenfassung

Das Verhalten wechselwirkender Quantenvielteilchensysteme stellt eine der größten Herausforderungen an die moderne theoretische Physik dar. In Bereichen, in denen Quanteneffekte sowie Wechselwirkungen relevant werden, ändern sich die makroskopischen Eigenschaften solcher Systeme oft drastisch. Zwei Beispiele sind der fraktionale Quanten-Hall-Effekt sowie Hochtemperatur-Supraleitung. Neue theoretische Zugänge sind nötig, um diese Systeme zu verstehen, da selbst einfache Modellsysteme auch nach Jahrzehnten intensiver Forschung nicht vollständig verstanden sind. Numerische Simulationen stellen sich zunehmend als unverzichtbares Verfahren neben den traditionellen analytischen Zugängen heraus, insbesondere da in den letzten Jahren rapide Fortschritte in diesen Methoden erreicht wurden.

In der vorliegenden Arbeit werden Tensornetzwerkzustände diskutiert, welche in den letzten Jahren insbesondere aus der Quanteninformationstheorie heraus entstanden sind. In diesen numerischen Verfahren werden Renormierungsgruppenmethoden mit Einsichten in die Verschränkung in Quantensystemen kombiniert, um effiziente Ansatzzustände für die Grundzustände stark korrelierter Quantensysteme zu erhalten.

Im Mittelpunkt der Arbeit stehen die sogenannten Projected Entangled-Pair States (PEPS). Dieser Ansatz für zweidimensionale Systeme wird detailliert vorgestellt, und anhand von Vergleichen mit etablierten Verfahren werden Genauigkeit und Anwendbarkeit eingeschätzt. Weiterhin entwickeln wir einen sehr allgemeinen Formalismus, um abelsche Symmetrien in Tensornetzwerken zu verwenden. Als Anwendungsbeispiel wird der Formalismus in PEPS eingeführt.

Einen weiteren Schwerpunkt bildet eine Klasse von supersymmetrischen Modellen für wechselwirkende Gitterfermionen. Zunächst werden Supersymmetrie in nicht-relativistischer Quantenmechanik sowie konforme Feldtheorie eingeführt, wobei besonders auf die Berührungspunkte zwischen numerischen Rechnungen und konformer Feldtheorie eingegangen wird. Zur Untersuchung der kritischen Theorie des Modells auf einem Leitergitter werden zwei Tensornetzwerkmethoden, Matrix-Product States (MPS) und Multi-Scale Entanglement Renormalization Ansatz (MERA), mit exakter Diagonalisierung kombiniert.

In den letzten Kapiteln werden zwei Anwendungen von Tensornetzwerkzuständen diskutiert: zum einen Simulationen des $SU(3)$ -Heisenberg-Modells in zwei Dimensionen, dessen Grundzustand durch die Kombination zweier Tensornetzwerkmethoden charakterisiert wird, und zum anderen die Ununterscheidbarkeit, welche zur Identifizierung von Phasenübergängen sowie zur Klassifizierung von Wellenfunktionen dient.

Contents

Contents	vii
1 Introduction	1
1.1 Some insights from quantum information theory	2
1.1.1 Exponential scaling of naive approaches	3
1.1.2 Ground state entanglement and area laws	4
1.1.3 Hardness results	7
1.2 Renormalization group	8
1.2.1 Real-space renormalization	9
1.2.2 Choosing the RG transformation	10
1.3 Outline	12
2 Tensor network states	13
2.1 Matrix-product states	14
2.1.1 Variational optimization of matrix-product states	19
2.1.2 Time evolution	21
2.1.3 Infinite matrix-product states	24
2.2 Projected entangled-pair states	26
2.2.1 Contraction of PEPS	28
2.2.2 Optimization of PEPS	29
2.3 Multi-scale entanglement renormalization	35
2.3.1 Superoperators	39
2.3.2 Optimization of a MERA	40
2.4 Fermionic tensor networks	42
2.5 Complete-graph tensor network states	46
3 Symmetries in tensor network states	49
3.1 Symmetry groups	50
3.1.1 Charge calculus	50
3.1.2 Examples	51
3.2 Symmetric tensor networks	53

3.2.1	Definition and contraction of symmetric tensors	53
3.2.2	Tensor contraction	54
3.2.3	Symmetric PEPS	56
3.3	Some proofs	59
4	Implementation of tensor network states	61
4.1	Requirements	61
4.2	Symmetries	62
4.3	Interface	63
4.3.1	Identifying indices	63
4.3.2	Defining tensors	63
4.3.3	Specifying contractions	66
4.3.4	Matrix operations	66
5	The accuracy of projected entangled-pair states	69
5.1	Non-frustrated spin systems	70
5.1.1	XXZ model in external field	71
5.1.2	The spin-flop transition: iPEPS at a first-order phase transition	73
5.1.3	Heisenberg and XY model	75
5.1.4	Dimerized Heisenberg model	77
5.2	Frustrated XY Models	79
5.3	The accuracy in the presence of symmetries	82
5.3.1	Finite groups	83
5.3.2	U(1)	84
6	Supersymmetric lattice fermions	87
6.1	Supersymmetric lattice fermions	88
6.1.1	A single-particle example: the supersymmetric harmonic oscillator	88
6.1.2	A many-particle model	90
6.2	Conformal field theory	91
6.2.1	Conformal symmetry in two dimensions	92
6.2.2	Minimal models	94
6.2.3	Relation to finite systems	95
6.2.4	Conformal field theory and entropy	97
6.2.5	Relation to the MERA	99
6.3	Chain	100
6.3.1	Entropy	101
6.3.2	MERA	107
6.4	Square ladder	109

6.4.1	Entropy	110
6.4.2	Finite-size spectra	111
6.4.3	Density	115
6.4.4	MERA results	117
7	The SU(3) Heisenberg model	121
7.1	The model	121
7.2	Methods	123
7.3	Results	125
7.3.1	Boundary conditions and pinning fields	125
7.3.2	Energy and local moment	128
8	Indistinguishability	133
8.1	Indistinguishability	134
8.1.1	Quantum Chernoff bound	135
8.1.2	Calculating I using matrix-product states	135
8.2	Indistinguishability for quantum phase transitions	137
8.2.1	Ising chain in transverse field	137
8.2.2	Spin-1 bilinear-biquadratic chain	140
8.3	Indistinguishability in the Toric Code	145
8.3.1	Review of the Toric Code	145
8.3.2	Computed Indistinguishability	145
9	Conclusion and outlook	149
9.1	Projected entangled-pair states	149
9.2	Supersymmetric lattice fermions	151
9.3	The SU(3) Heisenberg model	152
9.4	Indistinguishability	152
	List of publications	155
	Bibliography	157
	Curriculum Vitae	175
	Acknowledgements	177

CONTENTS

Chapter 1

Introduction

There are many examples of systems that undergo a drastic change in macroscopic properties due to effects of low temperature and interactions. A prime example is the fractional Quantum Hall effect discovered in 1982 [10]. The influence of this remarkable discovery on condensed matter theory can hardly be overestimated, as it has extended the traditional understanding of phase transitions based on Landau's symmetry breaking theory and lead to the development of a completely new class of theories evolving around topological order [11]. Interestingly, numerical simulations were an essential part already of the first theoretical developments in this area [12].

Another discovery of arguably even greater influence is high- T_c superconductivity in cuprates [13]. Effective models for cuprate superconductors, like the Hubbard model, were proposed very quickly after the experimental discovery [14] – but to this date, it is neither clear whether these models are appropriate, nor has their phase diagram been fully understood. Nonetheless, their investigation has triggered many developments in computational and analytical methods for interacting fermion systems.

These are just two out of a growing body of problems where conventional approaches such as effective single-particle theories fail. Consequently, numerical approaches are receiving more and more attention and have seen rapid progress in recent years. Examples include path-integral quantum Monte Carlo methods, which are an essential part in understanding experiments performed on cold atomic gases, time-dependent density matrix renormalization group calculations, which are central to understanding thermalization in open quantum systems, and dynamical mean-field theory, which, in particular when used in conjunction with density functional theory, is starting to play a central role in materials science.

In this thesis, we explore a new class of numerical methods, tensor networks states, which are a recent development that draws from renormalization group theory and quantum information theory to develop efficient ansatz states for the

ground states of strongly correlated quantum systems in one and higher dimensions. One example of a tensor network state algorithm, the density matrix renormalization group (DMRG), is a well-established method for studying the ground states of one-dimensional and quasi-one-dimensional systems. Since it was first developed by White in 1992 [15], it has been applied in many different contexts and has seen many extensions, for example to time evolution and thermal systems. DMRG will serve as starting point of our discussion of tensor network states.

The first proposal of a tensor network state to receive widespread attention were projected entangled-pair states [16]. Many other tensor network states have been proposed since, for example tree tensor networks [17], multi-scale entanglement renormalization [18, 19], string-bond states [20], scale-renormalized matrix product states [21], entangled plaquette states [22], correlator product states [23], graph-enhanced tensor network states [24], concatenated tensor network states [25], and plaquette renormalized states [26].

While the theoretical foundations for DMRG are well-understood, this is not the case in higher dimensions. We therefore have to resort to numerical calculations to confirm the validity of these approaches. A first focus of this thesis is therefore to assess the accuracy of projected entangled-pair states by comparison against established methods for a number of systems. Another important aspect of this thesis are applications of tensor network states. A large part of this work is devoted to a class of interacting fermion models on one- and quasi-one-dimensional lattices, which are studied using two tensor network states, the multi-scale entanglement renormalization ansatz and matrix-product states.

A detailed overview of this thesis is given in Section 1.3. In the following section, we will illustrate some concepts of quantum information theory and renormalization group theory that will naturally lead to matrix-product states, the simplest example of a tensor network state.

1.1 Some insights from quantum information theory

A plethora of numerical methods exist for the simulation of quantum many-body systems and it is beyond the scope of this introduction to list them. To this date, however, no method has been found that allows the numerically exact¹ simulation of generic quantum many-body systems with a classical computer, where the amount of resources needed scales only with a polynomial of the number of degrees of freedom. All known methods are either based on some approximation, limited

¹By this we mean that errors can in principle be reduced to the numerical accuracy of floating-point calculations on a computer.

to certain classes of problems or become prohibitively expensive for a large number of degrees of freedom.

Understanding the origin of this limitation, and deciding whether it is of fundamental nature or just a result of our inability to devise a proper method, is clearly an important problem. Advances in quantum information theory have shed some light on this question; for a recent review article, see Ref. [27]. Some of these ideas have been influential to the development of tensor network states as effective representations of quantum many-body systems.

In this section, we will first survey the difficulties associated with *representing* the state of a quantum system on a classical computer. Some methods, such as Path Integral Quantum Monte Carlo, do not even attempt to represent the state (or possibly density matrix) of a system, but instead aim to calculate only the expectation values of specific observables by sampling, e.g., the partition function of the system. While being free of systematic errors for some systems, these methods become prohibitively expensive for a wide range of systems due to the infamous *sign problem*. The origin of this limitation is not related in an obvious way to the difficulties of representing states of quantum systems discussed below. In fact, it has been shown to be intimately related to difficulties also present in the simulation of classical systems [28] — in these systems, representing the ground state is trivial, but finding it for a given Hamiltonian is an unsolved problem.

1.1.1 Exponential scaling of naive approaches

The state of a classical system can always be stored with an amount of memory that is proportional to the number of degrees of freedom of that system, although the number of possible states may be exponentially large. Consider, for example, a classical Ising system on a lattice, where with each site i of the lattice, a spin variable $\sigma_i \in \{0, 1\}$ is associated. The number of possible states for this system is 2^N , where N is the total number of sites, but to represent the state of such a system on a classical computer, only N bits have to be stored.

Consider now the case of a quantum Ising model on the same lattice. It is the nature of a quantum system that it can be in a superposition of states, that is, its state can be the linear combination of any number of the classical states. Therefore, to fully describe a quantum state, the coefficients for all 2^N classical states have to be stored. The space of such states forms a Hilbert space, with the states of the classical Ising system as one possible choice of basis.

The most straightforward approach to numerically solve a quantum system is to fully enumerate the basis of the system, express the Hamiltonian of the system in this basis, and diagonalize it numerically. While being the only numerical method that can always be applied, it is of course limited to a very small number of degrees of freedom in the system, so that gaining insights into the behavior of the system

in the thermodynamic limit is extremely difficult.

1.1.2 Ground state entanglement and area laws

An important question is whether the ground state of a realistic Hamiltonian will actually explore all of its exponentially large Hilbert space — in other words, how far away from a classical state will such a ground state be? A common measure to quantify the "quantumness" of a system is the entanglement entropy. Consider a system, \mathcal{C} , which is split into two subsystems \mathcal{A}, \mathcal{B} , such that $\mathcal{A} \cup \mathcal{B} = \mathcal{C}$. Let the state of the full system be described by a pure state $|\psi\rangle$. We can form reduced density matrices for each subsystem,

$$\rho_{\mathcal{A}} = \text{Tr}_{\mathcal{B}}|\psi\rangle\langle\psi| \tag{1.1}$$

$$\rho_{\mathcal{B}} = \text{Tr}_{\mathcal{A}}|\psi\rangle\langle\psi|. \tag{1.2}$$

These encode the full information about each subsystem, in the sense that the expectation value of an operator $O_{\mathcal{A}}$ ($O_{\mathcal{B}}$) that has support only in \mathcal{A} (\mathcal{B}) can be calculated as $\langle O_{\mathcal{A}} \rangle = \text{Tr}\rho_{\mathcal{A}}O_{\mathcal{A}}$ ($\langle O_{\mathcal{B}} \rangle = \text{Tr}\rho_{\mathcal{B}}O_{\mathcal{B}}$). It can be shown that these reduced density matrices have the same spectrum λ_{α} , and that the state of the full system can be written as

$$|\psi\rangle = \sum_{\alpha} \lambda_{\alpha}|u_{\alpha}\rangle|v_{\alpha}\rangle, \tag{1.3}$$

where $|u_{\alpha}\rangle$ and $|v_{\alpha}\rangle$ are the eigenvectors of $\rho_{\mathcal{A}}$ and $\rho_{\mathcal{B}}$, respectively. This is known as the Schmidt decomposition.

If the state of the full system is a classical state, only one of the coefficients λ_{α} will be nonvanishing. In the other limit, if all the basis states contribute equally to the wavefunction of the whole system, the number of relevant coefficients will grow exponentially with the size of the subsystems. To quantify where a given state is found in between these two extremal cases, the entanglement entropy, given by

$$S_1 = - \sum_{\alpha} \lambda_{\alpha} \log \lambda_{\alpha} \tag{1.4}$$

is used. Evidently, it is 0 for a classical state and $\log N$ in the case where all N possible basis state give an equal contribution. The maximum entropy that a system can have therefore grows with the system's volume, as one would expect from the analogy to the (extensive) thermodynamic entropy.

As we will see below, most physical systems do not exploit the maximum amount of entropy; instead, the entropy is bounded by a constant or grows much weaker than the volume. Studying how the entanglement entropy grows with system size may give an intuition about how much of the Hilbert space is exploited, and in some cases establish a connection to the simulability of the system. This

field has received a significant amount of attention in recent years. A good overview is given in Ref. [29]; in the following, we will first discuss some key results about the entanglement entropy and then discuss their relation to simulability in the next section.

One dimension

In one dimension, several strong results for the scaling of entanglement entropy have led to a classification of physically reasonable systems into two scenarios, namely i) gapless systems where the entropy diverges with the system size and ii) gapped systems where the entropy is bounded by a constant. Few exceptions are known; for an example of a local Hamiltonian that has a volume law, see Ref. [30]. This classification was first obtained by Vidal et al [31], who numerically studied a one-dimensional system close to a critical point and found that the entropy as a function of system size saturates away from criticality, while diverging at criticality. More rigorously, Hastings [32] has shown that the entropy in the ground state of a local Hamiltonian in one dimension has a bound that is related only to the correlation length and not the size of the system.

This saturation of the entanglement entropy is commonly referred to as *area law* or *boundary law*; the origin of this terminology will become clear when considering higher-dimensional systems. The existence of such an area law for a huge class of systems is at the heart of the *density matrix renormalization group* algorithm, which will be studied in some detail in this thesis.

The divergence of the entanglement entropy for critical one-dimensional systems can be related to results from conformal field theory [33, 34]. These calculations show that asymptotically, the entropy in the center of an open spin chain scales as

$$S(L) = \frac{c}{6} \log L. \quad (1.5)$$

Here, c denotes the central charge of the conformal field theory that describes the critical point. As we will see in Chapter 6, this formula is extremely useful in determining the central charge from entropies for finite-size systems.

Higher dimensions

In higher dimensions, the situation is more complicated. The question that is commonly asked is how the entropy between two subsystems scales with the area of the boundary and the volume of the two blocks. For an illustration, consider Fig. 1.1: If an *area law* or *boundary law* is present, the entanglement entropy should be purely a function of L — as opposed to a scaling in L and W , as one might naively expect.

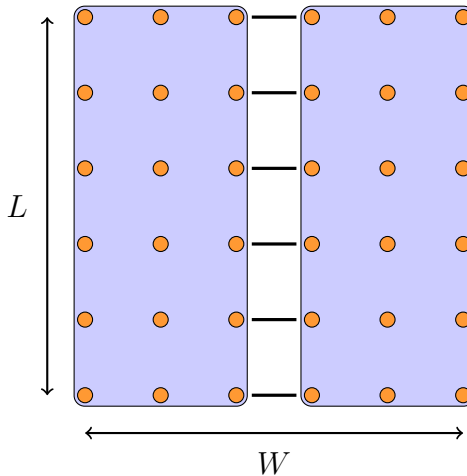


Figure 1.1: In this example of a two-dimensional system, an area law would be present if $S \sim L$. Naively, one could expect a scaling $S \sim L \cdot W$.

The existence of an area law for all gapped two-dimensional systems has been conjectured, but a general proof, like the one given by Hastings for one-dimensional systems, has not been found. Furthermore, the inverse, i.e. that a gapless system will in general violate the area law, is not true.

Strong results exist for non-critical harmonic (i.e., bosonic systems whose interactions are quadratic in canonical coordinates) lattice systems [35], where an area law holds. Fermions present a more complicated case: Wolf [36] was able to relate the presence of an area law in quasi-free (quadratic) fermionic systems to the volume of the Fermi surface. If the Fermi surface has a finite volume,

$$S \sim L \log L \tag{1.6}$$

is found, whereas an area law holds in the cases where the Fermi surface has vanishing volume. For free fermions, the existence of an area law therefore depends on the lattice: on a two-dimensional square lattice, the area law would be violated, while for the honeycomb lattice, an area law holds.

For more general interactions, the case is still unclear. The case of gapless anti-ferromagnetic spin systems, such as the paradigmatic spin- $\frac{1}{2}$ Heisenberg model, has been under debate recently. While these systems can be studied to high accuracy using Monte Carlo simulations, the entanglement entropy is difficult to extract from such simulations. The valence bond entanglement entropy was put forward in Ref. [37] as a quantity that could be extracted from Quantum Monte Carlo simulations and that should give some insight into the behavior of the standard entanglement entropy; based on this, Ref. [38] argued that gapless antiferromagnets show a logarithmic correction to the area law, similar to the case of fermions

with a finite Fermi surface. More recent results [39], which employ both Quantum Monte Carlo and the Density Matrix Renormalization Group algorithm (which allows a direct calculation of the entanglement entropy) challenge this result and strongly indicate the presence of an area law without corrections.

1.1.3 Hardness results

In light of the above discussions, one realizes that the states which are actually realized as ground states of local Hamiltonians explore only a small subset of the full Hilbert space, namely that of low-entanglement states, which in some sense are close to classical states. This may lead to some optimism about the possibility to represent such states on a classical computer: maybe it is not as hopeless as the naive picture of an exponentially growing Hilbert space suggests?

Obtaining rigorous statements about this has been a challenging topic in quantum information in the last few years and so far, only the situation in one dimension has been resolved to a certain extent. It was generally believed that for gapped one-dimensional states, a good approximation in terms of a so-called *matrix-product state*, which would have only polynomially many parameters, can be found. A recent proof showed that this holds for states that have an area law for the von Neumann entropy and for certain Renyi entropies [40]. This is a slightly tighter condition, which however is met for many systems of interest.

This result has strong implications for the simulation of one-dimensional quantum systems: it proves the ground states of gapped one-dimensional systems can be efficiently represented on a classical computer! For these systems, the exponential amount of memory required to store the state using naive approaches is merely an artefact of working in the wrong representation of the state – and a better representation is known, the matrix-product state, which will be discussed in the next section. Of course, we have only discussed the question of representing the ground state of such a system – the question of whether the optimal state within the class of matrix-product states can be found must be answered separately [41, 42]. One of the big open questions is how to obtain similar results in higher dimensions.

There exist also a number of systems which have been proven to be hard even for quantum computers; more precisely, finding their ground state has been shown to be hard for Quantum Merlin Arthur (QMA). QMA is an important complexity class in the field of quantum complexity and can be regarded as quantum generalization of the well-known NP complexity class.² After a seminal work by

²Some colloquial definitions: NP is the class of all problems where a potential solution can be verified in polynomial time. MA is the class of problems where a proper solution will be accepted in polynomial time with probability $2/3$, and a wrong solution will be accepted with probability at most $1/3$. QMA is the extension of this to solutions given as quantum states, and verifiers that are quantum circuits that run in polynomial time. Being complete for one of these classes

Kitaev [43], hardness has been shown for a number of systems. Physically relevant examples include fermions with Coulomb interaction [44] and local spin Hamiltonians [45, 46]³; recently, it has been shown even for a translationally invariant one-dimensional system [47]. For these systems, we cannot expect to find an efficient classical algorithm to solve all instances; nevertheless, it may be possible to obtain reasonable and generic approximation schemes for most instances.

1.2 Renormalization group

The Density Matrix Renormalization Group Method (DMRG) was invented in 1992 by Steve White [15]. At the time, the relation to entanglement was not realized; instead, it was mainly regarded as an improvement over Wilson’s Numerical Renormalization Group scheme [48]. The problems encountered in this method were described by White and Noack in the same year [49]; a pedagogical overview is also given in Ref. [50].

Traditionally, renormalization group (RG) has been applied in the context of critical systems. The most intriguing feature of such systems is universality, i.e. that the behavior of macroscopic parameters of the system can be characterized by a *universality class*, which encompasses many different microscopic realizations. Within a certain range of parameters, the microscopic details of the Hamiltonian do not affect the behavior of macroscopic observables near the critical point. Renormalization group has been the first method that allowed a quantitative explanation of the phenomenon of universality.

While there are many different RG schemes, they have in common that local degrees of freedom are being integrated over to obtain an effective description in terms of fewer variables. Usually, this RG transformation is iterated to obtain a description of macroscopic features of the system. In a critical system, there is no characteristic length scale; in particular, fluctuations occur on all length scales. It can be expected that after integrating over the microscopic details of such a system by means of an RG transformation, further iterations of the RG procedure will not change the description of the system fundamentally — the system can be described by a fixed point of the RG transformation. Different universality classes correspond to different fixed points of the RG transformation.

At the heart of such a renormalization group procedure is the definition of the RG transformation which maps the original system to a system with fewer degrees of freedom. Examples include Wilson’s real-space renormalization group procedure, which became famous by its successful application to the Kondo problem, and the Kadanoff block spin transformation, which can be applied to the

means that if that problem can be solved, all other problems in the class can be solved.

³Note that the notion of locality in Ref. [45] is not the geometric locality one would expect.

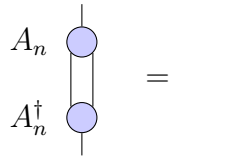


Figure 1.2: Illustration of an isometry $A_n : \mathcal{H}_A \otimes \mathcal{H}_B \rightarrow \tilde{\mathcal{H}}$ acting on two Hilbert spaces. These isometries are the building block for the RG procedure described in Section 1.2 and shown in Fig. 1.3.

two-dimensional (classical) Ising model; both are discussed in detail in Ref. [48].

1.2.1 Real-space renormalization

In the following, we will rephrase real-space renormalization for a finite chain in terms of a simple tensor network state, which will lead to the definition of the class of matrix-product states. We denote the Hilbert space of site i of our original lattice as \mathcal{H}_i ; for simplicity, we will assume that $\dim \mathcal{H}_i = d$ for all i . The Hilbert space of our full system is $\mathcal{H} = \bigotimes_{i=1}^L \mathcal{H}_i$.

We can write a generic transformation acting on a set of degrees of freedom on the lattice as a unitary transformation A between two Hilbert spaces, $A : \mathcal{H} \rightarrow \tilde{\mathcal{H}}$. For a useful RG procedure, we desire $\dim \tilde{\mathcal{H}} < \dim \mathcal{H}$. In this case, the unitary transformation becomes an isometric transformation, that is a $n \times m$ matrix with orthogonal rows, where $n < m$; the defining property is that $AA^\dagger = \mathbb{1}$ (see also Fig. 1.2). To specify the RG procedure, we need to decide which part of the system we want this isometric transformation to act on in each step. We choose to have an isometry acting on the two left-most sites of a chain, reducing them to a single effective site:

$$A_1 : \mathcal{H}_1 \otimes \mathcal{H}_2 \rightarrow \mathcal{H}_1^1. \quad (1.7)$$

After the RG step, this effective site should have a Hilbert space with a dimension that meets the condition

$$\dim \mathcal{H}_1^1 \leq \dim (\mathcal{H}_1 \otimes \mathcal{H}_2). \quad (1.8)$$

The Hilbert space of the effective system after one RG step is $\mathcal{H}_1^1 \otimes \mathcal{H}_3 \otimes \dots$. We iterate this procedure with isometries

$$A_n : \mathcal{H}_1^{n-1} \otimes \mathcal{H}_{n+1} \rightarrow \mathcal{H}_1^n \quad (1.9)$$

Iteratively applying this to a chain of length L reduces the system to a single effective site after $L-1$ RG steps. By restricting the transformations to isometries,

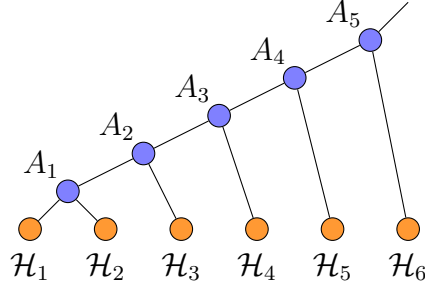


Figure 1.3: A tensor network for the renormalization of a chain of length $L = 6$. The orange circles indicate physical sites of the system, which carry Hilbert spaces \mathcal{H}_i . The blue circles denote isometries that perform the RG transformations. Taken as an ansatz state, this is equivalent to a matrix-product state.

we have enforced normalization and orthogonality of the state. The procedure is graphically represented in Fig. 1.3.

1.2.2 Choosing the RG transformation

We are left with the task of identifying appropriate isometries A_n . A possible prescription is to take A_n as the projection onto the lowest-energy states in $\mathcal{H}_1^{n-1} \otimes \mathcal{H}_{n+1}$; this requires the (numerical) diagonalization of the Hamiltonian in this Hilbert space, which should be feasible if the Hilbert space dimension of the effective sites is kept within reasonable bounds. This procedure is in fact equivalent to Wilson's renormalization group procedure, which yields excellent results in specific cases, such as the Kondo impurity problem. However, for many other lattice systems, even including a single free particle, it fails to reach sufficient accuracy.

As shown by White in 1992 [15], a much better approximation to the ground state is obtained if instead of the lowest-energy states, the states with the most important contribution to the reduced density matrix are kept. Some knowledge about the rest of the system is required to determine these states; the iterative procedure used to solve this is a key part of the Density Matrix Renormalization Group. We postpone the discussion of this procedure to a later point; now, we focus on understanding the reasons why this will lead to a good approximation.

Let us describe the RG transformation suggested by White in more detail. Following the notation of Section 1.1.2, we refer to the two leftmost sites of our (possibly renormalized) lattice as \mathcal{A} and the rest of the system as \mathcal{B} . Consider the

eigenvalue decomposition of ρ_A ,

$$\rho_A = \sum_{\alpha=1}^N \lambda_\alpha |u_\alpha\rangle\langle u_\alpha|, \quad (1.10)$$

where the λ_α are sorted such that $\lambda_\alpha \geq \lambda_{\alpha+1}$, and $N = \dim \mathcal{H}_A$. Let us take as isometry A the projection onto the M eigenvectors of the reduced density matrix with the largest eigenvalues,

$$A = \sum_{\alpha}^M |\alpha\rangle\langle u_\alpha| = \begin{pmatrix} \langle u_1| \\ \langle u_2| \\ \vdots \\ \langle u_M| \end{pmatrix} \quad (1.11)$$

where the $|\alpha\rangle$ are canonical basis vectors in a Hilbert space of dimension M , which will be smaller than the dimension of the Hilbert space of the subsystem A . Due to orthonormality of the eigenvectors of ρ_A , this is an isometry.

Consider now the expectation value of an operator O , which has support only in \mathcal{A} :

$$\langle O \rangle = \text{Tr} \rho_A O = \sum_{\alpha=1}^N \lambda_\alpha \langle u_\alpha | O | u_\alpha \rangle. \quad (1.12)$$

Performing the RG transformation $\tilde{\rho}_A = A \rho_A A^\dagger$, $\tilde{O} = A O A^\dagger$, we obtain

$$\langle \tilde{O} \rangle \approx \sum_{\alpha=1}^M \lambda_\alpha \langle u_\alpha | O | u_\alpha \rangle. \quad (1.13)$$

Note that the sum now runs only up to $M \leq N$. Assuming that $|\langle u_\alpha | O | u_\alpha \rangle| \leq \bar{O}$, this implies that

$$|\langle O \rangle - \langle \tilde{O} \rangle| \leq \bar{O} \sum_{\alpha=M+1}^N \lambda_\alpha \sim \mathcal{O} \left(\sum_{\alpha=M+1}^N \lambda_\alpha \right). \quad (1.14)$$

The error made by choosing the isometry A is therefore related to the sum of the discarded eigenvalues of ρ_A .

This establishes an important relation to the entanglement entropy: the maximally entangled state corresponds to the state where all eigenvalues of the reduced density matrices are equal – which means that the basis cannot be truncated without making a significant error. A weakly entangled state, on the other hand, is characterized by a single large eigenvalue corresponding to the mean-field solution and a quick decay of the spectrum below this state; we can therefore truncate at a relatively small value of M without sacrificing too much accuracy.

1.3 Outline

In the first part of this thesis, tensor network states are introduced in some detail. Chapter 2 explains algorithms based on matrix-product states (MPS), projected entangled-pair states (PEPS) and multi-scale entanglement renormalization (MERA); furthermore, fermionization of a tensor network and complete-graph tensor network states (CGTNS) are discussed. In Chapter 3, a general formalism for symmetric tensor networks is introduced. Finally, Chapter 4 discusses some aspects of the implementation of tensor network states with C++.

A central part of this thesis is contained in Chapter 5, where the accuracy of projected entangled-pair states is systematically assessed in comparison to established methods. For a number of non-frustrated spin systems, we compare the results of the iPEPS algorithm to Quantum Monte Carlo calculations. We then proceed to study a frustrated system which cannot be simulated with Quantum Monte Carlo methods. Finally, we confirm the validity of our approach for symmetric tensor networks by analyzing the accuracy of a symmetric version of iPEPS.

Another important part of this thesis is the discussion of a class of supersymmetric models for interacting lattice fermions in Chapter 6. We first introduce the concept of supersymmetry in non-relativistic quantum mechanics. Furthermore, we discuss in some detail conformal field theory and its relation to critical one-dimensional quantum systems, where we emphasize in particular the connections to numerical results on finite lattices and with numerical renormalization group approaches such as the MERA. Results for the model on the chain and the square ladder are discussed. In the case of the chain, we obtain an expression for the corrections to the entropy due to open boundary conditions. In the case of the square ladder, the critical theory is investigated using several different approaches.

In Chapter 7, the SU(3) Heisenberg model in two dimensions is studied using projected entangled-pair states and the density matrix renormalization group. We discuss the nature of the ground state of the model, which is found to break SU(3) symmetry and form a three-sublattice order for the case of the square and triangular lattice. We estimate the local moment using both techniques.

In Chapter 8, we put forward a measure called indistinguishability as simple way to detect phase transitions and identify ansatz wavefunctions without recourse to explicit order parameters. The approach is tested for two one-dimensional spin systems, the Ising model in transverse field and the spin-1 bilinear-biquadratic chain, as well as a model of topological order, the Toric code.

Chapter 2

Tensor network states

Tensor network states aim to generalize matrix-product states in various ways. The most important goal is to find states that are directly applicable to two-dimensional systems, in the sense that two-dimensional systems that obey an area law can be described by a number of parameters that grows at most polynomially in the system size. Other possible extensions include better descriptions for critical systems, which enables a very precise relation to fixed points of RG procedures, or the description of systems which completely lack geometrical structure, which are found for example in quantum chemistry.

In this chapter, we will discuss, in addition to a more detailed discussion of matrix-product states, examples for ansatz states that aim to meet one or more of the above goals. Much of this thesis will be devoted to projected-entangled-pair states (PEPS), which are the straightforward extension of MPSs to more general graphs or lattices. Another important class of states we discuss is the multi-scale entanglement renormalization ansatz (MERA), which can be advantageous in both one and two dimensions. We then discuss how to apply tensor network state algorithms to fermionic systems. Finally, we will discuss the complete-graph tensor network state, which is appropriate for problems lacking geometric structure.

To simplify the following discussion, we will explain some notational and foundational issues at this point. Our discussion will concern quantum systems on a lattice, where on each site a physical system with a Hilbert space \mathcal{H}_p of dimension d lives – the physical Hilbert space. We will usually use $|\sigma_i\rangle$ to denote the basis of the physical Hilbert space on site i ; for now, the degrees of freedom will be bosonic. The full Hilbert space is usually the tensor product of the physical spaces on each site; we will see examples where this is not the case in Chapter 6.

A tensor network state is a representation of the coefficients $c(\sigma_1, \sigma_2, \dots)$ of the full wave function,

$$|\psi\rangle = \sum c(\sigma_1, \sigma_2, \dots) |\sigma_1\rangle |\sigma_2\rangle \dots \quad (2.1)$$

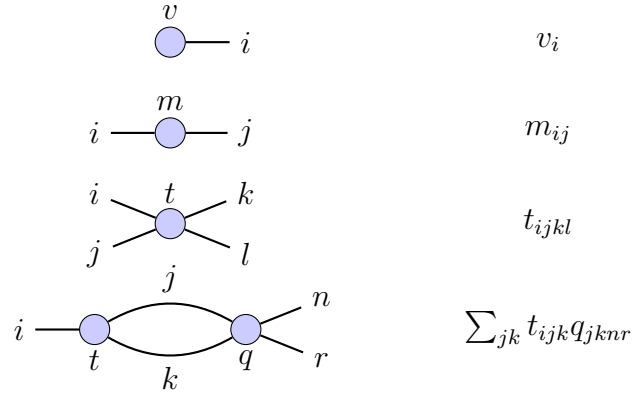


Figure 2.1: Diagrammatic representation of tensors. From top to bottom: i) vector, ii) matrix, iii) rank-4 tensor, iv) contraction of a rank-3 with a rank-4 tensor.

where the sum runs over all states in the full Hilbert space. The coefficients are expanded into a set of tensors which are connected to a network; the connections indicate indices that have to be summed to yield the scalar value. A very simple example of such a contraction is shown in Fig. 2.1. In the following, we will usually not express the network in equations, but instead in diagrams with the building blocks of Fig. 2.1, as such a notation proves to be much more readable. A more precise definition of the tensors will be given in Chapter 3 in the context of symmetries in tensor network states.

2.1 Matrix-product states

Based on the discussion in Section 1.2.1, we can immediately define the class of so-called matrix-product states. These states were first identified as the states obtained from DMRG in the thermodynamic limit in Ref. [51], but in fact look back to a long history of similar states, e.g. [52, 53]. Let us denote the components of the isometry A_1 of Fig. 1.3 acting on \mathcal{H}_1 and \mathcal{H}_2 as

$$A_1^{\alpha_2}(\sigma_1, \sigma_2) = \langle \alpha_2 | A_1 | \sigma_1 \sigma_2 \rangle, \quad (2.2)$$

where $|\alpha_2\rangle \in \mathcal{H}_1^1$, $|\sigma_1\rangle \in \mathcal{H}_1$, $|\sigma_2\rangle \in \mathcal{H}_2$. We can formally write this as

$$A_1^{\alpha_2 \alpha_1}(\sigma_2) A_0^{\alpha_1}(\sigma_1), \quad (2.3)$$

where we imply summation over the indices occurring twice, and where A_0 can be chosen as $A_0^{\alpha_1}(\sigma_1) = \delta_{\alpha_1 \sigma_1}$. Similarly, we can denote the components of all isometries as $A_n^{\alpha_n \alpha_{n-1}}(\sigma_n)$, where $|\alpha_n\rangle \in \mathcal{H}_1^{n-1}$. A coefficient of the full wave

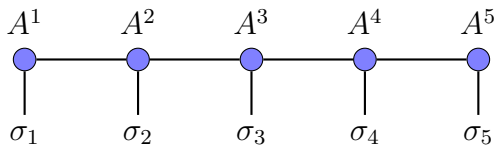


Figure 2.2: Diagrammatic representation of a matrix-product state $|\psi\rangle$ defined on a chain of length $L = 5$ with open boundary conditions, given by tensors A^1, A^2, \dots . The picture shows the diagrammatic representation of the weight of a configuration, $\langle\sigma_1\sigma_2\dots|\psi\rangle$.

function can then be expressed as

$$\langle\sigma_1\sigma_2\dots|\psi\rangle = A_n^{\alpha_{n-1}}(\sigma_n)A_{n-1}^{\alpha_{n-1}\alpha_{n-2}}(\sigma_{n-1})\dots A_0^{\alpha_1}(\sigma_1). \quad (2.4)$$

Identifying $A_k^{\alpha_k\alpha_{k-1}}(\sigma_n)$, for fixed k and σ_k , as a matrix, it becomes clear that the above expression is the product of these matrices, which justifies the name. To make the product a scalar, we require that $\dim \mathcal{H}_1^n = 1$, so that the left- and right-most matrices are in fact just vectors.

We now discuss some important properties of MPSs:

- ▷ If the A_n are chosen to be unitary, i.e. if the dimension of \mathcal{H}_1^n is chosen to equal the dimension of $\mathcal{H}_1^{n-1} \otimes \mathcal{H}_{n+1}$, the matrix-product state becomes an exact representation of the full state. Of course, this leads to a matrix dimension which grows exponentially with the system size, rendering practical calculations impossible. One therefore introduces the cutoff parameter M , commonly referred to as bond dimension, and chooses $\dim \mathcal{H}_1^n \leq M$ for all n . This cutoff parameters permits the systematic refinement of the variational ansatz.
- ▷ It is not necessary to restrict the A_n to be isometric; a general MPS can however always be brought to a form where the matrices are isometric. It is therefore not necessary to perform an optimization only over isometric matrices, which would be more difficult to perform.
- ▷ MPSs are not unique: introducing a resolution of the identity on a bond will change the values of matrices, but not the physical state. This freedom can be used to enforce different normalizations which are advantageous to the algorithm.
- ▷ Algorithms based on MPSs generally have a low-order polynomial scaling in the bond dimension, usually $\mathcal{O}(M^3)$, where M is the bond dimension defined above. The details will be discussed below.

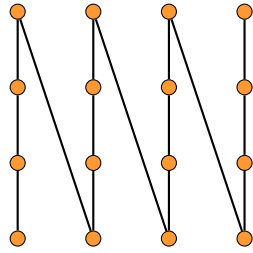


Figure 2.3: "TV screen" mapping for a 4×4 system to a one-dimensional system. This allows the simulation using a one-dimensional ansatz, but introduces long-range operators.

- ▷ As we discuss in more detail in the next section, the amount of entanglement that a matrix-product state of a given bond dimension M can contain is bounded by

$$S \leq \log M. \quad (2.5)$$

This makes it plausible that a gapped state, which has bounded entanglement for any system size, can be described accurately by an MPS of fixed bond dimension. For a critical system, we find using Eqn. (1.5) that the bond dimension should grow like

$$M \geq L^{c/6}. \quad (2.6)$$

This indicates that while we cannot approach the thermodynamic limit with a fixed bond dimension, the growth is usually sufficiently weak that system sizes much larger than exact diagonalization can be accessed.

- ▷ To simulate a higher-dimensional system with DMRG, it must be mapped to a chain. An example of such a mapping is shown in Fig. 2.3. The problem with such a mapping is twofold: firstly, it creates long-range interactions. These can be dealt with in such a way that the algorithm becomes only slightly more costly. A more severe problem is that there inevitably exists a way to cut through the system such that the two parts are only connected by a single bond of the MPS, but such that the boundary – and correspondingly the entropy that has to be described by this bond – scales at least linearly with the system width. To accommodate this at fixed precision, the bond dimension has to grow exponentially with the width (but not the length) of the system. This was first observed in Ref. [54].

Nevertheless, MPS can be used to describe higher-dimensional systems, as the system size that can be reached is still larger than in exact diagonalization. For a short review of applications of DMRG in two dimensions, see

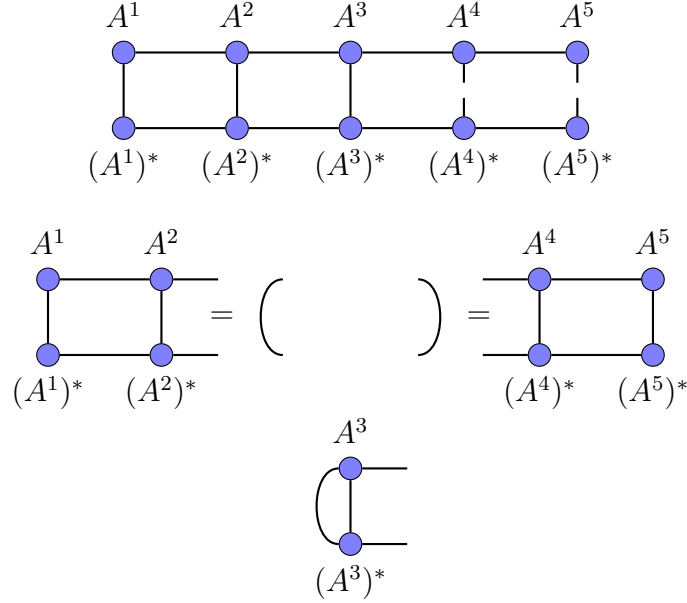


Figure 2.4: Top panel: Coefficients of the reduced density matrix as defined in Eqn. (2.9), where \mathcal{A} includes sites 4 and 5 and \mathcal{B} contains sites 1 through 3. Middle panel: Normalization constraints that make the calculation of the density matrices feasible. Bottom panel: With this normalization, the reduced density matrix for A can be written as a matrix of size $M \times M$, which can be obtained in a simple way from A^3 .

Ref. [55]. An application of DMRG to a challenging two-dimensional system is shown in Chapter 7.

Relation to density matrices

An important property of MPSs is that reduced density matrices for a block \mathcal{A} of spins can be expressed as matrices of dimension $M^n \times M^n$, where n is the number of interfaces that region \mathcal{A} has with the rest of the system. In particular, the reduced density matrix for a block of sites at the boundary of the system has size $M \times M$, and for any other contiguous block of sites has size $M^2 \times M^2$.

To obtain this result, consider a quantum system given in a state $|\psi\rangle = \sum_{\sigma} c(\sigma)|\sigma\rangle$. Splitting the system into parts \mathcal{A} and \mathcal{B} , with basis $|u\rangle, |v\rangle$, respectively, we can rewrite the state as $|\psi\rangle = \sum_{u,v} c(u,v)|u\rangle|v\rangle$. The reduced density

matrix for part \mathcal{A} is given by

$$\rho_{\mathcal{A}} = \text{Tr}_{\mathcal{B}} \rho \quad (2.7)$$

$$= \sum_{\tilde{v}} \langle \tilde{v} | \left(\sum_{\substack{u, u' \\ v, v'}} c(u, v) c(u', v')^* |u\rangle |v\rangle \langle u'| \langle v'| \right) | \tilde{v} \rangle \quad (2.8)$$

$$= \sum_{u, u'} \left(\sum_v c(u, v) c(u', v)^* \right) |u\rangle \langle u'|. \quad (2.9)$$

The coefficients $\sum_v c(u, v) c(u', v)$ are easily expressed as tensor network state as shown in Fig. 2.4 for the example of a chain of length 5, with \mathcal{B} being the leftmost 3 sites. With this choice, the rank of the reduced density matrix is bounded by M , but the naive evaluation of the tensor network would nevertheless yield an exponentially large object. If, however, the normalization is enforced such that all tensors except those at site 3 are isometric in the way that is shown in the second panel of Fig. 2.4, the contraction simplifies greatly: the two leftmost pairs of tensors are contracted to yield the identity, and the two rightmost tensors are only isometric basis transformations which do not affect the spectrum of the density matrix. The density matrix can therefore be obtained simply by evaluating the tensor network shown in the third panel of Fig. 2.4.

Expectation values and matrix-product operators

As mentioned before, the contraction of an MPS can be performed in polynomial time. The most simple contraction is the evaluation of the norm $\langle \psi | \psi \rangle$; the tensor network to represent this is shown in the upper panel of Fig. 2.5. The evaluation can be performed in $\mathcal{O}(M^3 d)$, where M is the bond dimension and d the dimension of the local physical Hilbert spaces.

To evaluate the expectation value of some operator O , $\langle \psi | O | \psi \rangle$, it is useful to work with matrix-product operators (MPOs). These are reminiscent of MPS, but instead of having one physical index, they have two separate physical indices. They can be used to encode arbitrary operators into a simple tensor network. Analogous to matrix-product states, the tensors, which we will refer to as W^n , are connected by bonds, whose dimension we will denote as D . The bond dimension necessary to exactly encode a physical operator depends on the type of operator:

- ▷ A simple product of single-site operators can be represented with $D = 1$. Such an MPO can be used to measure local observables.
- ▷ To calculate the sum of a list of strictly local operators, it is not necessary to calculate the expectation value for all operators separately. Instead, a

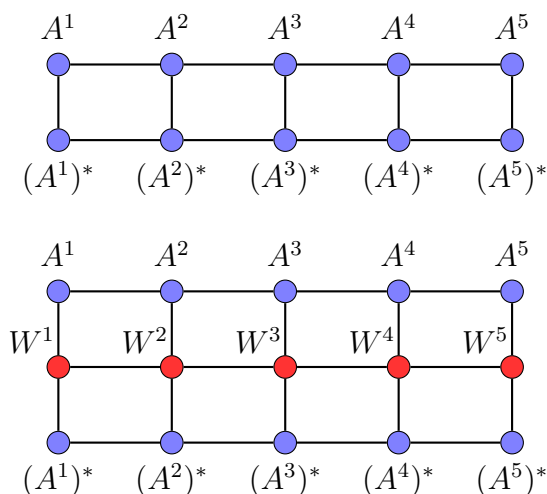


Figure 2.5: Diagrammatic representation for the expectation values calculated from an MPS, as shown in Fig. 2.2. Top panel: Expectation value of the norm, $\langle \psi | \psi \rangle$. The stars indicate complex conjugation. Bottom panel: Expectation value of an operator O , $\langle \psi | O | \psi \rangle$, where O is given as a matrix-product operator made from tensors W^i . The computational cost of contracting these networks is usually dominated by the bond dimension and scales as $\mathcal{O}(M^3)$. Stars indicate complex conjugation.

single MPO can be constructed, which will usually have bond dimension $D = 2$. Evaluating it will be computationally more efficient than evaluating all single-site operators separately.

- ▷ Local Hamiltonians for systems on a chain can usually be represented with a bond dimension in the range from 5 to 10. In the case of higher-dimensional systems, the bond dimension will grow with the system size. This is also the case for systems with long-range interactions.

The tensor network necessary to evaluate the expectation value $\langle \psi | O | \psi \rangle$ of a matrix-product state with a matrix-product operator is shown in the lower panel of Fig. 2.5. The most expensive steps of the contraction scale as $\mathcal{O}(M^3 d D)$ and $\mathcal{O}(M^2 d^2 D^2)$.

2.1.1 Variational optimization of matrix-product states

Two approaches are commonly used to find the best approximation to the ground state of a physical system within the space of matrix-product states: a direct variational optimization and imaginary time evolution. The first approach is more commonly used, in particular for finite systems; for infinite systems, on the other

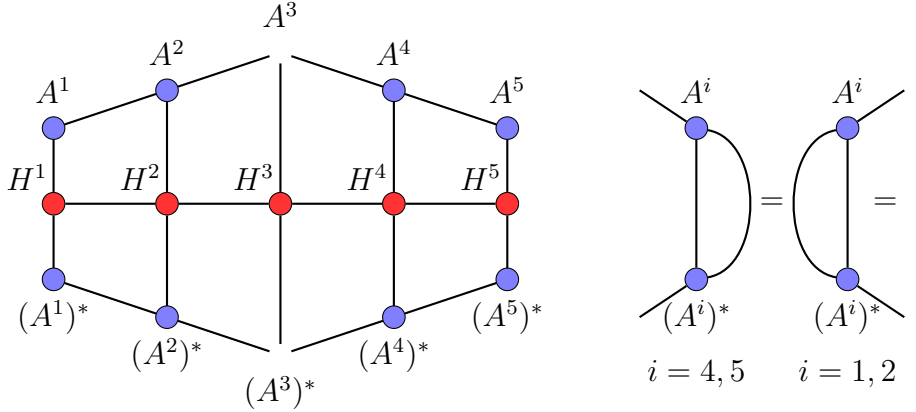


Figure 2.6: Effective single-site Hamiltonian for site 3. The two leftmost matrices are isometric such that contracting their physical and left indices with the complex conjugate yields the identity; for the two rightmost matrices, the normalization is chosen such the identity is obtained when contracting the physical and right indices.

hand, imaginary time evolution has become more and more popular. In this thesis, we will describe an example of both methods: i) The variational optimization of a finite MPS as described by White [15] in the first DMRG paper. ii) The time evolution scheme proposed by Vidal in Refs. [56, 57] for finite and infinite systems. The second approach will play an important role as building block of the PEPS algorithm.

In this description of the variational optimization, we will follow the description of Ref. [58]. The most important difference to the original description of White is that we proceed with a single-site optimization instead of performing the optimization for two sites simultaneously. We follow this approach since it appears more natural in the language of matrix-product states; from an RG perspective, the other approach may seem more natural.

The optimization proceeds in the following steps:

1. Construct an **initial state**. This state can be either random or constructed using some knowledge about the physics of the ground state. In the latter case, one has to make sure that it does not bias the simulation strongly towards a particular solution. In the first case, one should ensure that the final result does not show a strong dependence on the initial state (random seed).
2. Enforce **normalization**. For the purpose of this optimization, it is advisable to work in the normalization shown in Fig. 2.6. In this example, we consider

the optimization of the tensor associated with the center site, A^3 . In this case, we would ensure that A^1 and A^2 are isometric when multiplied on the left, while A^4 and A^5 are isometric when multiplied on the right. This is depicted in the right panel of Fig. 2.6; we here depict the MPS as a tree to indicate such a choice of normalization. To achieve this normalization, a singular-value decomposition can usually be used.

3. The optimization of a single tensor can be mapped to solving for the lowest eigenvalue of the effective Hamiltonian operator, which is given by the tensor network shown in the left panel of Fig. 2.6. In general, one has to ensure correct normalization of the state, which may require to solve a generalized eigenvalue problem. It is advantageous to fix the normalization shown in the right panel of Fig. 2.6, such that the norm of the full state equals the standard 2-norm of the elements of the tensor that is being optimized and the generalized eigenvalue problem turns into a standard eigenvalue problem. As only the lowest eigenpair is needed, the eigenvalue problem should be solved with some iterative diagonalization method such as Lanczos or Jacobi-Davidson [59, 60]. Since these only require a matrix-vector product and not the full matrix, the optimization will scale as $\mathcal{O}(M^3)$. If one were to set up the full matrix and solve it with an iterative method, the scaling would become $\mathcal{O}(M^4)$; solving it with a dense method would lead to $\mathcal{O}(M^6)$.
4. After solving the local eigenvalue problem, one moves to the next site. The tensor resulting from the previous step should be **normalized** properly, which is usually achieved by a singular-value or QR decomposition. The optimization should be swept back and forth until convergence of the energy is reached.

To improve convergence of the method, the enhancement described in Ref. [61]. We will use this optimization method to obtain the results discussed in Chapter 6.

2.1.2 Time evolution

A simple procedure for performing time evolution with a matrix-product state was proposed by Vidal in Ref. [62] and later extended to infinite systems in Ref. [57]. At the same time, several other approaches to simulate time evolution with MPS were put forward [63, 64, 65]. The approach of Vidal was discussed in more detail and extended to more general classes of operators in Ref. [66].

All these methods are based on the decomposition of the full time evolution operator into a product of operators that perform the evolution over a very small time step $\Delta t = t/N$ and are therefore close to the identity. For a Hamiltonian that

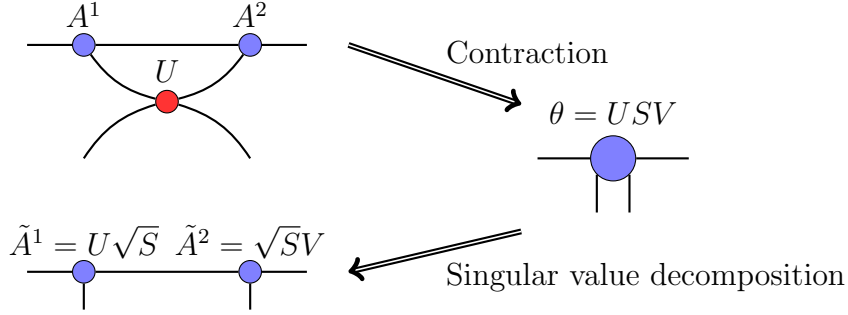


Figure 2.7: Evolution for a finite MPS which is not given in the canonical form. For the procedure to be exact, it is necessary that the other tensors are normalized as shown in Fig. 2.6, but with two sites at the center. The two adjacent tensors are multiplied together with the evolution operator, then a singular value decomposition is performed to obtain the new tensors. The square root of S can trivially be obtained as it is diagonal and positive.

is a sum of time-independent local terms, $H = \sum_{\langle i,j \rangle} h_{ij}$, where the sum runs over pairs of nearest neighbors on the lattice, a very simple decomposition is given by

$$U = \exp(-iHt) \quad (2.10)$$

$$= \prod_{k=1}^N \exp\left(-i \sum_{\langle i,j \rangle} h_{ij} \Delta t\right) \quad (2.11)$$

$$= \prod_{k=1}^N \prod_{\langle i,j \rangle} \exp(-ih_{ij} \Delta t) + \mathcal{O}(\Delta t) \quad (2.12)$$

$$= \prod_{k=1}^N \prod_{\langle i,j \rangle} U_{ij}. \quad (2.13)$$

Higher-order formulas can be used to reduce the discretization error. In the case of imaginary time evolution, discretization errors do not accumulate and can easily be eliminated by decreasing the time step Δt during the simulation.

The key part of a time evolution method is to efficiently perform the optimization problem

$$\min_{|\psi'\rangle} \| |\psi'\rangle - U_{ij} |\psi\rangle \|, \quad (2.14)$$

where the desired state $|\psi'\rangle$ is again a matrix product state, usually of the same or just slightly larger bond dimension as $|\psi\rangle$. The procedure proposed in Ref. [62], referred to as time-evolving block decimation (TEBD), is shown in Figure 2.7.

The method is only accurate if the normalization is chosen similar to the one of Fig. 2.6, i.e. such that the tensors to the left and the right of those being optimized are chosen isometric. In some cases, in particular for imaginary time evolution, it may not be necessary to enforce such a normalization explicitly, as the SVD will yield tensors sufficiently close to an isometry (indeed, performing TEBD without truncation would yield correctly normalized states).

Another update procedure, which works also for more general (long-range) operators and if the normalization cannot be enforced, was proposed by Verstraete et al in [63]. Let

$$\epsilon = \| |\psi'\rangle - U_{ij}|\psi\rangle \|^2 \quad (2.15)$$

$$= \langle \psi' | \psi' \rangle + \langle \psi | U_{ij}^\dagger U_{ij} | \psi \rangle - 2 \operatorname{Re} \langle \psi' | U_{ij} | \psi \rangle. \quad (2.16)$$

Note that $U_{ij}^\dagger U_{ij} = \mathbf{1}$ if the evolution is unitary. The terms in this sum can all be calculated from simple tensor networks analogous to those shown in Fig. 2.5. To solve for a minimum, we should solve for a root of the gradient $\nabla\epsilon$ with respect to the entries of the matrices, where normalization should be enforced. Since solving this for the entire state simultaneously is not feasible, the algorithm proceeds site by site, sweeping back and forth until convergence is reached. The algorithm therefore also proceeds locally and can be performed at roughly the same cost as TEBD, if partial contractions of tensor networks from earlier steps are re-used in each step of the simulation.

Let us denote the elements of a single tensor as \vec{x} , which we assume to be real. We will make use of the tensor network for the effective Hamiltonian shown in Fig. 2.6, but replace the MPO by local evolution gates. If we refer to this network as $M(O)$, where O is a local (or two-site operator), and define $N_{\text{eff}} = M(\mathbf{1})$, $U_{\text{eff}} = M(U)$, and $U_{\text{eff}}^2 = M(U^\dagger U)$, we can express ϵ as

$$\epsilon = (x')^T N_{\text{eff}} x' + x^T U_{\text{eff}}^2 x - (x')^T U x - x^T U^T (x'). \quad (2.17)$$

Deriving this, we find that we have to solve

$$x' = (N_{\text{eff}})^{-1} U x. \quad (2.18)$$

By choosing the normalization of Fig. 2.6, N_{eff} can be made equal to the identity, in which case solving the above problem becomes trivial. If normalization is not fixed, several numerical approaches exist that efficiently solve this linear problem. The computational cost for the inverse scales as $\mathcal{O}(M^6)$ if performed via a naive dense solver. This can be reduced to $\mathcal{O}(M^4)$ by using some iterative method such as conjugate gradient, and can be further reduced to $\mathcal{O}(M^3)$ if the matrices are not constructed explicitly, but instead only the matrix-vector product required by the conjugate gradient solver is used. It should be noted that in this approach, an operator combining several terms can be applied at once.

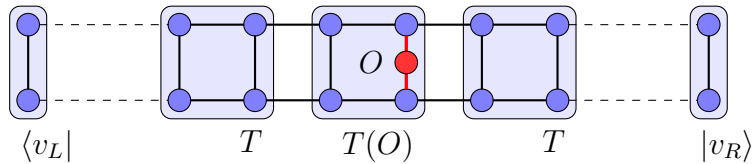


Figure 2.8: Illustration of the transfer operators that form the building blocks of an infinite MPS algorithm. We here assume an $ABAB$ structure, i.e. two independent tensors; the transfer operator T is then formed by contracting those two tensors with their complex conjugate. Single-site and two-site operators can be included to form the transfer operator $T(O)$.

2.1.3 Infinite matrix-product states

Although the original description of DMRG by White contained an algorithm for infinite systems, calculations are commonly carried out for finite systems. This is mainly because the original infinite size algorithm does not converge very well; it is however widely used to obtain initial states for the finite-size algorithm. Another restriction is that a truly infinite system can only be studied if translational invariance is assumed (this is however not the approach of the original infinite size DMRG). Recently, infinite MPS algorithms have become more popular; this is partly due to an efficient and accurate algorithm for (imaginary) time evolution of infinite states due to Vidal [57], and partly because such states form an important building block of algorithms for higher-dimensional tensor networks.

Let us discuss in more detail how to operate on infinite, translationally invariant MPSs. In the simplest case, all tensors would be chosen to be the same; in most situations, however, it is advantageous to choose a larger unit cell, for example two inequivalent tensors, leading to an $\dots ABABAB \dots$ structure. Two of these tensors (and their complex conjugates) can then be contracted together to obtain a transfer operator T ; if one wants to evaluate a local operator O , this can be achieved by placing an operator in this small tensor network to yield $T(O)$ (T is only a special case of this, $T = T(\mathbf{1})$). Both of these are shown in Figure 2.8.

To extract an expectation value, one now finds the dominant (i.e., with largest eigenvalue) left and right eigenvectors of the transfer operator T , which we will denote as $\langle v_L|$ and $|v_R\rangle$. An expectation value can then be calculated as

$$\langle O \rangle = \frac{\langle v_L | T(O) | v_R \rangle}{\langle v_L | T | v_R \rangle}. \quad (2.19)$$

Similarly, a two-point correlation function with distance n is calculated by

$$\langle O_i P_{i+n} \rangle = \frac{\langle v_L | T(O) T^n T(P) | v_R \rangle}{\langle v_L | T^{n+2} | v_R \rangle}. \quad (2.20)$$

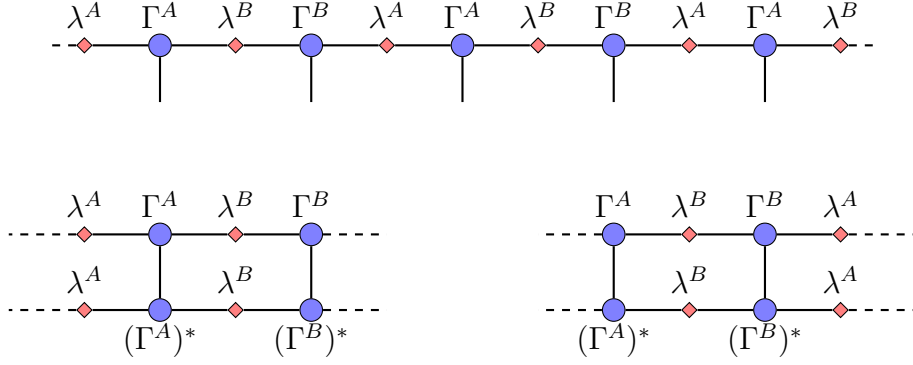


Figure 2.9: Top panel: Canonical form for an infinite matrix-product state. Lower panel: Transfer operators that can be used for a consistent normalization. When inserting these into Eqns. (2.19) and (2.20), care has to be taken to have connect them with an additional λ^A .

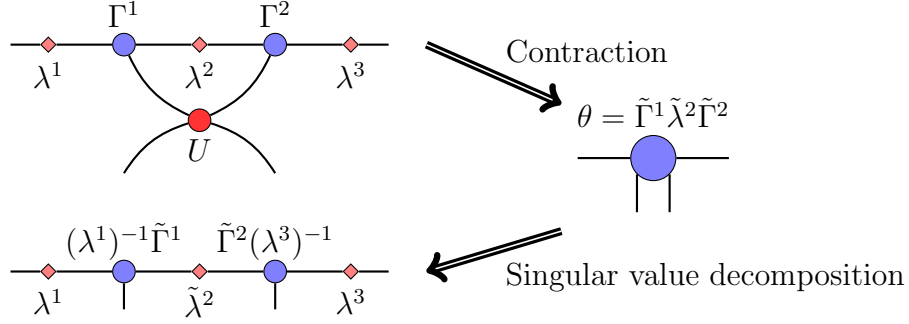


Figure 2.10: Time evolution for an MPS in canonical form. The evolution is equivalent to that shown in Fig. 2.7 for a finite system up to a choice of normalization.

To ensure numerical stability for large n , it is advisable to rescale A and B such that the largest eigenvalue of T is 1.

It turns out to be useful to define a canonical form for infinite matrix product state as shown in Fig. 2.9. On the bonds of the MPS, we introduce diagonal matrices λ^i , which will be chosen to have only non-negative values. A useful normalization is obtained by choosing a gauge where the left eigenvector (right eigenvector) of the transfer operator shown in the lower left (right) panel of Fig. 2.9 is the identity. Details on how to enforce this gauge will not be explained here, but can be found in [66].

In this gauge, the update procedure shown in Fig. 2.10 becomes exact also for

infinite systems. It is extremely similar to the one shown for finite systems in Fig. 2.7, with the difference being the treatment of the weight matrices λ . This is necessary to obtain a consistent gauge condition also in the thermodynamic limit, as the normalization shown in Fig. 2.6 cannot be chosen for an infinite MPS because tensors cannot simultaneously be left- and right-normalized. When taking the inverse of the matrices λ , a pseudo-inverse should usually be taken. In this case of diagonal matrices, this is obtained by replacing $1/\lambda_i \rightarrow 0$ for $\lambda_i < \epsilon$, where ϵ is some suitably chosen cutoff, usually close to the machine epsilon.

2.2 Projected entangled-pair states

Projected entangled-pair states have been suggested in different variations by several authors. The first proposal was by G. Sierra and M. A. Martin-Delgado under the name of vertex matrix product ansatz [67], which was subsequently applied to evaluate the partition function of a 3D classical model by Nishino and Okunishi [68, 69]. A first application to infinite, homogeneous quantum systems is found in Ref. [70]. A formalism for inhomogeneous, finite systems was proposed by Verstraete and Cirac [16], where the name of *projected entangled-pair states* was first used. In Ref. [71], infinite systems were reconsidered from the point of view of extending Verstraete and Cirac’s formalism.

Many variations of the method have been proposed [72, 73, 74, 75, 76, 77, 78, 79, 80, 81]. Applications have been focused on non-frustrated [82, 83, 84] and frustrated [85, 86, 87, 88, 89] spin systems; an application to real time evolution of a two-dimensional system is found in [90]. Later in this chapter, we will discuss extensions to fermionic systems.

In principle, a PEPS can be constructed on arbitrary graphs; in this thesis, we will discuss the case of the square lattice. Furthermore, we restrict the discussion to systems where the degrees of freedom on all sites are the same, so that with each site a Hilbert space $\mathcal{H}_{\text{phys}}$ of dimension d is associated, and where the full Hilbert space is the tensor product of the local Hilbert spaces. We will denote the basis on site i as $|\phi_i\rangle$ and the basis for the full system as $\{|\phi\rangle = |\phi_1\rangle|\phi_2\rangle \dots\}$. Similar to matrix-product states, our goal is to approximate the coefficients $c(\phi)$ of a wave function $|\Psi\rangle = \sum c(\phi)|\phi\rangle$

PEPS can be understood as direct extension of MPSs to arbitrary graphs: while the tensors of an MPS have three legs – one enumerating the state in the local physical Hilbert space, and two connecting to the neighbors – a PEPS is made up of tensors of rank $z + 1$, where z is the number of nearest neighbors. Again, one of these indices is the physical index, while the others connect to tensors on the adjacent sites. The coefficient $c(\phi)$ is then given as the trace over all auxiliary

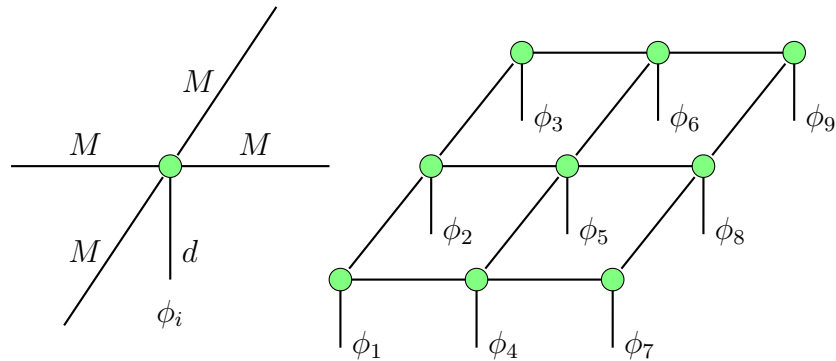


Figure 2.11: Pictorial representation of a projected entangled-pair state (PEPS). Left panel: For the square lattice, a tensor of rank 5 will be associated with each site in the bulk of the system. The index pointing down connects to the physical system, while the other indices connect to neighboring tensors in the state. Right panel: The panel shows the PEPS decomposition of a coefficient $c(\phi)$ for a state $|\Psi\rangle = \sum c(\phi_1 \dots \phi_9) |\phi_1 \dots \phi_9\rangle$ on a 3×3 square lattice with open boundary conditions.

indices in the network. A graphical representation is shown in Figure 2.11. The dimension of the bonds connecting to the nearest neighbors will again be referred to as bond dimension and denoted as M . Its role is analogous to the matrix size in an MPS:

- ▷ For $M = 1$, they are equivalent to static mean-field theory.
- ▷ For sufficiently large bond dimension, they cover the full Hilbert space of the problem.

The most important difference to matrix-product states is that they can capture the entanglement properties of systems obeying an area law at fixed bond dimension. To see this, consider the reduced density matrix for a block of sites in a PEPS as shown in Fig. 2.12. The number of bonds connecting to the rest of the system grows linearly with the size of the boundary, which means that the upper bound on the rank of the reduced density matrix grows exponentially. Therefore, in principle the entanglement entropy can grow linearly with the size of the boundary, hence satisfying an area law with a fixed bond dimension.

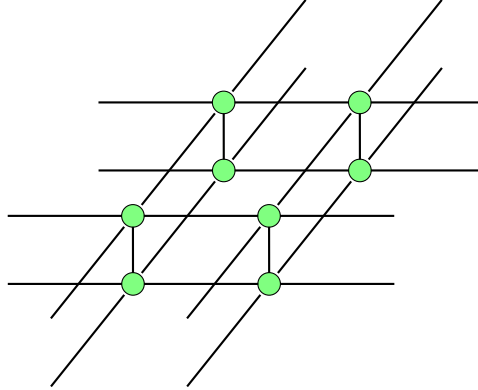


Figure 2.12: Approximate reduced density matrix of a block of 4 sites described by a PEPS. In contrast to the situation in MPS, cf. Fig. 2.4, there is no normalization that could be imposed on the rest of the state to make this the exact reduced density matrix. Nevertheless, an upper bound on the rank of the reduced density matrix can be derived from this picture.

2.2.1 Contraction of PEPS

Unlike matrix-product states, however, the exact evaluation of expectation values can not be performed in polynomial time [91]. Therefore, approximate methods are required. Several such methods have been proposed:

- ▷ In the original proposal of Ref. [16], finite systems with open boundary conditions were treated. The method is based on the insight that the coordination is less at the boundary of the system: if the physical indices are traced over to form an expectation value, the tensors at the boundary form matrix-product states (see lower right panel of Fig. 2.13, and Fig. 2.14). The other columns or rows can be regarded as matrix-product operators after tracing over physical indices. This can be exploited by adapting a time evolution method for MPS. Performing one step of such an evolution maps a system of size $N \times N$ to a system of size $(N - 1) \times N$. Iterating this, the $N \times N$ system can be reduced to a quasi-one-dimensional system of size $2 \times N$. This system can then be treated with standard methods. Assuming that the bond dimension of the boundary MPS is taken to be at most the square of the bond dimension of the PEPS, the key parts of this algorithm scale as $\mathcal{O}(M^{12})$.
- ▷ The generalization of this approach to infinite systems is conceptually simple. Given a system with an infinite number of equivalent rows (or columns), we can iterate the evolution procedure of applying a row or column as MPO to some boundary MPS many times, which will converge to some steady state if

the operator given by such a row or column has a gap in the spectrum below the largest eigenvalue. Such an eigenvector can be interpreted as representing the infinite lattice. In general, the number of iterations necessary to reach converge should be related to the correlation length of the system. This approach was first pursued by Jordan et al. in Ref. [71].

- ▷ A different approach to contracting PEPS, in particular (but not exclusively) in the infinite case, is the corner-transfer matrix (CTM) method. This approach was first described by Baxter as a method to trace over the partition sum of a classical system [52]. It was introduced into the field of tensor network states by applications to two-dimensional and three-dimensional classical systems in Refs. [92, 68]. A variant of the CTM method, the directional CTM, was used to perform the contraction of an infinite PEPS in Ref. [79]. The original approach was revisited and slightly generalized in [93]. The scaling of this approach is the same as the MPS-based method.
- ▷ A very different approach is taken in the tensor renormalization group method [76]. Instead of contracting the state by obtaining a boundary that represents the full system, this scheme is based on a coarse-graining procedure which approximately maps the original tensor network state to a new state given on a lattice with fewer sites, which is expected to capture the properties of the original state well. The procedure is iterated until a sufficiently small system which can be summed exactly is reached.

2.2.2 Optimization of PEPS

For the optimization of a PEPS, there are in principle two possibilities: direct energy minimization and imaginary time evolution. With a few exceptions such as [94], imaginary time evolution is used for most PEPS simulations. The reason why imaginary time evolution is usually preferred lies in its numerical stability: the change to the state is in general of the order of the time step and thus very small. If the optimization is performed one tensor after another, this helps to avoid instabilities in the optimization between different tensors and may also avoid local minima, as all tensors are slowly converged to their optimal values.

We therefore now describe two time evolution schemes for the PEPS, termed *full* and *simplified* update. The full update was described in Refs. [16, 71]; the simplified update was first shown by Jiang et al [76] and later described, e.g., in [6]. Furthermore, we will propose a new update scheme which can be applied to optimize PEPS for more general operators, such as next-nearest neighbor or plaquette interactions. For a discussion of the application of the simplified update

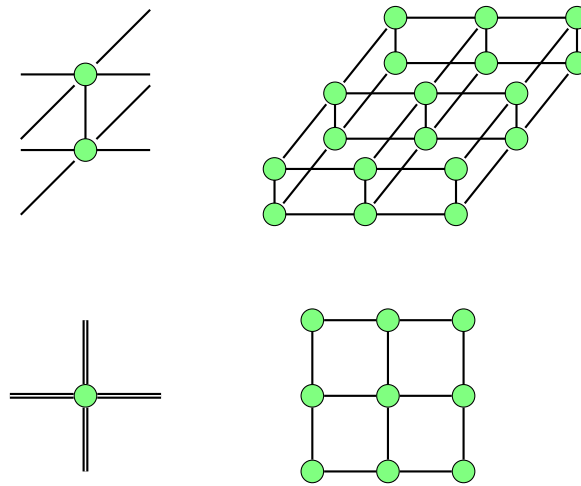


Figure 2.13: To obtain an expectation value, the state has to be contracted with itself (top right panel). For many purposes, it will be useful to draw the product of a PEPS tensor with itself, contracted over the physical index (top left panel), as a single tensor (bottom left panel). This gives a simpler picture which does not explicitly show physical bonds (bottom right panel).

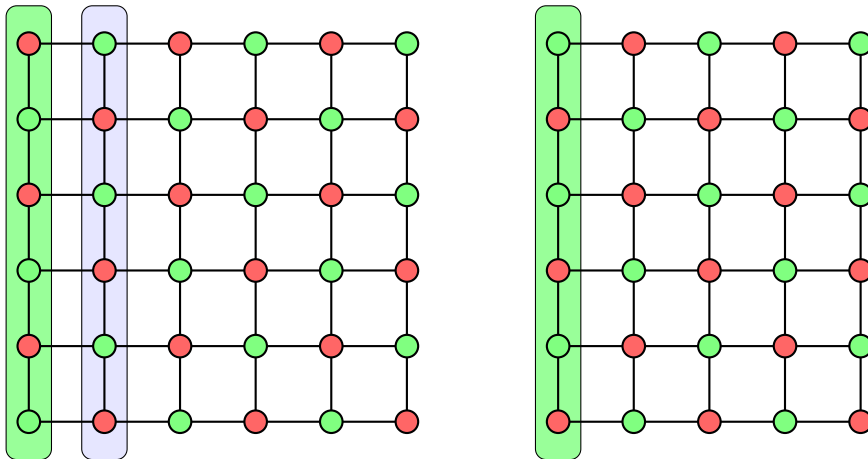


Figure 2.14: First step in the reduction of a finite PEPS of size 6×6 . After summing over the physical indices, the leftmost column (green rectangle) is a matrix-product state, the second column from the left is a matrix-product operator. Applying this MPO with one of the standard techniques available for MPO-based time evolution yields a new system of size 5×6 with an updated left column (right panel).

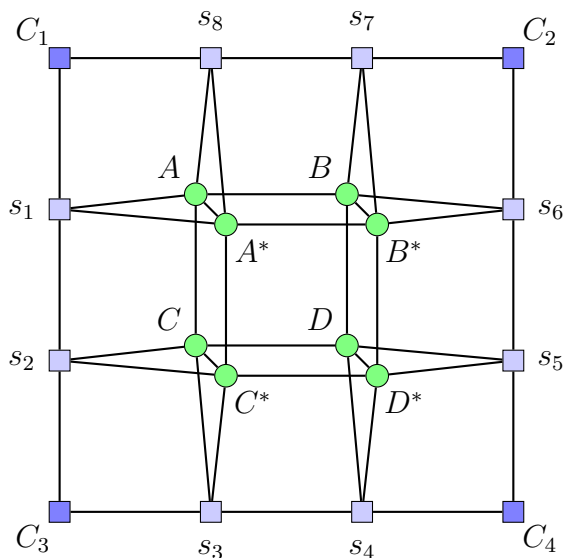


Figure 2.15: PEPS environment obtained from the corner transfer matrix method.

to next-nearest neighbor interactions, see [93].

Full update

The full update is analogous to the second update described in Section 2.1.2 for matrix-product states, i.e. we have to solve a minimization problem of the form

$$\epsilon = (x')^T N_{\text{eff}} x' + x^T U_{\text{eff}}^2 x - (x')^T U x - x^T U^T (x'), \quad (2.21)$$

where we use the notation introduced in Eqn. (2.17). This minimization must be performed for the tensors on all sites involved in the time evolution operator; for simplicity, we will focus on the case of bond operators, such that only two tensors A and B are involved. Together, these form the vector x above. The effective operators have to be calculated from a local PEPS environment, cf. Fig. 2.15, which must be obtained from one of the contraction methods described in the previous section; note also that if we perform imaginary time evolution, U is not unitary.

If x is taken to contain the elements of both A and B , the effective operators above have dimension $M^8 \times M^8$, which makes the numerical solution of (2.21) intractable. Therefore, the problem is solved for A and B separately, and the optimization is iterated until convergence is reached for both tensors.

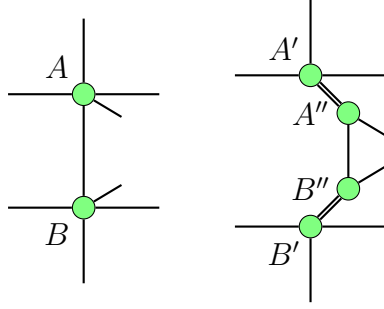


Figure 2.16: For better convergence of both the full and simplified update schemes, the PEPS tensors A , B can be split into the tensors A' , A'' and B' , B'' , respectively, by a singular-value decomposition. The optimization can then be performed only on A'' and B'' , which have fewer parameters.

As opposed to the case of MPS, we have no way of enforcing an appropriate normalization such that N_{eff} becomes the identity; to complicate matters more, it is quite often close to singular. It is therefore advisable to solve the inverse via a Moore-Penrose pseudo inverse. For a matrix M with singular value decomposition $M = USV$, this is given by $M^{-1} \approx V^\dagger S^{-1} U^\dagger$, where S^{-1} is obtained by taking the inverse of all elements which are larger than some appropriately chosen cutoff ϵ , and taking 0 otherwise. The cost of calculating this inverse scales as $\mathcal{O}(M^{12})$; however, since previous steps of the algorithm have the same scaling but with a larger prefactor, this is not a limitation in practice. In the case of infinite PEPS, the update sweeps over all tensors in the unit cell until convergence is reached.

Both the convergence and the computational cost can be improved by performing a decomposition shown in Fig. 2.16. The PEPS tensors A , B involved in the update are split as shown in the figure and the optimization is performed on the new tensors A'' , B'' , which have as legs only the physical leg, the leg connecting to the other tensor that is being updated, and an external leg connecting to A' , B' , respectively. After the update, A' and A'' , as well as B' and B'' , are contracted again to go back to the original form of the PEPS. This reduces the scaling of the pseudo-inverse to $\mathcal{O}(M^3 d^3)$.

Simplified update

The simplified update is very similar to the update of the TEBD scheme for infinite matrix-product states. The aim is to reduce the computational cost by performing an update that does not fully take into account the environment tensors, whose contraction is very time-consuming, but instead make further approximations to obtain an effective environment.

In the case of matrix-product states, this can be achieved without approximation by enforcing the canonical form described above. In the case of PEPS, this is not possible, as there is no known normalization on parts of the PEPS such that their contraction would yield the identity and could therefore be ignored for the purpose of a local optimization. It is therefore not possible to define a local update scheme comparable to TEBD that does not explicitly handle the environment. However, it turns out that the simplified update scheme works well in practice.

In analogy to the canonical form for MPS, we introduce weights on the bonds between each tensor, which we will denote as λ and which should be chosen positive. In this case, no formal justification for the weights can be given; however, numerical calculations show that the algorithm is much more robust if formulated to include the weights. The update scheme is shown in Fig. 2.17: the two tensors, the operator and the weights on the adjacent bonds are contracted together to obtain the tensor $\tilde{\Gamma}$. By first performing a singular-value decomposition and then applying the inverses of the adjacent weights, the state is brought back to the old form.

Gradient update

The full update described above is based on linearizing Eqn. (2.21) and solving the optimization problem for each tensor separately. While this usually works well for bond operators, the procedure may become very unstable in the case of e.g. plaquette operators involving four tensors. We propose another update scheme where the optimization is solved directly for all tensors using a gradient minimization algorithm such as conjugate gradient.

The key insight is that while inverting the effective operator for several tensors at once is prohibitively expensive, the gradient has only as many elements as there are variational degrees of freedom, namely nM^4d , where n is the number of tensors involved in the update ($n = 2$ for a bond operator, $n = 4$ for a plaquette operator). The gradient can be efficiently calculated by obtaining the gradient separately for each tensor keeping the other tensors fixed, and concatenating this into a single vector. This implies that the gradient does not correspond to a simple bilinear form, as a naive inspection of Eqn. (2.21) would suggest; instead, it depends in a nonlinear way on the elements of all other tensors. While this will slow down the convergence of optimization methods such as conjugate gradient, it does not pose a fundamental limitation.

The gradient update scheme is numerically slightly more expensive than the full update, despite having the same leading cost. It is therefore useful in particular in situations where the full update does not converge properly, such as models with

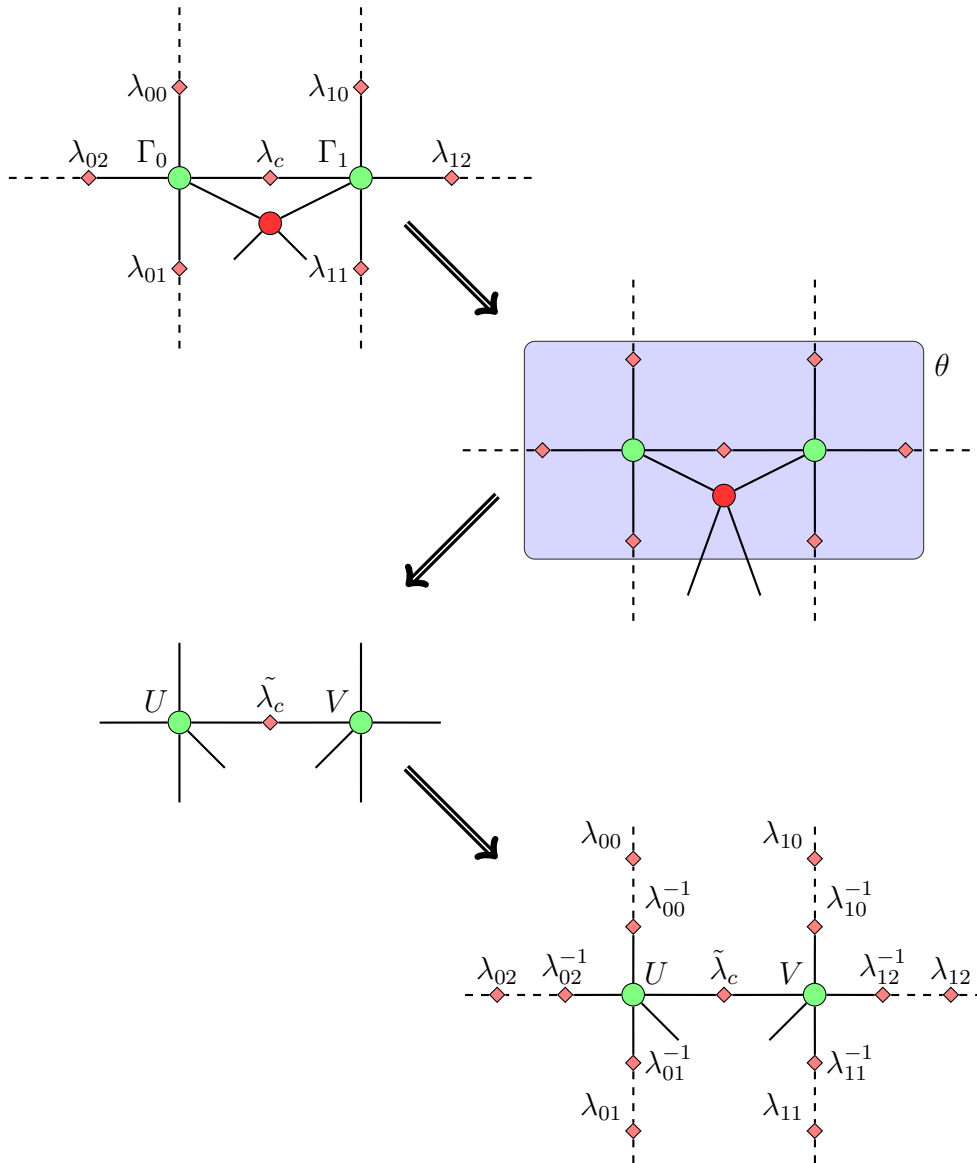


Figure 2.17: Simplified update: in the first step, the PEPS tensors, bond weights and the operator acting on the physical sites are contracted to yield θ . In the second step, this is split by means of a singular-value decomposition which yields tensors U , V , and the new bond weight $\tilde{\lambda}_c$. In the last step, the state is brought back to the old form by contracting U , V with the inverses of their adjacent bond weights to yield new $\tilde{\Gamma}_0$, $\tilde{\Gamma}_1$.

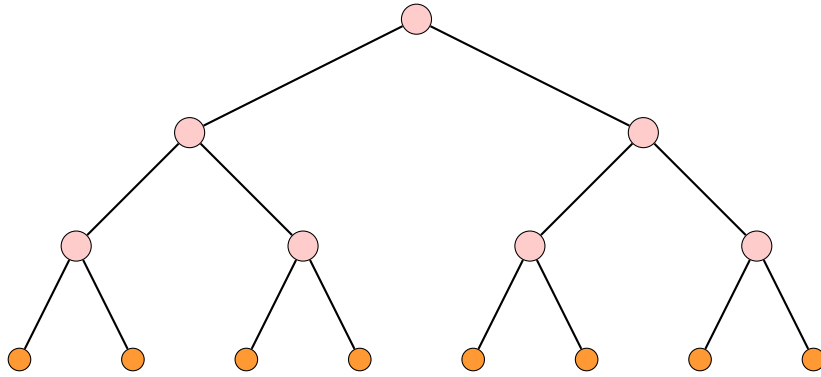


Figure 2.18: Tree tensor network representing a coarse-graining procedure that renormalizes two sites into one effective site.

operators involving more than two sites.

2.3 Multi-scale entanglement renormalization

Both matrix-product states and projected entangled-pair states share the property that they emphasize local properties of the system. One could argue that the information necessary to describe a correlation function over a distance of n sites accurately must be distributed over $\mathcal{O}(n)$ different tensors, making it difficult to describe long-range correlations.

A natural way to overcome this limitation would be a tree structure, where a correlation function of distance n would generically involve only $\mathcal{O}(\log n)$ different tensors. Such a structure should be much better suited to describe long-range properties of systems. This is particularly relevant in situations where the physical behavior of a system is dominated by its long-range correlations, such as systems at or close to criticality, where the length scales diverge.

In the following section, we will describe such an ansatz state, the multi-scale entanglement renormalization ansatz, which is a tree-like tensor network state introduced by Vidal [18, 19]. As we will see below, it has many favorable properties, most importantly that i) in one dimension, it can describe critical states with a logarithmic divergence of the entanglement entropy with a fixed bond dimension, ii) in higher dimensions, it can describe the ground states of systems obeying an area law, and iii) it can be contracted exactly in polynomial time.

As its name indicates, the MERA has an interpretation in terms of a renormalization procedure. The renormalization scheme that led to the formulation of the density matrix renormalization group method is inspired by Wilson's numerical renormalization group scheme, which performs the renormalization starting from

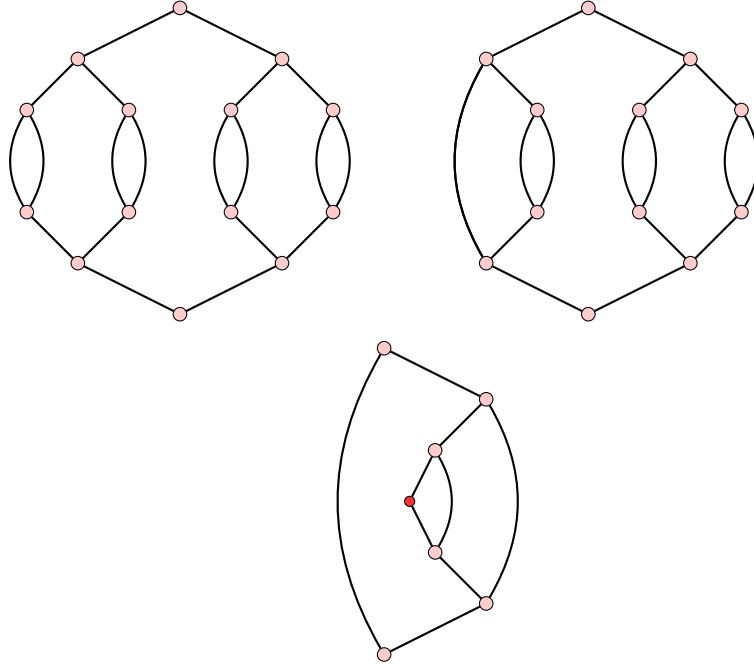


Figure 2.19: Contraction scheme for a tree tensor network. Top left: full tensor network for the identity. Top right: first step of the contraction obtained by using the isometric property of the bottom-left tensor of the state with its complex conjugate. Bottom panel: tensor network (light cone) for a local operator after isometries have been contracted to yield the identity wherever possible.

a small system and adding a number of sites to this system at each step. Pictorially, this can be described by a one-sided tree as shown in Fig. 1.3. A different class of renormalization schemes are coarse-graining procedures; an early example is the Kadanoff block spin method [48]. In these schemes, one starts with a large lattice, and in each step joins a block of sites together to form an effective site, which should have fewer degrees of freedom than the original sites. Iterating this procedure, one either reaches a fixed point for critical systems that lack a characteristic length scale, or reaches some trivial state after a sufficiently large length scale is reached. A tensor network that performs such a procedure is shown in Fig. 2.18.

As for matrix-product states, an important question is how to appropriately choose the RG transformation from the block of sites to an effective site. We will postpone this topic and assume that an algorithm to variationally optimize a tree or MERA structure is known. At a later point, we will revisit the RG picture again and discuss the nature of the coarse-graining transformation induced by the

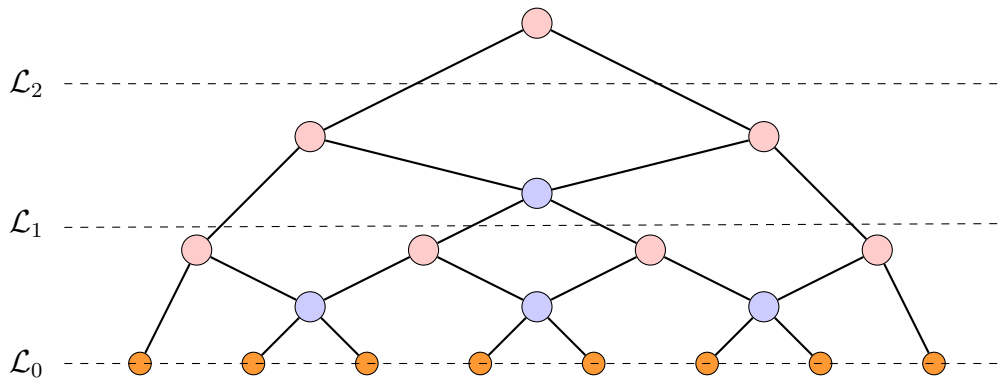


Figure 2.20: Binary MERA structure. \mathcal{L}_0 corresponds to the physical system.

MERA.

Let us discuss in some more detail the tensor network shown in Fig. 2.18. In order to enforce normalization of the state, we require that all tensors are isometric. This is sufficient to enforce that the norm of the state is trivially 1, as each tensor is contracted with its complex conjugate to yield the identity. The first step in the procedure to obtain this result is shown in the top left panel of Fig. 2.19. Furthermore, it is also this property which makes the calculation of local observables possible in polynomial time, as shown in the bottom panel of Fig. 2.19: if an operator is inserted anywhere in the state, the isometric property of the tensors that are not affected by this operator can still be used and only a tensor network of finite width remains to be contracted; this can be achieved in polynomial time. This network will be referred to as *light cone* of the operator.

The shortcoming of such a tensor network state is that it cannot represent an area law for the entanglement entropy at fixed bond dimension. Remember that to capture an area law, the number of bonds that are being cut by a bipartition of the system must grow linearly in the length of the boundary between the two parts. For the tree tensor network, there are always bipartitions that violate this requirement; this is particularly obvious for a binary tree as shown in Fig. 2.18, where the system can always be split in two parts that are only connected at the top of the tree. This argument holds for all dimensions.

In the MERA, this shortcoming is resolved by introducing an additional tensor between each pair of (physical and effective) sites that are not connected by an isometry, as shown in Fig. 2.20. These tensors are referred to as disentanglers, for reasons that will become clear later in the discussion. This introduces additional bonds which have to be cut when partitioning the system, so that a larger amount of entanglement can be captured. In one dimension, the number of bonds that has to be cut for a bipartition is now proportional to the height of the tree, such that

the entanglement entropy is bounded by $\mathcal{O}(\log L)$, where L is the length of the system. In higher dimensions, the number of bonds is linear in the size of the block and an area law is recovered. The disentanglers should be chosen to be unitary in order to enforce normalization and allow contraction in polynomial time; the light cone scheme developed for the tree tensor network can also be applied to the MERA with unitary disentanglers, although with slightly increased computational cost.

Note that for a given dimension and lattice, there is no unique choice of the MERA. The construction shown above is based on a binary tree; even in one dimension, generalizations such as a ternary tree are obvious. In higher dimensions, there are even more possibilities of constructing a MERA. This flexibility permits the optimization of the structure to well describe the physical properties of the system.

As we discussed before, the MERA can be understood as a renormalization group procedure, where each layer of the tree represents a coarse-grained system; in Fig. 2.20, we denote these layers as \mathcal{L}_i , where \mathcal{L}_0 corresponds to the microscopic physical system we started with. A layer of the MERA will be denoted as M_i ; it induces two transformations, namely

- ▷ the *ascending superoperator*, which maps an operator from layers \mathcal{L}_{i-1} to \mathcal{L}_i ,
- ▷ the *descending superoperator*, which maps a reduced density matrix from layers \mathcal{L}_i to \mathcal{L}_{i-1} .

These ascending and descending superoperators play a central role in the algorithm and will be discussed later.

Some important properties of the renormalization group transformation M_i are:

- ▷ It is known that a critical system should represent a fixed point of a renormalization group transformation [95, 96]. This is also the case for the MERA, which implies that one can take a limit of infinite system size by choosing $M_i = M_\infty$ for some $i > i_0$. Usually i_0 is chosen to be larger than 0. This implies that $\mathcal{L}_i = \mathcal{L}_\infty$ for $i > i_0$, i.e. that coarse-grained operators and reduced density matrices reach a fixed point. As we will discuss below, a one-dimensional system for which such a fixed-point transformation can be obtained is described by a conformal field theory; the fixed-point ascending and descending superoperators contain important information about this theory.
- ▷ For a gapped system, which has finite correlation length χ , it is intuitive that only $\mathcal{O}(\log \chi)$ layers of the MERA should be necessary to capture this correlation. Therefore, for sufficiently large i , the reduced density matrices ρ_i should correspond to product states and M_i can be understood as a transformation which reduces entanglement. This explains the name disentangler

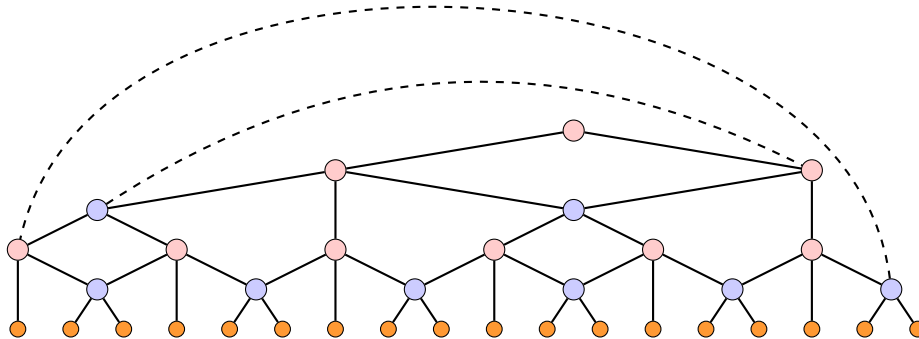


Figure 2.21: The ternary MERA structure used for the numerical calculations throughout this thesis for a chain of 18 sites with periodic boundary conditions (dashed lines are those that wrap around the boundary).

for the unitary operators: their task is to locally remove entanglement from the system, which makes it possible to obtain a product state as limit of the RG transformation.

Different classes of MERA structures are possible:

- ▷ In a **finite, non-translational-invariant** MERA, all tensors are allowed to have different values.
- ▷ By taking all equivalent tensors on a layers to be equal, one obtains a **finite, translationally invariant** MERA. This is only useful for periodic systems. Note that the state will not be translationally invariant on the physical level, as the physical sites are inequivalent if the whole network is considered.
- ▷ In addition, one can take the thermodynamic limit by assuming that all tensors above a certain layer are equal. This **scale-invariant** ansatz is appropriate only for critical systems.

For the purpose of this thesis, we will be interested mostly in the scale-invariant MERA, which permits a direct connection to critical one-dimensional systems described by a conformal field theory. We will consider this topic in more detail in Section 6.

2.3.1 Superoperators

We have mentioned before the concept of ascending and descending superoperators. These play a central role in the construction of the MERA algorithm and should

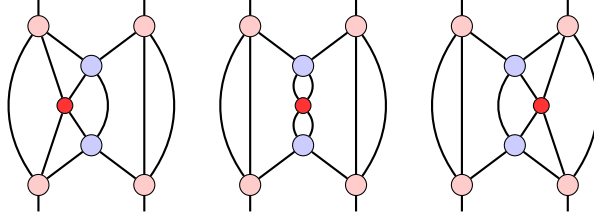


Figure 2.22: Ascending superoperators for the ternary MERA shown in Fig. 2.21. The operator on lattice \mathcal{L}_i is shown in red; the renormalized operator on lattice \mathcal{L}_{i+1} corresponds to the sum of the three contributions. The descending superoperators are easily obtained from these as described in the text.

therefore be discussed at this point. The specific form of these superoperators depends on the MERA structure that is being used. Numerical calculations in this thesis were carried out using a ternary MERA, which is shown in Fig. 2.21. A detailed discussion of technical aspects of the MERA can be found in Ref. [97].

The three contributions to the ascending superoperator of the ternary MERA are shown in Fig. 2.22. These correspond to the three inequivalent ways in which an operator on layer \mathcal{L}_i influences the operator on layers \mathcal{L}_{i+1} . The renormalization of an operator is therefore given by the sum of the three contributions.

The descending superoperator is trivially obtained from the ascending superoperator: the operator on \mathcal{L}_i is removed from the network, and instead the legs that are shown open in Fig. 2.22 are contracted with the density matrix on \mathcal{L}_{i+1} to obtain the density matrix on \mathcal{L}_i . The three contributions again have to be summed up. The computational cost of evaluating these diagrams scales as $\mathcal{O}(\chi^8)$ for this particular MERA structure..

2.3.2 Optimization of a MERA

The expectation value of the energy of the MERA is bilinear in the elements of each tensor, and normalization is implied by imposing that the tensors must be isometric or unitary. However, the optimization of one tensor is coupled to all other tensors, making it a highly nonlinear problem to perform a global optimization. Similar to the approach used for the optimization of the PEPS, the optimization is performed for each tensor separately, which is iterated until convergence is reached. There is of course no guarantee for this procedure to converge to the absolute ground state, but similar to the case of the PEPS, good convergence behavior is usually observed.

For a finite MERA without translational invariance, i.e. where all tensors are different, the energy is bilinear in the tensor W due to a contribution from the state and its complex conjugate. Considering the tensor and its complex conjugate

as separate variables, we have for the energy

$$\langle E \rangle = \text{Tr } eW \quad (2.22)$$

where W denotes the tensor we aim to optimize, and e denotes the rest of the tensor network (environment), including the complex conjugate of W . This network can be efficiently evaluated since the light cone is finite.

We aim to find a new W' such that $\langle E \rangle$ becomes minimal (with fixed environment e) and such that $W'^{\dagger}W = \mathbf{1}$. To this end, we calculate the singular-value decomposition of the environment, $e = USV$. Choosing $W' = -V^{\dagger}U^{\dagger}$, we obtain

$$\langle E \rangle' = \text{Tr } eW' \quad (2.23)$$

$$= -\text{Tr } USVV^{\dagger}U^{\dagger} \quad (2.24)$$

$$= -\text{Tr } S, \quad (2.25)$$

where we have used the cyclic property of the trace. The magnitude of the energy after optimization is therefore equal to the sum of singular values of the environment; also, W' is isometric. It remains to be shown that this indeed is the minimum. Since the product of two unitaries is unitary, it is sufficient to consider (with U, V unitary)

$$\min_V \text{Tr } USV = \text{Tr } (VU)S \quad (2.26)$$

$$= \sum_i S_i (VU)_{ii} \quad (2.27)$$

where $(VU)_{ii}$ denotes the diagonal elements of the matrix product VU , which is also unitary. As the orthonormality of the rows and columns of a unitary matrix U dictates that $|U_{ij}| \leq 1$, the optimal choice is $(VU)_{ii} = -1$, which we achieve by the above choice. Note that with this prescription, the energy is necessarily negative or zero; the physical Hamiltonian should therefore be shifted by some appropriate constant such that all eigenvalues are negative.

This recipe for optimizing a linearized problem of the form (2.22) is the basic ingredient for the optimization of a tensor: starting from some initial guess for W and its conjugate W^{\dagger} , we obtain a W' using the above procedure and replace $W^{\dagger} \rightarrow (W')^{\dagger}$; this is usually iterated several times. This procedure is then repeated for all tensors of the network. For translationally invariant or scale-invariant MERA states, the optimization has to be performed only once for each layer. In these cases, the optimization problem is not bilinear in each tensor, but instead a coupled problem of much higher order; the same approach based on linearization must be applied and usually converges reasonably.

For computing the environment e of some tensor W , the contributions from all light cones containing W must be summed up. In the case of the ternary

MERA, there are six contributions to the environment of an isometry, and three contributions to the environment of a disentangler; for details, we refer to Ref. [97]. For the optimization of a scale-invariant MERA, the contributions from all higher layers must be summed up as described in [97].

2.4 Fermionic tensor networks

Up to this point, we have only discussed tensor networks for systems where operators on different sites commute, such as spin systems and bosonic systems. However, the natural degrees of freedom in a condensed matter systems are usually fermions, which obey anticommutation relations. Many of the most relevant models are indeed fermionic models and it is a natural question to ask whether tensor network states can also be applied in this situation.

For one-dimensional systems, the answer is clear: by means of a Jordan-Wigner transformation, the fermionic system can be mapped to a spin system which can be treated using standard methods. In higher dimensions, such an approach is possible only for finite systems, as a naive Jordan-Wigner transformation will introduce non-local interaction terms with an interaction range of the order of the linear system size. A more systematic approach is therefore needed.

In 2009, several approaches were put forward that allow the definition of fermionic tensor network states that can be treated numerically at a cost comparable to that of bosonic tensor networks. In this thesis, we will focus on the approach described in Refs. [98, 99, 6]; other approaches are found in Refs. [100, 101, 102, 94, 103].

Consider spinless fermions on the lattice with annihilation and creation operators c_i, c_i^\dagger , where i denotes the site on the lattice, and which obey the standard anticommutation relations

$$\{c_i, c_j\} = \{c_i^\dagger, c_j^\dagger\} = 0 \qquad \{c_i^\dagger, c_j\} = \delta_{ij}. \quad (2.28)$$

The Jordan-Wigner transformation is given by

$$c_i = \prod_{j<i} (-2S_j^z) S_i^- \quad (2.29a)$$

$$c_i^\dagger = \prod_{j<i} (-2S_j^z) S_i^+, \quad (2.29b)$$

where S^α , $\alpha = x, y, z, +, -$ are spin- $\frac{1}{2}$ operators. The product over j must be taken along some uniquely chosen path. It can easily be confirmed that these operators fulfill the required anticommutation relations. Consider now a hopping

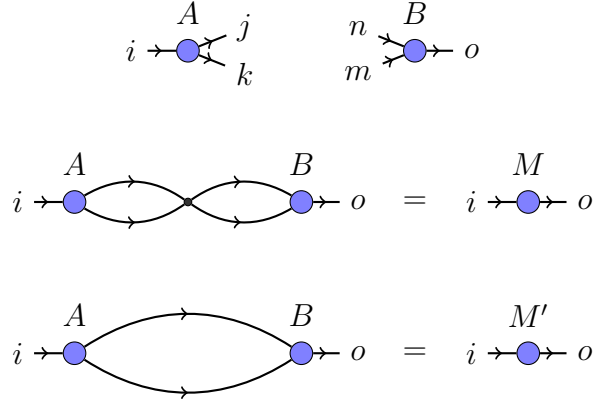


Figure 2.23: Examples of fermionic contractions.

term, where for simplicity we assume $i < j$; a short calculation shows that

$$c_i^\dagger c_j = S_i^+ \left(\prod_{i < l < j} (-2S_l^z) \right) S_j^- \quad (2.30)$$

where we have used the commutator $[S^z, S^+] = S^+$.

For a one-dimensional system with nearest-neighbor hopping only, this confirms that the spinless fermions can be mapped to bosons without additional operators; for long-range hopping terms, it implies a chain of diagonal operators between the two sites. In higher dimensions, such a chain of operators may also be present for nearest-neighbor hopping and will depend on the ordering chosen for the sites. In most cases (with the notable exception of DMRG), this will render tensor network state simulations much less efficient and accurate.

Consider now the contraction of two rank-3 tensors shown in the center panel of Fig. 2.23:

$$M_{io} = \sum_{jkmn} A_{ijk} B_{mno} \delta_{jm} \delta_{kn} \quad (2.31)$$

We can formally associate with each bond a Hilbert space whose dimension equals what we commonly refer to as bond dimension. For the purpose of this discussion, let us restrict the Hilbert space dimension to 2. We can then define either bosonic or fermionic operators that create these two basis states. We will denote these as $a_{[i]}^\dagger$, where the subscript indicates which bond the operator is

associated with. The tensors A, B then become

$$A_{ijk} \rightarrow \sum_{ijk} A_{ijk} (a_{[i]}^\dagger)^i |0\rangle \langle 0| (a_{[j]})^j (a_{[k]})^k \quad (2.32)$$

$$B_{mno} \rightarrow \sum_{mno} B_{mno} (a_{[m]}^\dagger)^m (a_{[n]}^\dagger)^n |0\rangle \langle 0| (a_{[o]})^o \quad (2.33)$$

Now the purpose of the arrows drawn in the figure become clear: they indicate whether operators act on the left or right side of $|0\rangle \langle 0|$. Also, note that we draw legs on the tensor in a fixed order; by convention, we choose a clockwise ordering. Implying summations over all indices, we can write the contraction as

$$M_{io} (a_{[i]}^\dagger)^i |0\rangle \langle 0| (a_{[o]})^o \quad (2.34)$$

$$= A_{ijk} B_{mno} (a_{[i]}^\dagger)^i |0\rangle \langle 0| (a_{[j]})^j \underbrace{(a_{[k]})^k (a_{[j]}^\dagger)^m (a_{[k]}^\dagger)^n}_{\text{brace}} |0\rangle \langle 0| (a_{[o]})^o. \quad (2.35)$$

Using the property $\langle 0| (a_{[i]})^k (a_{[i]}^\dagger)^l |0\rangle = \delta_{kl}$, we can perform some of the sums and recover the original form of the contraction. To this end, we must now commute $(a_{[k]})^k$ and $(a_{[j]}^\dagger)^m$, indicated by the brace. It is at this point where we can introduce the fermionization of a tensor network: if we take the operators a, a^\dagger to obey fermionic anticommutation rules instead of bosonic commutation rules, additional signs will be introduced in this contraction. The two possible outcomes are given below:

$$M_{io} (a_{[i]}^\dagger)^i |0\rangle \langle 0| (a_{[o]})^o \quad (2.36)$$

$$\begin{aligned} \text{(bosonic)} &= A_{ijk} B_{mno} (a_{[i]}^\dagger)^i |0\rangle \langle 0| \overbrace{\left((a_{[j]})^j (a_{[j]}^\dagger)^m \right)}^{\delta_{jm}} \\ &\quad \underbrace{\left((a_{[k]})^k (a_{[k]}^\dagger)^n \right)}_{\delta_{kn}} |0\rangle \langle 0| (a_{[o]})^o \end{aligned} \quad (2.37)$$

$$\begin{aligned} \text{(fermionic)} &= A_{ijk} B_{mno} (a_{[i]}^\dagger)^i |0\rangle \langle 0| \overbrace{\left((a_{[j]})^j (a_{[j]}^\dagger)^m \right)}^{\delta_{jm}} s(m, n) \\ &\quad \underbrace{\left((a_{[k]})^k (a_{[k]}^\dagger)^n \right)}_{\delta_{kn}} |0\rangle \langle 0| (a_{[o]})^o \end{aligned} \quad (2.38)$$

where

$$s(m, n) = \begin{cases} -1 & \text{if } m = 1 \text{ and } n = 1 \\ +1 & \text{otherwise} \end{cases} \quad (2.39)$$

The key observation is that using a tensor network where all operators are fermionic implies also that the physical operators are fermionic! Therefore, such

a network allows the simulation of fermionic Hamiltonians without recourse to a Jordan-Wigner transformation.

The appearance of the sign depends on the specific contraction. For example, consider the contraction shown in the bottom panel of Fig. 2.23,

$$M'_{io} = \sum_{jkmn} A_{ijk} B_{mno} \delta_{jn} \delta_{km}. \quad (2.40)$$

Expressing this in the form of (2.35), one observes that no commutation of operators is necessary and that the contraction can be performed regardless of whether the operators are bosonic or fermionic. As a general rule, additional signs are introduced if lines cross in the tensor network (it is for this reason that the order of legs on the tensor, i.e. the clockwise ordering, is important). We can formally introduce these signs into the tensor network by inserting the *swap gate* $s(m, n)$ at every line crossing of the tensor network. In the implementation of the tensor network, the swap gate can be applied as part of each contraction with only sub-leading cost.

The generalization to bond dimensions higher than 2 is possible using a parity-symmetric basis for each auxiliary Hilbert space such that each state in the Hilbert space corresponds to either an even or odd number of fermions, and restricting each tensor to be parity-symmetric (which they must be for a sensible fermionic theory, as parity is a good quantum number). Symmetric tensor networks will be discussed in more detail in Chapter 3. In terms of the parity quantum number, the swap gate $s(m, n)$ equals -1 if and only if both m and n denote odd-parity states, which corresponds to an exchange of an odd number of fermionic operators.

Another reason for using parity-preserving tensors is that this implies an even number of fermionic operators to be associated with each tensor. Therefore, the tensors that make up the tensor network commute and the order in which contractions are performed does not matter.

We can now formulate the rules for fermionizing tensor networks, which were first given in Ref. [99]:

- i) Use parity-preserving tensors.
- ii) After drawing the tensor network as planar graph, insert swap gates at each line crossing.

The approach has been applied to the MERA [98, 99] and the PEPS [6]. In the latter reference, a number of models were studied, including a solvable model for spinless fermions, a model for interacting spinless fermions and the t - J model, where a comparison to variational Monte Carlo simulations was presented. A more recent demonstration of the usefulness of the approach is found in [104], where the

t - J model was studied in more detail. In an unfinished study, we are currently applying fermionic PEPS to interacting spinless fermions on different lattices and exploring extensions to spinful fermions.

2.5 Complete-graph tensor network states

As we mentioned quickly in Section 2.1 (Fig. 2.3) for the case of a two-dimensional lattice, any system can be mapped to a one-dimensional system in order to perform a simulation based on a matrix-product state. Of course several ordering schemes are usually possible, which may vary greatly in how the system’s entanglement is distributed over the bonds of the MPS. In the case of two-dimensional systems, most schemes can be ruled out as they obviously lead to detrimental entanglement properties for the MPS – but for systems that lack geometric order, it is usually impossible to guess a priori which orderings should be preferred.

The most common situation where this occurs are applications in quantum chemistry. Consider the standard electronic Hamiltonian for a molecule,

$$H = \sum_{\substack{i,j \\ \sigma}} h_{ij} a_{i\sigma}^\dagger a_{j\sigma} + \frac{1}{2} \sum_{\substack{i,j,k,l \\ \sigma,\sigma'}} V_{ijkl} a_{i\sigma}^\dagger a_{j\sigma'}^\dagger a_{k\sigma'} a_{l\sigma}, \quad (2.41)$$

which contains one-electron integrals h_{ij} over spatial orbitals $\phi_i(\vec{r})$ given in non-relativistic theory by

$$h_{ij} = \int \phi_i^*(\vec{r}) \left(-\frac{1}{2} \nabla^2 - \sum_I \frac{Z_I}{r_I} \right) \phi_j(\vec{r}) d^3r, \quad (2.42)$$

with nuclear charge number Z_I of atomic nucleus I and electron–nucleus- I distance $r_I = |\vec{r} - \vec{R}_I|$, and the two-electron integrals V_{ijkl} defined as

$$V_{ijkl} = \iint \frac{\phi_i^*(\vec{r}_1) \phi_j^*(\vec{r}_2) \phi_k(\vec{r}_2) \phi_l(\vec{r}_1)}{r_{12}} d^3r_1 d^3r_2. \quad (2.43)$$

The nucleus-nucleus repulsion term is suppressed for the sake of brevity. For a reference, see [105].

The single-particle orbitals $\phi_i(\vec{r})$ are generally obtained from some preparatory numerical calculation for the specific molecule. These orbitals completely lack geometric structure in the sense that they cannot be regarded as being distributed over sites of a lattice and the mapping to the chain becomes arbitrary. While DMRG calculations based on arranging the orbitals on a chain have nevertheless proven to be accurate [106, 107, 108] and despite many attempts to systematically improve the ordering (for examples see Refs. [109, 110, 111, 112]), a reliable way

to determine a good ordering is not known and the approach is conceptually not satisfying.

In Ref. [4], we have put forward an ansatz that does not rely on a geometric structure for the orbitals, but instead treats all correlations on an equal footing. The ansatz can be regarded as special case of the correlator product states [23], which are generalizations of string-bond states [20] and entangled-plaquette states [22].

The Complete-Graph Tensor Network approximates the coefficients of the wave function in an occupation-number basis by a network of tensors that connects all orbitals with each other:

$$\langle n_1 n_2 \dots n_k | \Psi_{\text{CGTN}}^{(N)} \rangle = \prod_{\alpha} \prod_{\beta \leq \alpha}^k f_{\alpha\beta}^{n_{\alpha} n_{\beta}} \quad (2.44)$$

where α, β run over the orbitals, n_{α} and n_{β} denote their respective occupation. The variational parameters are contained in the $f_{\alpha\beta}^{n_{\alpha} n_{\beta}}$. For a given pair of orbitals α, β , $f_{\alpha\beta}$ is a matrix that encodes the correlation between these two orbitals. A similar ansatz was used by Huse and Elser [113] for a two-dimensional antiferromagnet.

In contrast to the tensor network states discussed so far, the CGTN cannot be contracted by evaluating the trace over a tensor network. Instead, we can either perform the sum over all basis states explicitly or perform a variational Monte Carlo simulation, i.e. sample stochastically over the basis states. Such an approach was first used in the context of tensor network states by Sandvik and Vidal [114].

A key question in variational Monte Carlo methods is how to optimize the parameters. While it is usually possible to sample the gradient and perform some line minimization following its direction, such an approach is very likely to be stuck in local minima. In [114], a stochastic optimization procedure is proposed which takes into account only the sign of the gradient for each element, disregarding the magnitude. In our simulations, we go one step further and use a completely stochastic approach: introducing artificially a temperature T , we can sample configurations \mathbf{f} in the space of variational parameters according to a weight $\exp(-E(\mathbf{f})/T)$, where $E(\mathbf{f})$ is the energy evaluated for a fixed set of variational parameters. We can then use a simulated annealing or parallel tempering procedure to obtain the ground state as limit $T \rightarrow 0$. This approach proves to be more reliable in avoiding local minima than approaches that include gradient information.

In [4], we use this method to study the energy splitting of states of different spin for methylene and the strongly correlated ozone molecule at a transition state structure. These benchmark calculations, which we compare against known results, demonstrate that the ansatz is capable of accurately capturing the energies of these highly entangled molecules.

Chapter 3

Symmetries in tensor network states

In the previous chapter, we have discussed a number of tensor network state algorithms for one- and higher-dimensional systems. They share the property that they can be systematically refined by some parameter M , but suffer from a strong increase of the computational cost. In order to reach large values of M , it is therefore necessary to exploit all possible means of reducing the computational cost. A method to achieve this that is commonly used in exact diagonalization and DMRG calculations is to exploit symmetries, which may in some cases speed up algorithms by more than an order of magnitude.

In exact diagonalization, the Hamiltonian can be brought into a block-diagonal form by rotating to an appropriately chosen basis. The number of blocks equals the total number of irreducible representations of the symmetry group of the Hamiltonian. Since the diagonalization can be performed in each block separately, the computational cost can be reduced significantly. In some cases, it may also help to obtain spectral gaps as the quantum numbers of the state can be fixed. In the case of exact diagonalization, both Abelian and non-Abelian symmetries (including spatial symmetries) can be used. In DMRG calculations, Abelian symmetries are usually exploited [50]. Non-Abelian symmetries have also been considered by some authors [115, 116, 117, 118, 119, 120, 121].

In the context of two-dimensional tensor network state calculations, symmetries have been explored only recently. Parity symmetry (\mathbb{Z}_2) plays a central role in the definition of fermionic tensor networks [6, 100, 101, 98, 99, 102, 94, 103] but has also been shown to be useful for spin systems [122]. Continuous groups, such as $U(1)$, have been used in calculations with the TERG algorithm [123] and the MERA [124, 125]. A general introduction to the topic without numerical results is given in Ref. [126]; Ref. [125] contains a detailed introduction to $U(1)$ symmetry and its use for MERA computations.

In this chapter, which is based on work published in Ref. [7], we will develop a general formalism to implement Abelian symmetries for arbitrary tensor network states. Our approach is implemented in the projected entangled-pair states algorithm and we demonstrate the validity of the necessary approximations by benchmark calculations for the spin- $\frac{1}{2}$ Heisenberg model, which will be discussed in Chapter 5. The approach is also used for the multi-scale entanglement renormalization ansatz in one dimension, which will be used in Chapter 6.

3.1 Symmetry groups

In this section, we will review some important elements of group theory and explain the formalism necessary to define symmetric tensor networks in Section 3.2.

3.1.1 Charge calculus

In the following, we will be concerned with Hamiltonians H with a symmetry group \mathcal{G} , i.e. they commute with the elements of some Abelian group \mathcal{G} , $[H, q] = 0 \forall q \in \mathcal{G}$. This implies that eigenstates of H are also eigenstates of q . We require:

- ▷ There exists a unitary representation U of the group. For $q \in \mathcal{G}$, we have $U^\dagger(q^{-1}) = U(q)$.
- ▷ All representations of the group decompose into a direct sum of irreducible representations \mathcal{V}_i , which can be labelled in correspondence to the eigenvalues of some operator g . We will call these labels c_i .
- ▷ Consider a state $|\phi\rangle \in \mathcal{V}_i$ and $q \in \mathcal{G}$. We then have

$$U(q)|\phi\rangle = \nu(q, c_i)|\phi\rangle \quad (3.1)$$

with $\nu(q, c_i) \in \mathbb{C}$.

Examples will be discussed in Section 3.1.2.

We can classify eigenstates of the Hamiltonian H into the irreducible representations of \mathcal{G} . The associated labels c_i are then called good quantum numbers (for brevity, we will also call them charges or symmetry sectors).

As we will see below, only few properties of the irreducible representations of the group are needed to implement symmetric tensor networks. These are intimately related to the properties of the eigenvalues defined in Eq. (3.1).

Charge fusion Consider two states $|a\rangle \in \mathcal{H}_1, |b\rangle \in \mathcal{H}_2$ with associated quantum number c_1 and c_2 , respectively. Their tensor product in $\mathcal{H}_1 \otimes \mathcal{H}_2$ also has a well-defined quantum number c_3 . We thus define the fusion of quantum numbers

$$c_1 \times c_2 = c_3. \quad (3.2)$$

This corresponds to a labeling of the tensor product of irreducible representations. For the eigenvalues ν , this corresponds to

$$\nu(q, c_1)\nu(q, c_2) = \nu(q, c_3). \quad (3.3)$$

Identity charge There exists an identity charge $\mathbb{1}$ such that $c \times \mathbb{1} = c \forall c$. This implies $\nu(q, \mathbb{1}) = 1$.

Conjugate charge For each charge c , a conjugate charge \bar{c} exists such that

$$c \times \bar{c} = \mathbb{1} \quad (3.4)$$

This implies $\nu(q, \bar{c}) = 1/\nu(q, c)$.

We can easily generalize the above to products of groups. For $\tilde{\mathcal{G}} = \mathcal{G}^1 \times \mathcal{G}^2$, the irreducible representations are $\tilde{\mathcal{V}}_{ij} = \mathcal{V}_i^1 \times \mathcal{V}_j^2$, which can be labelled by $\tilde{c}_{ij} = (c_i^1, c_j^2)$. These labels correspond to eigenvalues of the operator $\tilde{g} = (g^1 \otimes \mathbb{1}, \mathbb{1} \otimes g^2)$. The above calculus is then constructed from element-wise operations on the \tilde{c} .

3.1.2 Examples

An important example is the U(1) symmetry, which is present in systems with particle number conservation and many spin models. For benchmarking purposes, we will apply the symmetric PEPS algorithm to a system of spin- $\frac{1}{2}$ degrees of freedom on the square lattice with Heisenberg interaction. This system has an SU(2) spin rotation symmetry, which in the thermodynamic limit and at zero temperature is spontaneously broken to a U(1) symmetry. We will exploit this symmetry and its finite subgroups.

\mathbb{Z}_2

For Hamiltonians that are invariant under a simultaneous flip of all spins, $|\uparrow\rangle \leftrightarrow |\downarrow\rangle$, the operator

$$g_{\mathbb{Z}_2} = (-1)^{\sum_i \sigma_i^z} = \prod_i \sigma_i^z \quad (3.5)$$

commutes with the Hamiltonian. A unitary representation of the group \mathbb{Z}_2 is given by

$$U(\alpha) = g_{\mathbb{Z}_2}^\alpha \quad (3.6)$$

with $\alpha \in \{0, 1\}$. Its unitarity follows from the unitarity of the Pauli matrix σ^z . The two irreducible representations can be labeled as $c = \pm$. The eigenvalues $\nu(\alpha, c)$ are:

$$\nu(0, +) = +1 \quad \nu(1, +) = +1 \quad (3.7a)$$

$$\nu(0, -) = +1 \quad \nu(1, -) = -1 \quad (3.7b)$$

3.1 Symmetry groups

The fusion rules therefore are:

$$\pm \times \pm = + \qquad \pm \times \mp = - \qquad (3.8)$$

This implies $+$ = $\mathbb{1}$ and $\bar{c} = c$.

Due to the very simple structure with only two irreducible representations and the trivial charge conjugation, the implementation of \mathbb{Z}_2 symmetry is particularly easy.

U(1)

The most commonly used symmetry in simulations with exact diagonalization or DMRG is the U(1) spin symmetry, which is present if the operator

$$g_{\text{U}(1)} = \sum_i \sigma_i^z \qquad (3.9)$$

commutes with the Hamiltonian. This is the infinitesimal generator of a representation of U(1),

$$U(\phi) = \exp(i2\pi\phi g_{\text{U}(1)}), \qquad (3.10)$$

where $\phi \in [0, 2\pi)$.

The irreducible representations can be labeled with integer numbers, $c \in \mathbb{Z}$. The $\nu(\phi, c)$ are

$$\nu(\phi, c) = \exp(i2\pi\phi c). \qquad (3.11)$$

Clearly,

$$\nu(\phi, c_1)\nu(\phi, c_2) = \nu(\phi, c_1 + c_2) \qquad (3.12a)$$

$$\nu(\phi, 0) = 1 \qquad (3.12b)$$

$$\nu(\phi, -c) = \nu(\phi, c)^{-1} \qquad (3.12c)$$

The charge calculus therefore follows the rules of integer addition. The label of the irreducible representations can be interpreted as magnetization of the state. Special care must be taken when forming the adjoint of a vector or operator, since $U(\phi)|\Psi\rangle \rightarrow \langle\Psi|U(-\phi)$. The Hermitian transpose of a state in the irreducible representation c therefore falls into the irreducible representation \bar{c} .

\mathbb{Z}_q

Since for the PEPS, finite groups are easier to deal with, we consider finite subgroups of U(1), namely the cyclic groups \mathbb{Z}_q . We define

$$g_{\mathbb{Z}_q} = \exp\left(\frac{i2\pi}{q} \sum_i \sigma_i^z\right), \qquad (3.13)$$

which naturally also commutes with the Hamiltonian if $g_{U(1)}$ does. The irreducible representations can be labeled with $c \in \{0, \dots, q\}$, where 0 is the identity. A unitary representation is, similar to \mathbb{Z}_2 , given by

$$U(\alpha) = g_{\mathbb{Z}_q}^\alpha. \quad (3.14)$$

where $\alpha \in \{0, \dots, q-1\}$. The eigenvalues $\nu(\alpha, c)$ are

$$\nu(\alpha, c) = \left(e^{i\frac{2\pi}{q}} \right)^{\alpha c}. \quad (3.15)$$

This implies the cyclic property $\nu(\alpha, c+q) = \nu(\alpha+q, c) = \nu(\alpha, c)$. The resulting fusion rule is

$$c_1 \times c_2 = (c_1 + c_2) \pmod{q}, \quad (3.16)$$

therefore

$$\bar{c} = q - c. \quad (3.17)$$

For taking adjoints, the same consideration as in the case of $U(1)$ applies. The implementation of \mathbb{Z}_q symmetry for $q > 2$ is more involved than \mathbb{Z}_2 since charges are not inverse to themselves. The small number of sectors however reduces the technical efforts compared to $U(1)$.

3.2 Symmetric tensor networks

3.2.1 Definition and contraction of symmetric tensors

We define a tensor T as a linear map from a tensor product of Hilbert spaces to the complex numbers:

$$T : \mathcal{H}_1 \otimes \mathcal{H}_2 \otimes \dots \otimes \mathcal{H}_R \rightarrow \mathbb{C}. \quad (3.18)$$

Here, R is the rank of the tensor. The elements of the tensor are $T(v_1, v_2, \dots)$ for $v_k \in \mathcal{H}_k$. Equivalently, if we choose a fixed basis $\{b_i^k\}$ in each \mathcal{H}_k , we can define a tensor as a multidimensional array $T_{i_1 i_2 i_3 \dots}$, where the indices i_k run from 1 to $\dim \mathcal{H}_k$ and

$$T_{i_1 i_2 i_3 \dots} = T(b_{i_1}^1, b_{i_2}^2, b_{i_3}^3, \dots). \quad (3.19)$$

In this chapter, we are interested in states composed of tensors that are invariant under the operations of a group. To define this, let $q \in \mathcal{G}$ and $U^k(q)$ unitary representations in the Hilbert spaces \mathcal{H}_k . We then require

$$T(U^1(q)v_1, U^2(q)v_2, \dots) = T(v_1, v_2, \dots). \quad (3.20)$$

As shown in the Appendix, a tensor element $T(v_1, v_2, \dots)$ vanishes unless

$$\bigotimes_k c_k = \mathbb{1} \quad (3.21)$$

where c_k is the label of the irreducible representation that v_k belongs to. Colloquially, this can be understood as conservation of charge at the tensor. As a direct consequence, if a fixed basis of eigenvectors of the generators is chosen, the multidimensional array $T_{i_1 i_2 i_3 \dots}$ takes a block-sparse form, therefore reducing the number of non-zero parameters.

If we partition the indices to form two groups $\mathcal{I}_1, \mathcal{I}_2$, we can equivalently express the tensor as a linear operator

$$\tilde{T} : \bigotimes_{k \in \mathcal{I}_1} \mathcal{H}_k \rightarrow \bigotimes_{k \in \mathcal{I}_2} \mathcal{H}_k \quad (3.22)$$

where $(\bigotimes_{k \in \mathcal{I}_2} v_k)^\dagger \tilde{T} (\bigotimes_{k \in \mathcal{I}_1} v_k) = T(v_1, v_2, v_3, \dots)$. We refer to \mathcal{I}_1 as in-going and \mathcal{I}_2 as out-going indices. In a pictorial representation, we will associate arrows with the indices. What are the symmetry properties of this operator? As shown in the appendix, it commutes with the group action. Schur's Lemma then implies that for $x \in \bigotimes_{k \in \mathcal{I}_1} \mathcal{H}_k$ in the irreducible representation labeled c , $\tilde{T}x$ is also in the representation c . This is true for all possible partitions of the indices.

We are now ready to discuss the algorithms that form the basic building blocks of any tensor network state algorithm, namely contraction of tensors and mapping to matrices to perform singular value or eigenvalue decomposition. This will be based on the results of the previous sections, namely i) the definition of symmetric tensors in Eqns. (3.19), (3.21), ii) the transformation to a linear operator (3.22), and iii) the charge calculus of Section 3.1.1. In particular, we have obtained a way of implementing tensor networks without knowing explicitly the matrix representations of the group in each (auxiliary) Hilbert space, allowing us to enforce the symmetry on all bonds.

3.2.2 Tensor contraction

We now discuss the most important ingredient of a tensor network algorithm, tensor contraction. Fig. 3.1 shows the steps of the contraction of two rank-4 tensors; these are:

1. We first transform the tensors to operators of the form (3.22) (Fig. 3.1 (a)–(b)). The choices of in-going and out-going indices are dictated by the indices that are being contracted: on one tensor, those indices must be the in-going and on the other the out-going indices. The resulting operators, which are written as a matrix, have a block-diagonal structure.

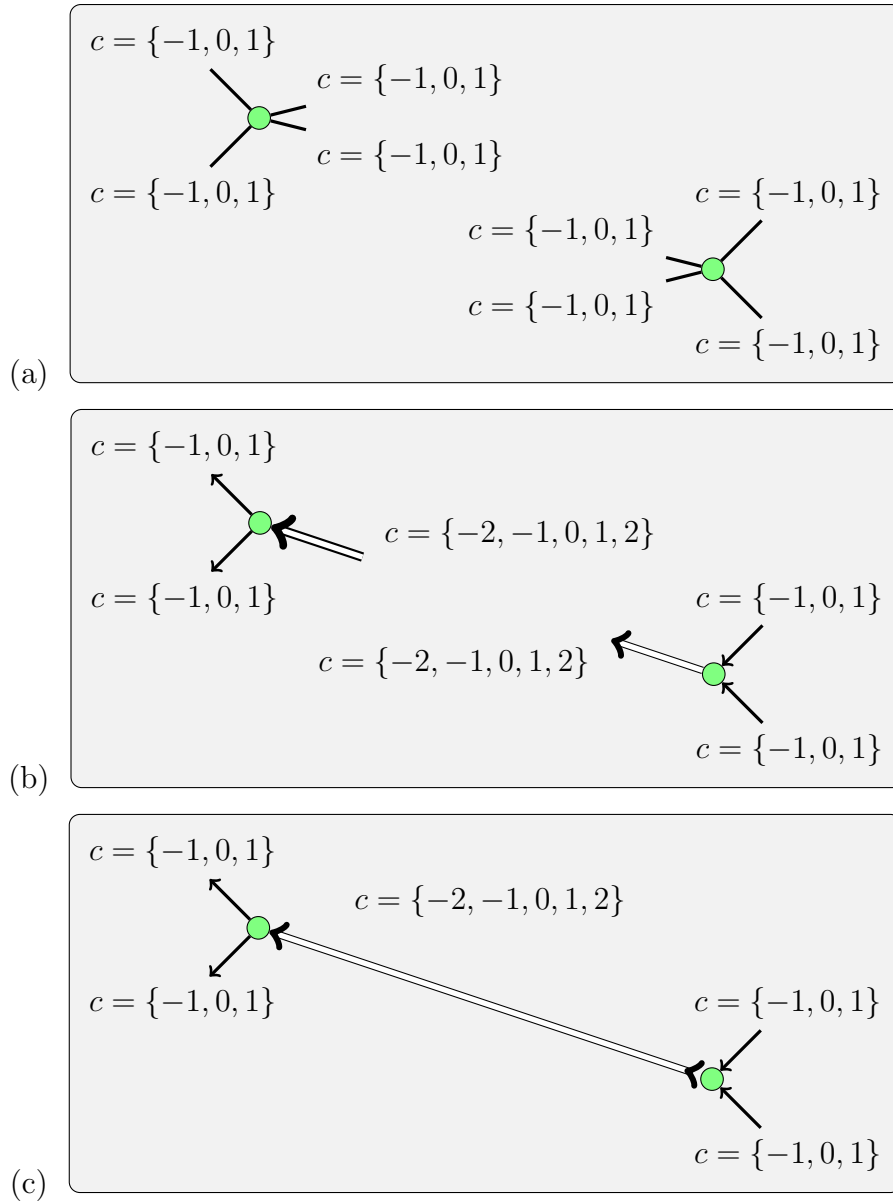


Figure 3.1: Pictorial representation of the contraction of two rank-4 tensors with $U(1)$ symmetry. The steps are explained in detail in Section 3.2.2.

2. The contraction is now equivalent to a matrix multiplication. The blocks must be contracted in such a way that the resulting tensor still satisfies (3.20). Therefore, we must match blocks in such a way that

$$c_{\text{in}} \times c_{\text{out}} = \mathbf{1}. \quad (3.23)$$

3. The resulting tensor, Fig. 3.1 (c), can be converted back to the form of Eqn. (3.18).

The conversion between the forms (3.18) and (3.22) also allows the definition of other linear algebra operations, such as singular value decomposition or eigenvalue decomposition based on the mapping to a matrix. All these share the block-diagonal structure.

3.2.3 Symmetric PEPS

As a simple example of a tensor network, the construction of a matrix-product state invariant under some symmetry group \mathcal{G} is shown in Fig. 3.2. On each bond i of the tensor network, we have a set of charges \mathcal{C}_i . For the bonds connecting to physical degrees of freedom, this set of charges is fixed by the physical Hilbert space. In the case of a finite MPS with open boundary conditions, the set of charges possible on an auxiliary bond is unique and has a well-defined physical meaning: if one were to consider, e.g., a system with particle number conservation, the allowed symmetry sectors on each auxiliary bond in the construction in Fig. 3.2 are the possible particle numbers to the left part of the chain. In general, the set of allowed charges corresponds to the possible fusion outcomes of all physical charges to the left. In a finite system, a quantum number sector can be selected by appropriately fixing the allowed charges at the right end of the chain.

In the case of a PEPS, a unique identification of the charges on an auxiliary bond with the fusion outcomes of a specific region cannot be made. It is therefore not possible to determine uniquely which symmetry sectors must be kept on the auxiliary bonds. While for finite groups, it is usually computationally possible to allow all charge sectors, some choice has to be made in the case of infinite groups. It is therefore an important task to verify that i) for finite and infinite groups, one obtains a good approximation to the ground state by using a PEPS constructed from symmetric tensors, ii) for infinite groups, a reasonable approximation is obtained for computationally feasible choices of the symmetry sectors. Numerical evidence that this is the case will be shown in Section 5.3.

To understand the nature of the approximation introduced by truncating the set of allowed quantum numbers, consider the expansion of a state $|\Psi\rangle = \sum_{|\phi\rangle} c(\phi)|\phi\rangle$.

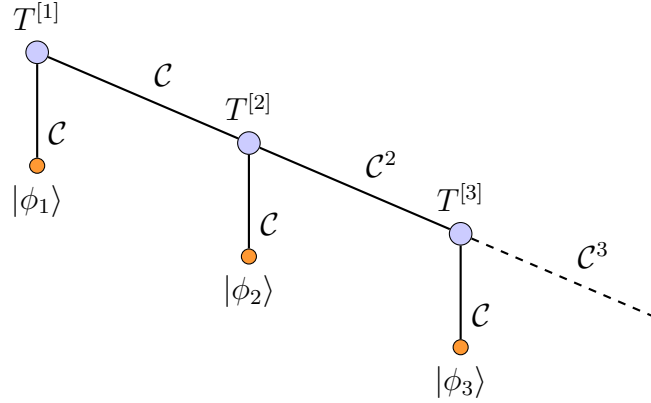


Figure 3.2: End of a matrix product state invariant under some symmetry group \mathcal{G} . $|\phi_i\rangle$ denote physical states in the local Hilbert space \mathcal{H}_{loc} . By \mathcal{C} , we denote the set of charges associated with sectors in \mathcal{H}_{loc} , and by \mathcal{C}^n the set of charges associated with sectors in $\bigotimes_{i=1}^n \mathcal{H}_{\text{loc}}$. The first auxiliary bond to the left simply carries the physical charges of the first site. For the second bond, all possible fusion outcomes of charges on the first auxiliary bond with the physical charges have to be considered. This can be continued up to the middle of the chain, such that each auxiliary bond carries the possible combinations of charges to the left. Joining such a state with its reflection will yield a finite symmetric MPS.

Using a tensor network ansatz amounts to representing all coefficients $c(\phi)$ by a trace over a tensor network, which will represent the low-entanglement subspace of the full Hilbert space efficiently. In principle, all basis states are allowed and could have non-vanishing weight. Imposing restrictions on the quantum numbers, on the other hand, amounts to a restriction on the allowed basis states: the sum does not run over the full basis $\{|\phi\rangle\}$, but only a subset of states compatible with the allowed quantum numbers.

In addition to the charge sectors on each bond, the number of states in each sector has to be chosen. In principle, this could differ between all sectors on one bond and between bonds. The situation becomes more involved since even for a translationally invariant PEPS, several different sets of charges have to be considered, as shown in Fig. 3.3. For the purpose of this chapter, we make the simplification that we choose the charges to be the same on all equivalent bonds of the lattice and the environment states. Additionally, for the case of finite groups, we choose the number of states in each sector the same for all equivalent bonds.

Two points require special attention when applying symmetric PEPS to infinite lattices: i) On infinite lattices, the ansatz is restricted to states that globally fall into the sector of the identity charge. For example, using the $U(1)$ symmetry

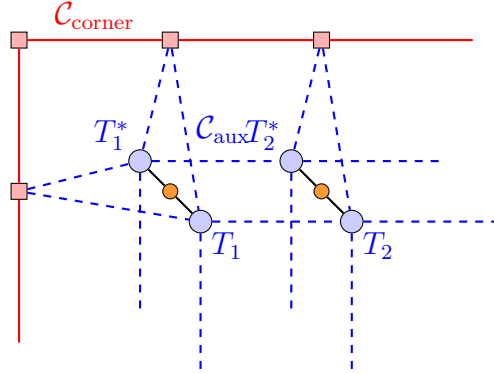


Figure 3.3: Corner of a symmetric PEPS state with an environment as in the directional corner transfer matrix method.[79] Here, the blue circles denote tensors T_i of the ansatz state and their conjugate T_i^* , the red squares denote tensors of the corner transfer matrix and the orange circles represent single-site operators acting on the physical index of the PEPS tensor. In the infinite case, in general there are three sets of charges involved: i) the physical charges $\mathcal{C}_{\text{phys}}$ carried on the black, solid lines in the figure, ii) the auxiliary charges \mathcal{C}_{aux} on the blue, dashed bonds, and iii) the charges carried on the bonds of the environment $\mathcal{C}_{\text{corner}}$. This reflects the three independent bond dimensions involved in a PEPS: the physical dimension d , the bond dimension M and the environment dimension χ . Usually, $M > d$ and $\chi \sim M^2$. Therefore, $\mathcal{C}_{\text{phys}} \subset \mathcal{C}_{\text{aux}} \subset \mathcal{C}_{\text{corner}}$. In principle, all charges could depend on the location in the PEPS or the environment.

of a spin- $\frac{1}{2}$ system described in Section 3.1.2, only states with vanishing total magnetization can be studied. In the case of particle number conservation, an appropriate choice of charges would have to be taken to enforce the desired filling fraction. On finite lattices, however, selecting specific quantum number sectors is possible also in the PEPS construction by adding an external bond carrying the total charge of the system to one of the tensors that make up the PEPS. ii) Since our construction assumes that the state has a well-defined global quantum number, systems that spontaneously break the symmetry that is being exploited cannot be represented. If the possibility of a spontaneous symmetry breaking is present in the system being studied, the results should therefore be checked against calculations without enforcing the symmetry.

In order to confirm the validity of our approach, we have numerically studied the spin- $\frac{1}{2}$ Heisenberg model using $U(1)$, \mathbb{Z}_2 and \mathbb{Z}_q symmetries. Our results clearly confirm the validity of the approach and in particular for finite groups, a significant reduction of computational cost while keeping the accuracy fixed is achieved. We postpone the detailed discussion of these results to Section 5.3.

3.3 Some proofs

In this section, we show in detail some calculations relevant to the discussion in Sect. 3.2.1, in particular symmetry properties of a tensor of the form (3.18).

To simplify the notation, we consider the case of a tensor of rank 2, where the Hilbert spaces are taken to be equal:

$$T : \mathcal{H} \otimes \mathcal{H} \rightarrow \mathbb{C} \quad (3.24)$$

$$\tilde{T} : \mathcal{H} \rightarrow \mathcal{H}, \quad (3.25)$$

where for $x, y \in \mathcal{H}$ we have $T(x, y) = y^\dagger \tilde{T} x$. Also, let U be a unitary representation of the group in \mathcal{H} .

We would like to show the following equivalence:

$$(a) \quad [\tilde{T}, U] = 0 \quad (3.26)$$

$$(b) \quad \Leftrightarrow T(Ux, Uy) = T(x, y).$$

First, we show that (b) follows from (a):

$$\begin{aligned} T(Ux, Uy) &= y^\dagger U^\dagger \tilde{T} Ux \\ &= y^\dagger U^\dagger U \tilde{T} x \\ &= T(x, y) \end{aligned} \quad (3.27)$$

Secondly, we show that (a) follows from (b):

$$\begin{aligned} y^\dagger [T, U] x &= y^\dagger T U x - y^\dagger U T x \\ &= T(Ux, y) - T(x, U^\dagger y) \\ &= T(U^\dagger U x, U^\dagger y) - T(x, U^\dagger y) \\ &= 0 \end{aligned} \quad (3.28)$$

The above can easily be generalized for all operators of the form (3.22).

We now want to show the validity of (3.21). Let $q \in \mathcal{G}$. Then,

$$\begin{aligned} &T(U(q)v_1, U(q)v_2, \dots) \\ &= T(\nu(q, c_1)v_1, \nu(q, c_2)v_2, \dots) \\ &= \nu(q, c_1)\nu(q, c_2) \dots T(v_1, v_2, \dots) \\ &= \nu(q, \times c_k) T(v_1, v_2, \dots) \\ &= T(v_1, v_2, \dots) \end{aligned} \quad (3.29)$$

where we have used Eqns. (3.20) and (3.3). Therefore, $\nu(q, \times c_k) = 1$ and $\times c_k = \mathbf{1}$.

Chapter 4

Implementation of tensor network states

In this chapter, we will sketch how to efficiently implement tensor network states in C++, possibly including symmetries. The objectives of our approach are two-fold:

- ▷ **Good run-time efficiency.** To achieve this, most of the CPU-intensive tasks, like matrix multiplication or singular value decomposition, are performed by external libraries which are optimized for the specific architecture.
- ▷ **Good programming efficiency.** Tensor network states are a fast-moving field with new proposals coming up very frequently, but at the same time, the programming effort is relatively large. In particular, implementing and debugging the contractions involved in the higher-dimensional tensor networks is very time-consuming. An efficient programming model is therefore essential.

Our approach is centered on a high-level C++ library which will aid the programmer in storing and manipulating tensors of arbitrary rank. The interface is constructed to allow a direct translation from a diagrammatic or mathematical notation into the source code, allowing the quick implementation of a variety of tensor network state methods. Also, symmetries can be dealt with at the level of such a library, so that only slight modifications are necessary to include symmetries in any tensor network state algorithm.

4.1 Requirements

To achieve the goals described above, we implement a library that meets the following requirements:

- ▷ **Compatibility with standard matrix layout.** For the CPU-intensive

tasks, we utilize libraries such as BLAS or LAPACK. To this end, we must map all operations to matrix operations. This is an important step in particular for contractions, where instead of summing indices explicitly, we implement the conversion to an appropriate matrix form.

- ▷ **High-level interface for contractions.** The starting point of the implementation of a tensor network method is a set of diagrams, representing the contractions necessary to perform each step of the simulation. The most time-consuming step in the implementation is translating these diagrams into C++ code. A high-level interface is used to simplify this, where the programmer only specifies the names of indices that are to be contracted.
- ▷ **Use of advanced C++ optimizations.** Advanced C++ features, such as template metaprogramming, is used to optimize the computations that are not being performed by low-level library.

There is currently no C++ library available that addresses these problems, in particular the problem of efficient tensor contraction based on a mapping to matrix multiplication, and in the presence of symmetries. Implementations of non-symmetric tensors and the contraction are available in Matlab and Python's NumPy package.

4.2 Symmetries

In this section, we outline a few details of the implementation of symmetries in the tensor library. There are two key elements for symmetric tensors:

- ▷ When the tensor is constructed, the allowed charge sectors and their dimensions must be specified for each leg of the tensor. Together with the convention that all indices are in-going, this completely determines the structure of the tensor.
- ▷ The conversion between a tensor structure and a matrix operator ((3.18) \leftrightarrow (3.22)) must be implemented with symmetries. Performing this efficiently is non-trivial as the correct location within each block of the output matrix must be determined for each element of the tensor.

The latter operation scales linear with the number of matrix elements N and is therefore subleading compared to matrix operations, which scale roughly as $\mathcal{O}(N^{3/2})$. Nevertheless, it has to be implemented very carefully because determining the correct location for each tensor element may introduce a large prefactor.

In Ref. [125], precomputation is suggested as efficient approach for this problem: the correspondence between the location of an element in the tensor and the matrix is calculated once and stored in memory to be reused later. This approach has several downsides: a) the overhead in memory usage may be significant, b) memory

bandwidth is one of the bottlenecks of tensor network state simulations and should therefore be minimized, c) the structure of tensors, in particular for groups such as $U(1)$ where the number of sectors is chosen dynamically, may vary between each iteration of the algorithm.

In our implementation, we do not rely on precomputation. Instead, the correspondence is calculated on the fly in a recursive algorithm that iterates over all elements of the tensor. By fixing the rank of the tensor at compile-time, the necessary recursion and most of the loops involved in the calculation can be inlined using template metaprogramming. The algorithm can be run in two ways such that elements are either read sequentially and written in an unstructured way, or vice versa. Benchmark calculations show that the bottleneck is not the calculation of the location for each element, but the memory bandwidth for unstructured memory access.

4.3 Interface

4.3.1 Identifying indices

In order to be able to specify contractions and matrix-based operations, a mechanism for labeling indices is necessary. Many implementations, such as the one in Matlab, enumerate the indices and leave it to the user to assert the correct identification of the numeric labels. We aim for a simpler and less error-prone procedure, where at the time of creation of a tensor, the user specifies alphanumeric labels which can be referred to when specifying contractions.

The obvious choice for these labels would be to use `C++` strings. However, manipulating strings at run-time is rather expensive and may lead to significant overhead. To avoid this, we use an `enum` type for the labels. The user can therefore still write alphanumeric names, but the `C++` compiler will convert these labels to integer numbers at the time of compilation, so that the run-time overhead becomes negligible. The downside is that the `enum` containing all possible labels has to be defined at some early point in the code. To automate this, we use a small Python script which collects the possible labels from the code and assembles the `enum` definition.

4.3.2 Defining tensors

To specify a tensor, the user must provide, for each index, a list of allowed quantum numbers and their respective dimensions.

```
1 REGISTER(a , b , c , d , e , b1 , b2 , b3 , in1 , in2 , out );
```

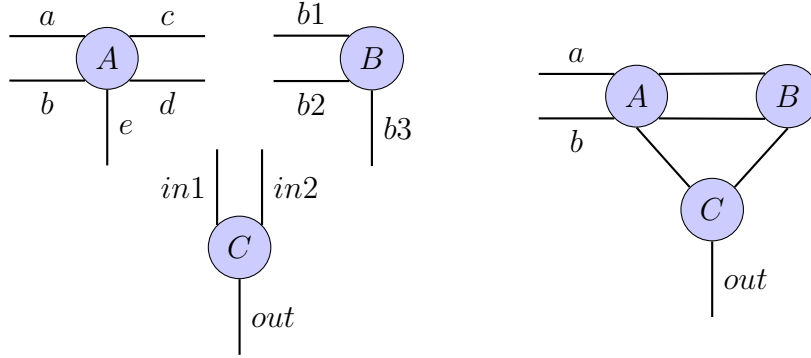


Figure 4.1: Example of a tensor network, whose implementation is discussed in the main text.

```

6  tensor<double,5,grp> A(( PIndex<grp>(a,M,C),
                           PIndex<grp>(b,M,C),
                           PIndex<grp>(c,M,C),
                           PIndex<grp>(d,M,C),
                           PIndex<grp>(e,M,C)));
11 tensor<double,3,grp>
    B(( PIndex<grp>(b1,M,C),
        PIndex<grp>(b2,M,C),
        PIndex<grp>(b3,M,C))),
    C(( PIndex<grp>(in1,M,C),
        PIndex<grp>(in2,M,C),
        PIndex<grp>(out,M,C)));

```

Here, M can be an integer or a vector of integers defining the number of states in each quantum number sector, and C is a list of allowed quantum numbers on the bond. If M is a scalar, the dimension is assumed to be equal in each quantum number sector; if C is omitted, a default set of quantum numbers may be used, if defined by the symmetry group. Of course, both M and C may be different for each leg, but must match between legs that are to be contracted.

The rank of the tensor is a template parameter, i.e. it has to be specified at compile time. This is generally not a restriction, as the ranks of all tensors involved are known at the time of writing the program. Many optimizations of the code are based on knowing the rank at compile-time; for example, recursive algorithms that would be used for example for rearranging tensor elements can be optimized using template meta-programming.

The template parameter `grp` specifies the symmetry group. This should be a class that defines the type of charge (quantum number) and the fusion rules for the charges. For \mathbb{Z}_q symmetry, the class definition is:

```

1  template<int Q> class ZqCharge {
    friend ZqCharge operator+(ZqCharge a, ZqCharge b) {
        return ZqCharge((a.c_+b.c_)%Q);
    }
5  public:
    ZqCharge(unsigned int c = 0) : c_(c) { }
    ZqCharge operator-() const {
        return c_ == 0 ? 0 : Q-c_;
    }
10 protected:
    unsigned int c_;
};
template<int Q> class Zq
{
15 public:
    typedef ZqCharge<Q> charge;
    static const int q = Q;
    static charge fuse(charge a, charge b) {
        return a+b;
20 }
};

```

The symmetry therefore has to be specified at compile-time. This allows many compiler optimizations, since operations on the charges have to be executed very often.

REGISTER() is a macro that is not evaluated by the C++ compiler, but instead is used by the aforementioned Python script to identify all possible index names. The file created by this Python script would look like this:

```

1  enum Index {
    a,b,/* ... */out
};
inline std::string IndexName(Index idx)
5  {
    switch (idx) {
        case a: return std::string("a");
        // ...
    }
10 }
inline Index IndexName(const std::string &idx)
{
    if (idx == std::string("a")) return a;
    // ...
15 }

```

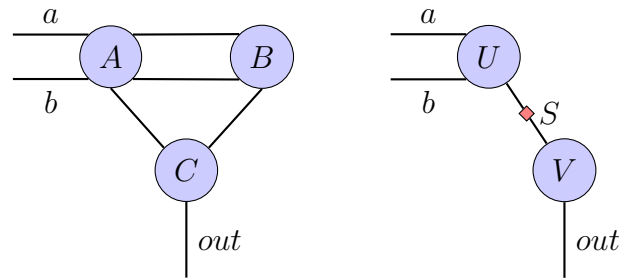


Figure 4.2: ...

The `IndexName()` functions allow the conversion between `enum` and `string`, which is useful for debugging and disk storage purposes.

4.3.3 Specifying contractions

For an example of how to create tensors and specify their contraction, see the small tensor network shown in Fig. 4.1. The contraction of this network is performed in two steps, first contracting A and B over the index pairs (c, b_1) and (d, b_2) , and then contracting the resulting tensor with C over the pairs (e, in_1) , (b_3, in_2) . The C++ code to perform this contraction is shown below:

```

1  tensor<double,4,grp> temp;
   tensor<double,3,grp> result;
   temp.contraction((a,b,e,c,d),A,
                   (b1,b2,b3),B);
5  result.contraction((a,b,e,b3),temp,
                    (in1,in2,out),C);

```

An alternative code to perform the same task, which is equivalent at run-time, is:

```

1  tensor<double,3,grp> result =
   A((c,d),(b1,b2),B)
   ((e,b3),(in1,in2),C);

```

The main advantage of the second alternative is that the user does not have to create temporary tensors.

4.3.4 Matrix operations

Tensors can always be converted to matrix by grouping some indexes. While this function can in principle be called directly by the user, the library is designed in such a way that matrix operations, like singular value decomposition, can be called directly without the need to explicitly convert to a matrix.

```
1 REGISTER(k);
2 tensor<double,3,grp> U;
  tensor<double,2,grp> S,V;
  int keep=-1;
  results.SVD((a,b),_(out),
              SV_TO_NONE,k,keep,AllCharges()),
7          U,V,&S);
```

Here, `SV_TO_NONE` indicates that the singular values should not be multiplied into the adjacent tensors (other options are `SV_TO_LEFT` and `SV_TO_RIGHT`), `k` is the name for the newly created index on `U` and `V`, `keep` indicates how many singular values should be kept (where a value of -1 indicates that all should be kept), and `AllCharges()` indicates that no truncation of the quantum number sectors should be performed. `S` is passed as a pointer so that a default value of `NULL` can be passed if the user does not need the singular values. Adapting the code to perform a truncation below some cutoff weight can easily be done.

Chapter 5

The accuracy of projected entangled-pair states

In the previous sections, we have discussed why tensor network states promise to be a useful tool for studying strongly correlated quantum systems. However, the arguments are not sufficient to determine whether with the amount of computational resources available on current machines, a sufficient bond dimension can be reached to accurately describe the physical properties of interesting systems for condensed matter theory. In the case of matrix product states, a bond dimension ranging from several thousands up to tens of thousands is possible, and it has been demonstrated innumerable times that the method is very accurate for one-dimensional systems. In the case of PEPS, the bond dimension is limited to at most a dozen for the PEPS, and even this can only be achieved at the sacrifice of additional approximations. It is therefore very important to confirm the reliability and accuracy of PEPS for some models where results are well-known, for example from quantum Monte Carlo calculations.

In this section, which is based on work published in Refs. [1, 7], we will study several examples of spin systems without frustration, where results can easily be compared to known results and Quantum Monte Carlo calculations, which we perform using the ALPS package [127, 128]. We will first discuss the origin of these models and why they are relevant test cases for tensor network state methods. We will then show results for a series of increasingly difficult systems studied without exploiting symmetries in the simulations. In the last section, we will discuss the improvement achieved by exploiting symmetries as discussed in Chapter 3.

5.1 Non-frustrated spin systems

Spin systems arise in two different contexts: as models for magnetic materials, and as effective models for interacting fermionic or bosonic systems around certain limits. Historically, they first appeared in the quest for microscopic models for ferromagnetism. A first phenomenological explanation for magnetism was given by the molecular field theory of Weiss. In this context the famous Ising model was invented as a microscopic picture for Weiss' theory. However, it did not deliver a satisfying explanation: Ising showed that it does not order in one dimension, and suggested that this should also be true in higher dimensions [129]. More importantly, the forces that lead neighboring spins to align in parallel did not come out of a first principles quantum mechanical calculation, but instead were merely a postulate.

A big step forward was taken by Heisenberg in [130], where a quantum mechanical treatment of a linear chain of atoms with a single valence electron is given. The big step forward in this calculation was to consider the magnetic moments to be localized at the atoms and consider the kinetic term as a perturbation, instead of taking interactions as perturbation. A presentation that is closer to the modern notation is given in Ref. [131], where the model is described in terms of diagonal and off-diagonal terms acting on the representation of the magnetic state in the S_z -basis. Arguments in favor of ferromagnetic order for higher-dimensional systems are also discussed. Shortly after, the model was solved in one dimension by the famous Bethe ansatz [132]. These discussions pertain mostly to the ferromagnetic case.

A different context in which the *antiferromagnetic* Heisenberg model is obtained was first realized by Anderson [133], who derives it perturbatively for a system of localized electrons in a diamagnetic background. This derivation is closely connected to the derivation from the Hubbard model [134] by perturbing in t/U at half filling and $U = \infty$. Consider a model of electrons located on N sites of a regular lattice, where i) there is exactly one electron per site, ii) placing two electrons of different spin on the same site increases the energy by a large amount U , and iii) placing two electrons of equal spin on one site is not allowed due to Pauli exclusion. The Hamiltonian for this system is given by

$$H_{\text{int}} = U \sum_i c_{i\uparrow}^\dagger c_{i\uparrow} c_{i\downarrow}^\dagger c_{i\downarrow}, \quad (5.1)$$

where $c_{i\sigma}^\dagger$ creates a fermion with spin σ at site i .

It is diagonal and the energies can easily be read off; as all spin configurations have the same energy, the ground state manifold has dimension 2^N and contains all states where each site is occupied by one electron. We now introduce a hopping

term proportional to t such that electrons can reduce their energy by hopping to adjacent sites:

$$H_{\text{kin}} = -t \sum_{\langle i,j \rangle} (c_{i\sigma}^\dagger c_{j\sigma} + \text{h.c.}) \quad (5.2)$$

This (partially) lifts the degeneracy between spin states: at second order in perturbation theory, spin configurations where an electron is surrounded only by electrons of different spin polarization become favorable, since they permit exchanging two electrons without violating the Pauli exclusion. This leads to an effective antiferromagnetic Heisenberg coupling.

A few decades later, the Heisenberg model reappeared, this time in the field of superconductivity, and again due to a paper by Anderson [135]. Therein, it was doubted that the Heisenberg model develops magnetic order at zero temperature, at least under circumstances where frustration enhances the role of quantum fluctuations. Such frustration effects appear for example when taking into account higher order terms of the aforementioned expansion of the Hubbard model in t/U ; another example are non-bipartite lattices. It was argued that the ground state could be a resonating valence bond state, where pairs of electrons form singlets. These singlets were considered candidates for a pairing mechanism in high-temperature superconductors.

At least for the case of the square lattice Heisenberg model with only nearest-neighbor interactions, while a rigorous proof of the existence of long-range order is still missing, there is overwhelming numerical evidence for the existence of antiferromagnetic order. The most accurate method to date is Quantum Monte Carlo, e.g. in Ref. [136]. Recently, accurate results have also been obtained with DMRG [137]. In the presence of frustration, the phase diagram is not fully understood and an active area of research.

5.1.1 XXZ model in external field

Let us now turn our discussion to a generalized version of the Heisenberg model, the XXZ model in external field. We consider spin- $\frac{1}{2}$ particles on the square lattice, with the Hamiltonian

$$H = \sum_{\langle i,j \rangle} \left(\frac{J_{xy}}{2} (\sigma_i^+ \sigma_j^- + \sigma_i^- \sigma_j^+) + J_z \sigma_i^z \sigma_j^z \right) + h \sum_i \sigma_i^z \quad (5.3)$$

where $\sigma^x, \sigma^y, \sigma^z$ denote Pauli matrices and $\sigma^+ = \sigma^x + i\sigma^y$, $\sigma^- = \sigma^x - i\sigma^y$. By identifying $a_i = \frac{\sigma_i^+}{2}$, $a_i^\dagger = \frac{\sigma_i^-}{2}$, $n_i = \frac{\sigma_i^z + 1}{2}$, this model can be mapped (up to a

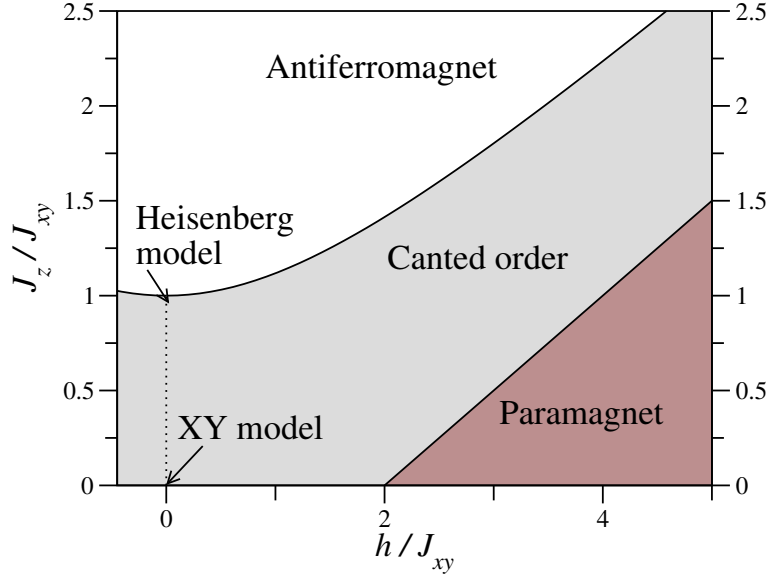


Figure 5.1: Schematic phase diagram of the XXZ model for $J_{xy} = 1, h \geq 0, J_z \geq 0$. For a description of the phases, see Sect. 5.1.1. The phase diagram is symmetric with respect to the line $h = 0, J_z \geq 0$.

constant) the Bose-Hubbard model in the limit of hard-core bosons, given by

$$H = -t \sum_{\langle i,j \rangle} (a_i^\dagger a_j + a_j^\dagger a_i) + V \sum_{\langle i,j \rangle} n_i n_j + \mu \sum_i n_i, \quad (5.4)$$

where the parameters are translated as $J_{xy} = -\frac{t}{2}, J_z = \frac{V}{4}, h = \frac{\mu+V}{2}$.

The phase diagram of this model has been studied to much detail and is well understood [138, 139, 140]. The schematic phase diagram is shown in Fig. 5.1. In the full phase diagram, the model has a U(1) symmetry related to magnetization conservation. At $h = 0$, there is in addition a \mathbb{Z}_2 symmetry related to the spin flip $|\uparrow\rangle \rightarrow |\downarrow\rangle$. At $h = 0$ and $J_z = J_{xy}$, i.e. for the Heisenberg model, the symmetry is enlarged to the full SU(2) symmetry. In the following discussion, XY and Z identify the axes in spin space, not in real space. Three different phases can be identified:

Paramagnet A large magnetic field forces the system into a paramagnetic state, where all spins are aligned in the Z-direction. In the bosonic language, it corresponds to a full or empty state, depending on the sign of the chemical potential. As no spontaneous symmetry breaking occurs, the system is gapped. It is short-range correlated and therefore also very weakly entangled. The magnetization along the field can be used to characterize this phase.

Antiferromagnet In the antiferromagnetic phase, the coupling in Z-direction dominates and spins align antiferromagnetically in this direction, which implies that translation symmetry is broken. As the U(1) symmetry is not spontaneously broken and there are no Goldstone modes, the system has a gap. Away from the phase transition around $h = 0$, the state is weakly entangled. The staggered magnetization in Z direction must be used to characterize this phase. It should not display a staggered magnetization in the XY plane.

Canted phase This phase interpolates between the paramagnet and the antiferromagnet: starting from the paramagnetic phase, the increasing XY coupling leads to the spins bending down towards each other, hence the name. The U(1) symmetry of spin rotation in the XY plane is broken and a staggered magnetization in the XY plane is observed. This leads to gapless modes and the system is therefore much more strongly entangled than the antiferromagnetic and paramagnetic phases. In the bosonic model, this phase corresponds to a superfluid, where particle number conservation is spontaneously broken.

The transition from the paramagnet to the canted-order phase is of second order; the transition from the canted-order phase to the antiferromagnet is of first order, as discussed in detail below. The transition at $J_z = 0$ was studied using iPEPS in Ref. [83].

5.1.2 The spin-flop transition: iPEPS at a first-order phase transition

The nature of the transition from the canted order to the antiferromagnetic phase, referred to as spin-flop transition, was under debate for some time. The existence of a different type of order on both sides of the phase transition excludes the possibility of a direct continuous phase transition between the two phases. The two remaining possibilities are a first-order transition and a series of two continuous transitions with a very small intermediate phase, where both types of order coexist. In the bosonic model, this would correspond to a so-called supersolid phase [141, 142], where superfluidity and long-range crystalline order coexist. Early Monte Carlo simulations [143] indeed seemed to confirm the presence of a small phase of coexisting order in the hard-core boson model. A few years later, Monte Carlo simulations were repeated, taking into account the possibility of phase separation at a first order transition, and found that this is the more likely scenario [144]. This was confirmed in further studies [138, 139, 140].

The iPEPS method is very suitable to first-order phase transitions. Orús et al [145] studied a phase transition in the anisotropic quantum orbital compass model

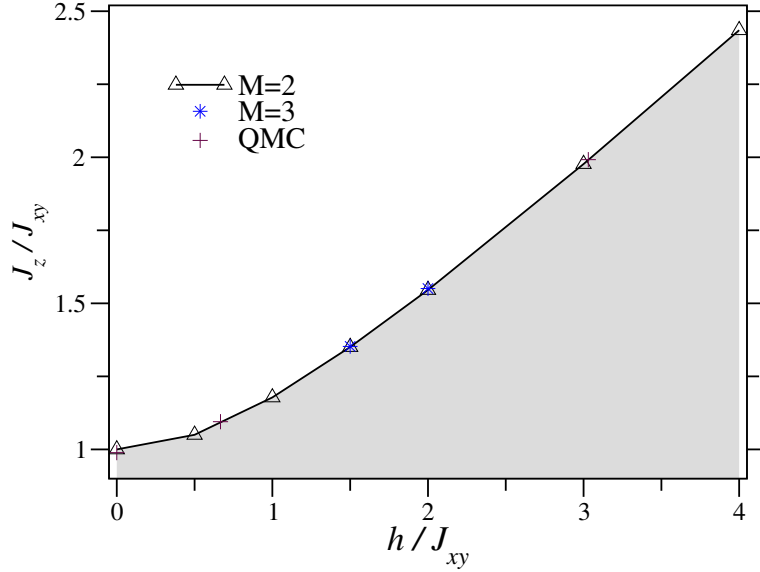


Figure 5.2: Spin-flop transition of the XXZ model. Lines are guides to the eye and interpolate the results for an iPEPS with bond dimension 2. The QMC results are taken from Yunoki [140].

and located the transition point using adiabatic time evolution. We will take a different approach based on the observation that the dynamics close a first-order phase transition differ fundamentally between simulations on finite lattices and on infinite lattices with translational invariance.

If the system is taken across the phase transition from phase A to phase B, phase A becomes meta-stable. Since phase A cannot locally be continuously deformed into phase B (assuming pure states), the dominant process by which the meta-stable state decays is the condensation of finite clusters of phase B (see, e.g., Binder [146]), which necessarily breaks translational symmetry. This process is suppressed by enforcing translational symmetry. The imaginary time evolution we simulate therefore has a strongly suppressed probability of tunneling from one phase to the other in the phase coexistence regime where the energy densities of phase A and B are similar.

We can therefore expect to find only homogeneous systems of one phase in the vicinity of the transition. By preparing a state deep within one phase and using this state as initial state for the imaginary time evolution of the Hamiltonian with different parameters, we can find the energy density of each phase for a relatively wide space of parameters. The transition point can then be located to high accuracy as the crossing point of the ground-state energy densities of the two phases; simultaneously, the existence of this stability allows us to clearly

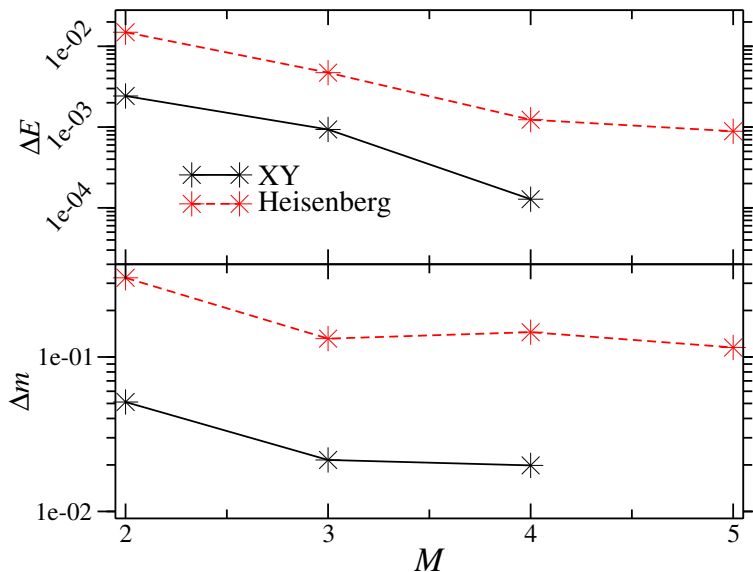


Figure 5.3: Convergence of relative errors $\Delta x = |x(\text{iPEPS}) - x(\text{QMC})|/|x(\text{QMC})|$ with bond dimension M . Monte Carlo results from [136, 147] are taken as exact. For the definition of the magnetization refer to the text.

distinguish the nature of the phase transition.

If the coexistence of two different types of order is observed in an iPEPS simulation, it cannot be due to coexistence of the two phases, i.e. phase separation. This is in strong contrast to simulations of finite systems, where due to the equal energy density of the two phases at or close to the transition point, bubbles of one phase may exist within the other, rendering the interpretation of data difficult.

The results we obtain for the spin-flop transition are shown in Fig. 5.2. The results for $M = 2$ already match very well with the QMC results. The change with $M = 3$ is very minor; at $h = 1.5$, the relative difference between the critical coupling is on the order of 0.1%. A very small M is therefore sufficient to characterize this phase transition with very good accuracy. Similar results were simultaneously found in Ref. [84].

5.1.3 Heisenberg and XY model

In the beginning of this chapter, we discussed the relevance of the Heisenberg model for magnetism and as effective model for interacting fermions. It is clearly a relevant test case for two-dimensional long-range ordered SU(2) antiferromagnet. An accurate description has long been sought for, until it was finally obtained by Quantum Monte Carlo. Due to its large symmetry group, there are three

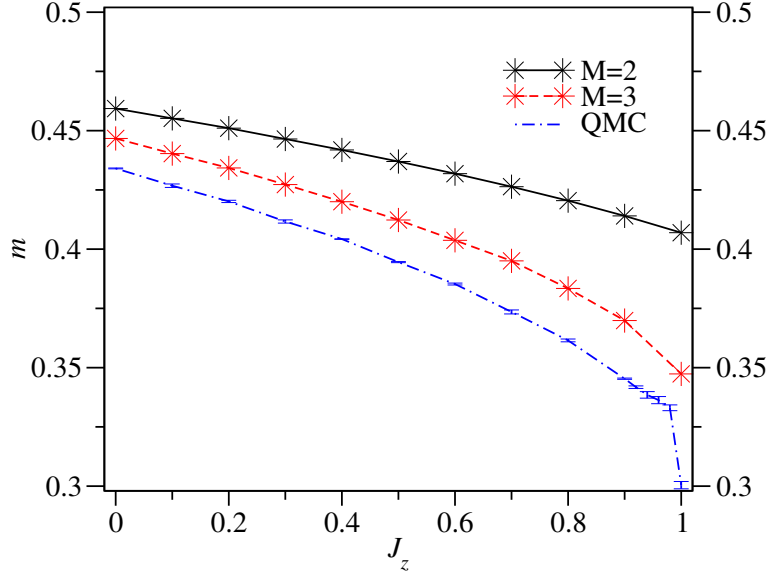


Figure 5.4: Magnetization m (cf Eqn. (5.5)). The error increases significantly as the isotropic Heisenberg model is approached. The restoration of the full SU(2) symmetry at that point leads to a significant decrease of the magnetization, which is not correctly captured by iPEPS for the M we considered. Finite size scaling was performed for the Monte Carlo calculations.

Goldstone modes, which renormalize the magnetization significantly compared to the classical Néel state. These fluctuations lead to a large amount of entanglement in the ground state, even though it is an ordered phase. We therefore expect it to be a difficult test case for tensor network state methods.

The XY model is similar, but has a smaller symmetry group. Its U(1) symmetry is spontaneously broken, which introduces one Goldstone mode. The fluctuations away from the Néel state are weaker than in the Heisenberg model, which leaves the magnetic moment closer to that of the classical Néel state.

In Fig. 5.3, results for the energy and the spontaneous magnetization are shown, where the magnetization m is defined as (subscript indices denote the site in the unit cell)

$$m = \frac{1}{2} \langle m_k \rangle_{\text{unit cell}} \quad (5.5a)$$

$$m_k = \sqrt{\sum_{i=x,y,z} \langle \sigma_k^i \rangle^2}. \quad (5.5b)$$

$\langle \sigma^z \rangle$ vanishes for all $J_z < J_{xy}$. The data clearly shows that while energies are captured very well for both models, the large quantum fluctuations away from

the Néel order, in particular for the isotropic case, are not captured by a PEPS of small dimension very well, leading to a significant error in the magnetization. Interestingly, the energy for the Heisenberg model decreases strictly monotonously with increasing M , while the magnetization does not improve significantly from $M = 3$ to $M = 4$ (this can also be seen in Fig. 5.6). This illustrates that in gapless models, states with varying physical properties may lie very close to each other in energy, which impairs the ability of variational simulations to obtain accurate results.

Figure 5.4 shows the magnetization as the coupling is tuned from the limit of the XY model to the isotropic Heisenberg model, i.e. J_z is tuned from 0 to J_{xy} . In the Monte Carlo data, it is interesting to note that the magnetization drops very quickly close to the isotropic point. It is in particular this large drop that is not well described by the PEPS data for small values of the bond dimension, leading to the large deviation of the magnetization at the isotropic point.

Figure 5.4 shows how the decrease of the magnetization as J_z is tuned from 0 to J_{xy} is captured by the PEPS; in particular the rapid decrease as the SU(2) symmetry is restored is not seen in the PEPS calculation.

5.1.4 Dimerized Heisenberg model

It has been demonstrated several times that PEPS on infinite lattices work well at the quantum phase transition of the two-dimensional Ising model in transverse field [71, 79]. In these publications, the authors were able to show that the location of the critical point can be determined with excellent accuracy, and even the critical exponent for the magnetization can be extracted. However, from an entanglement point of view, the transition in the Ising model seems particularly simple: the phases on both sides of the transition are weakly entangled phases, as one phase is a simple paramagnet, and the other a long-range ordered ferromagnet, which however only breaks a discrete symmetry and therefore remains gapped.

The study of the Ising model is therefore not sufficient to assess the accuracy of PEPS for more general classes of phase transitions. To obtain insights about the accuracy in more challenging situations, we study a phase transition in an SU(2) symmetric model. We consider a dimerized Heisenberg model given by the Hamiltonian

$$H = \sum_{\langle i,j \rangle} J^{(i,j)} \vec{\sigma}_i \vec{\sigma}_j, \quad (5.6)$$

where we choose the couplings $J^{(i,j)}$ inhomogenously according to the pattern shown on the left in Fig. 5.5. For $J' = 1, J = 0$, the state is made up of isolated singlets on the strong-coupling bonds; although these dimers are uncorrelated, the

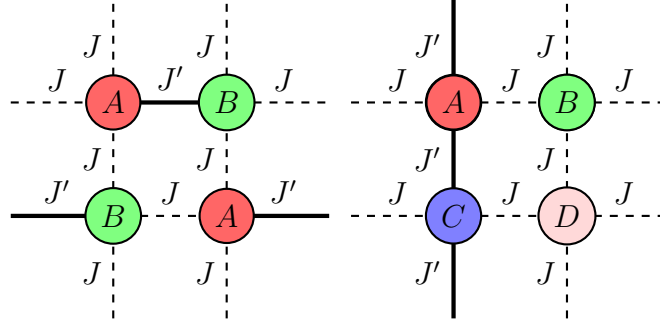


Figure 5.5: (color online) Different dimerization and unit cell patterns. The pattern on the left, which we refer to as *staggered* pattern, is described by a unit cell with two independent tensors and used for the dimerized Heisenberg model. For $J' = 0$, the honeycomb lattice is obtained. The second pattern, referred to as *columnar* pattern, is used in the frustrated cases, but requires 4 instead of two independent tensors. The thick, solid bonds carry couplings J'_{xy}, J'_z , the dashed lines carry couplings J_{xy}, J_z .

state cannot be described at mean-field level. In the limit $J = J'$, the isotropic Heisenberg model is recovered, which, as discussed above, is a strongly entangled phase that poses challenges to tensor network state methods. Between these limits, a second-order phase transition occurs. A recent investigation using Quantum Monte Carlo [148] located the critical point precisely, but raised some questions about the universality class; for further discussions of this topic, see e.g. Ref. [149].

In Fig. 5.6, the order parameter for the phase transition, the staggered magnetization (Eqn. (5.5)) is shown for several values of the bond dimension M ; for comparison, we show results obtained with Quantum Monte Carlo. The iPEPS results clearly indicate the presence of a phase transition; the singularity at the critical point gets sharper as the bond dimension is increased. The location of the critical point is however not obtained to high accuracy with these simulations, but a large improvement is seen between $M = 3$ and $M = 4$. We have however not attempted to extrapolate this, as there are too few points to allow a reliable fit. Also, we have not attempted to extract critical exponents, as this would require data with much higher accuracy.

In the iPEPS simulation, the antiferromagnetic region is found to be larger than it should be. This can be attributed to the fact that breaking the $SU(2)$ symmetry reduces entanglement and is therefore preferred by tensor network state methods.

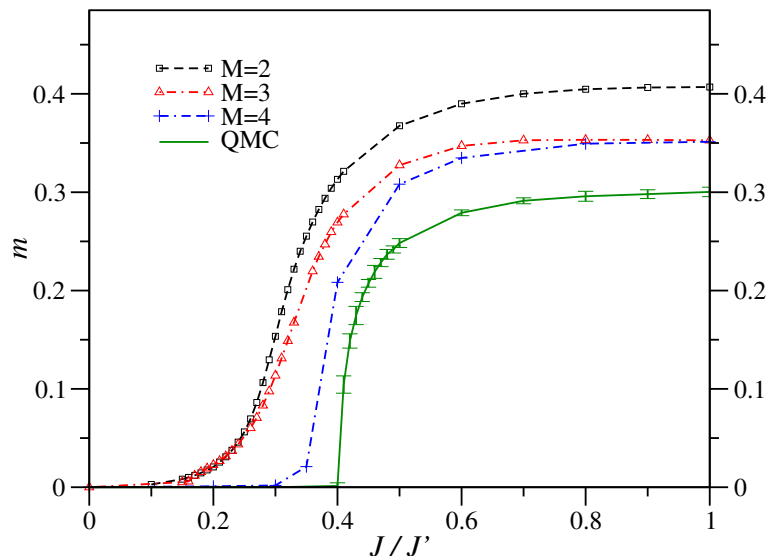


Figure 5.6: (color online) Staggered magnetization of the dimerized Heisenberg model as a function of the coupling ratio. $J/J' = 1$ corresponds to the isotropic Heisenberg model, while $J/J' = 0$ corresponds to isolated dimers on every second horizontal bond.

5.2 Frustrated XY Models

To study the applicability of the iPEPS method to frustrated quantum models, we have studied a phase transition in the family of models obtained by choosing the signs of the different couplings as shown in Fig. 5.5 in such a way that the product around each plaquette is negative, i.e. $JJ' < 0$. The class of models allows a large degree of freedom in the choice of parameters. In particular, we can choose full Heisenberg coupling $J_{xy}^{(i,j)} = J_z^{(i,j)}$ or restrict the coupling to the XY plane, $|J_{xy}| > 0, J_z = 0$.

The case of Heisenberg couplings on the staggered pattern has been studied by Krüger et al [150] using the Coupled-Cluster Method and Exact Diagonalization. The authors find a phase transition from the antiferromagnetic state in the non-frustrated limit to a hexatic phase. Classically, this occurs at a coupling ratio $J'/J = 1/3$; in the quantum model, the antiferromagnetic phase is stable up to $J'/J \approx 1.35$. While the phase transition is second-order in the classical case, it is conjectured to be of first order in the quantum case. The hexatic phase for this pattern however has a large magnetic unit cell which renders it unsuitable for simulation with an infinite, translationally invariant ansatz. In the following

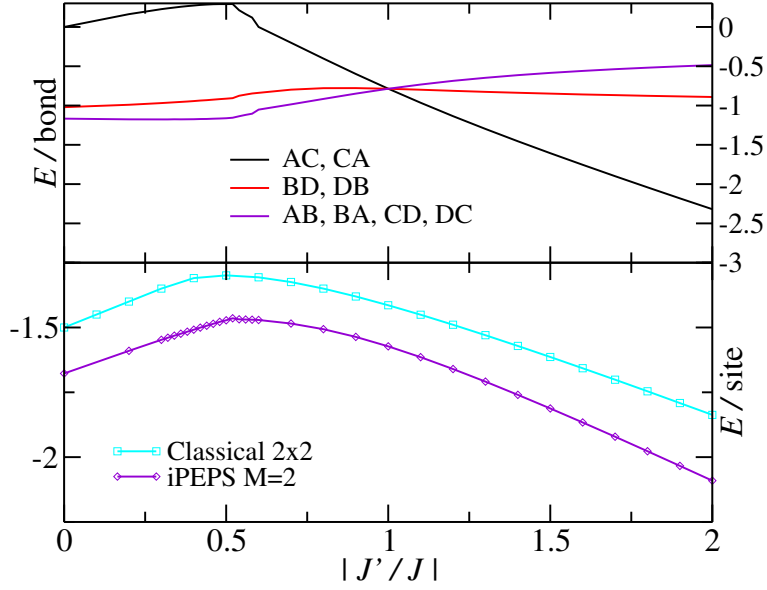


Figure 5.7: (color online) Energies for the different bonds and comparison of energies for the classical and quantum columnar frustrated XY model.

discussion, we will therefore focus on the case of XY coupling and the columnar configuration with $J = -1$.

Classical analogues of spin- $\frac{1}{2}$ systems can be obtained by replacing the quantum spins with Ising (\mathbb{Z}_2), XY ($O(2)$) or Heisenberg ($O(3)$) spins. Equivalently, one can consider mean-field solutions of the quantum system since for spin- $\frac{1}{2}$ degrees of freedom, the mean-field approximation to a Hamiltonian of the form

$$H = \sum_{\langle i,j \rangle} J_x^{(i,j)} \sigma_i^x \sigma_j^x + J_y^{(i,j)} \sigma_i^y \sigma_j^y + J_z^{(i,j)} \sigma_i^z \sigma_j^z, \quad (5.7)$$

can be mapped exactly to a classical Hamiltonian for Heisenberg spins. We can therefore choose to either solve a classical system or perform a mean-field simulation, which we can do simply by minimizing the energy of an iPEPS state with bond dimension $M = 1$. In this case, the renormalization procedure described above reduces to the multiplication with a scalar which cancels for all physical observables.

The classical system has been studied by Villain [151] and solved for the case of $|J'| = |J|$ with Ising and XY spins. For XY spins on the columnar pattern, a two-fold degenerate hexatic state is found, which exhibits a 2×2 site unit cell. Using numerical mean-field calculations on a 2×2 unit cell, we locate a second-order phase transition from a ferromagnetically ordered state to the hexatic state at $J'/J = 1/3$. Our result for $J'/J = 1$ complies with the result by Villain.

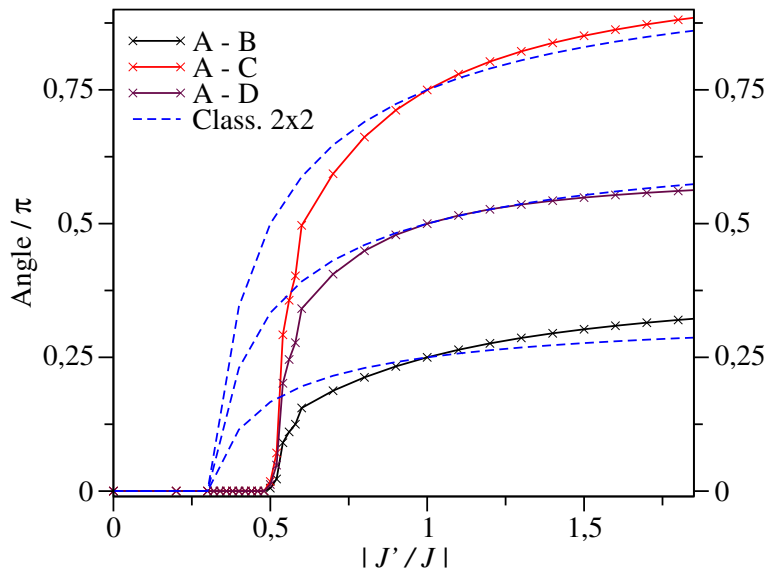


Figure 5.8: (color online) Relative angles between the magnetizations in the XY plane for the quantum and classical columnar frustrated XY model, which is equivalent to a mean-field solution of the quantum model. Notice that at maximal frustration, the angles for the classical and quantum case coincide. The transition is shifted from $J'/J = 1/3$ to a larger value of $J'/J \approx 0.45$.

To simulate the quantum system beyond mean-field, we use an iPEPS ansatz with $M = 2$ and a 2×2 unit cell. The classical ground state is used as initial state for the iPEPS simulation, since this improves stability and convergence speed of the algorithm. We measure the energy on each bond and the relative angles between the spins in the XY plane. For the ferromagnetic configuration, these are 0; for $\angle(AC) = \angle(AB) = \pi, \angle(AD) = 0$, the state is antiferromagnetic. Between these limits, a hexatic state is found. Therefore, the angles can be used as order parameters for the phase transition.

In Fig. 5.7, the energy for each bond and a comparison of the total energy per site to the classical result is shown. For the non-frustrated case, $J' = 0$, we can also compare to Quantum Monte Carlo results. The energy found with iPEPS for $M = 2$ is $E_0 = -1.676$, while the Monte Carlo results for small lattices extrapolate to $E_0 = -1.683(1)$. The relative error of $\Delta E = 0.0042$ is comparable to that obtained for the XY model on the square lattice.

We find that the magnetization always remains in the XY plane and is reduced by quantum fluctuations to a value on the order of $m \approx 0.45$; at all points except the maximally frustrated point $J' = J$, the magnetization is different on the AD and BC sublattices. The angles as a function of the coupling ratio are shown in Fig. 5.8. They indicate a phase transition analogous to the classical one, which however

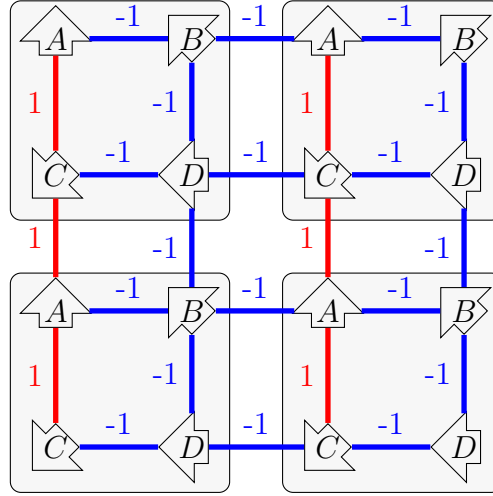


Figure 5.9: (color online) Ground state of the columnar-pattern frustrated model with $J_{xy} = -1$ and $J'_{xy} = 1$. Four magnetic unit cells are shown for illustration purposes. The arrows indicate the magnetization in the XY plane (up to global rotation). The angles of the quantum ground state are identical to those of the classical ground state.

is shifted towards a higher critical coupling of around $J'/J = 0.45$. This agrees with previous results indicating that quantum fluctuations stabilize the collinear order in this class of models.

The state at the point of maximal frustration, $|J'/J| = 1$, is shown in Fig. 5.9. The state corresponds directly to Villain's solution up to a reduction of the magnetization on each site to $m \approx 0.451$. We have cross-checked this result by starting the simulation with different initial states.

In order to investigate the order of the phase transition, we can study the stability of a state upon quenches of the parameters that take the system across the phase transition as discussed in Sect. 5.1.2. In our simulations, we do not observe such stability of the state, indicating that the transition remains continuous in the presence of quantum fluctuations.

5.3 The accuracy in the presence of symmetries

In Chapter 3, we have developed a formalism for symmetric tensor networks, i.e. tensor networks where an Abelian symmetry of the physical Hamiltonian is used to constrain the form of the tensors that make up the state. However, for two-dimensional tensor networks like the PEPS, it is not a priori clear that such a symmetric tensor network will be as accurate as the standard algorithm; this is

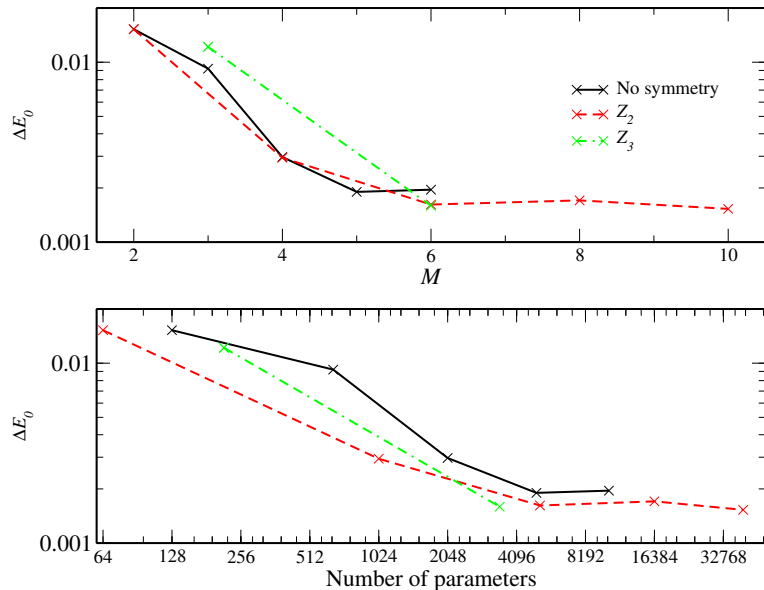


Figure 5.10: The first panel shows how the relative error in the energy decreases as M is increased, for different choices of the symmetry group. The second panel shows the same data versus the number of variational parameters in the state (note the logarithmic scale on both axes). Clearly, the fact that the relative errors are similar between symmetry groups for a given M shows that reducing the number of parameters and the computation time by using larger (finite) symmetry groups does not lead to any loss in accuracy.

in contrast to matrix-product states, where this is clear. We therefore need to establish the accuracy of the method by comparing to known results for some test cases.

In this section, we discuss the accuracy of symmetric PEPS exploiting $U(1)$ and \mathbb{Z}_q symmetry focusing on the isotropic Heisenberg model as a test case. We obtain results with the simplified update described in Section 2.2.2; the directional corner transfer matrix is used to extract expectation values.

5.3.1 Finite groups

The results we obtain for the Heisenberg model with finite symmetry groups \mathbb{Z}_2 and \mathbb{Z}_3 are shown in Fig. 5.10 as a function of the total bond dimension on the bonds of the state and as a function of the total number of variational parameters of the state (note the logarithmic scale in this case). For comparison, we show results obtained with a non-symmetric PEPS, but with the same simplified update

n	M	M_c	Parameters	Comparison \mathbb{Z}_2
3	6	2-2-2	2048	5184
5	8	1-2-2-2-1	4800	16384
5	9	1-2-3-2-1	8128	26244
5	10	2-2-2-2-2	10240	40000
5	11	2-2-3-2-2	15680	58564
7	14	2-2-2-2-2-2-2	28672	153664

Table 5.1: The table shows the choices of symmetry-sector dimensions for the $U(1)$ symmetry in the Heisenberg model. The columns contain i) the number of sectors associated with quantum numbers $S_z = -(n-1)/2 \dots (n-1)/2$, ii) the total bond dimension, iii) the size of each sector, iv) the total number of parameters of the state, v) the total number of parameters in a \mathbb{Z}_2 -symmetric state with the same total bond dimension.

scheme. We choose the number of states equal in each sector, hence $M = q \cdot n$. We also make the same choice on all bonds of the PEPS. We keep up to 36 states in the renormalization of the corner transfer matrices.

For $n > 1$, that is with a non-trivial dimension in each symmetry sector on the auxiliary bonds, the energies obtained with the symmetric PEPS are comparable to those obtained without symmetry for the same bond dimension. This demonstrates that the approximation introduced by restricting the structure of the tensors is valid and does not affect the accuracy. Since all matrix operations decompose into q blocks, we can expect a speedup of $\mathcal{O}(q^3)$ of the algorithm. In terms of the number of variational parameters, a significant improvement is achieved: with \mathbb{Z}_2 symmetry, only half the number of variational parameters is necessary. With \mathbb{Z}_q symmetry, the reduction is even stronger. This may be advantageous particularly if a direct energy minimization algorithm is applied instead of the imaginary time evolution.

In some cases, the energy of the symmetric state falls below the energy of the non-symmetric state. This must be attributed to trapping in local minima, which seems more likely in the case of a non-symmetric PEPS with more variational parameters.

5.3.2 $U(1)$

While for the finite groups considered so far, we could simply keep all allowed sectors of the symmetry on each auxiliary bond, some choice must be made for the infinite group $U(1)$. Furthermore, we have to choose the dimension within each

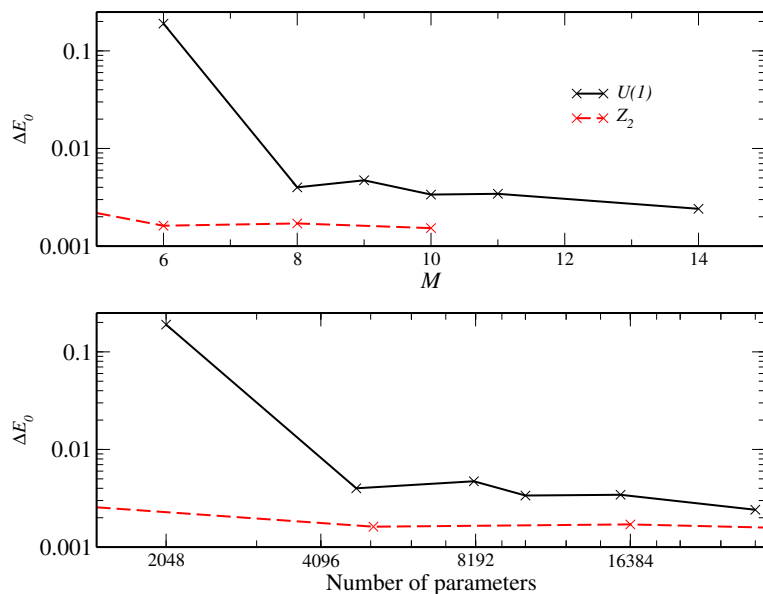


Figure 5.11: Relative error in the ground state energy of the 2d Heisenberg model with a $U(1)$ -symmetric PEPS, as a function of i) the total bond dimension, ii) the number of parameters. The choice of sectors and dimensions is shown in Table 5.1. We show results with Z_2 symmetry for comparison.

symmetry sector – due to the large number of sectors, it is generally not efficient to keep it the same in all sectors, as we did for finite groups. However, given the fast growth of computational cost with the bond dimension, only a few choices are possible. The choices we considered are listed in the table in Fig. 5.1. It should be noted that for equal total bond dimension M , a state with more symmetry sectors of smaller dimension is computationally less expensive since all matrix computations can be split into more blocks. This allows us to study states with very large bond dimension up to $M = 14$, which would be intractable otherwise.

Results obtained with the above choices are shown in Fig. 5.11. The accuracy for a given bond dimension is worse than with the finite group Z_2 ; even for the very large bond dimensions studied with $U(1)$ symmetry, the accuracy does not reach the level of the finite symmetry groups. This is a clear signature that the approximation we made by imposing a $U(1)$ -symmetric structure on the tensors and picking only a few allowed sectors of the symmetry limits the accuracy of the simulations. One has to keep in mind, however, that the number of variational parameters is reduced much more strongly than in the case of finite groups, as shown in the last column of Table 5.1.

Chapter 6

Supersymmetric lattice fermions

The study of supersymmetry has its origins in the field of particle physics, where it allows the construction of quantum field theories containing both bosonic and fermionic excitations which are related by the supersymmetry. Such field theories are considered promising candidates for extensions of the standard model of particle physics and may solve some of the open problems encountered in the field today.

At the same time, supersymmetry has found applications in many other fields of physics. In this chapter, we will study it in a very different context than the particle physics problems where it was first used. Instead of relativistic quantum field theories, we will discuss a class of models for interacting lattice fermions which by construction are supersymmetric. The notion of supersymmetry in this context will be introduced in Section 6.1.1. Several analytical methods are available only for supersymmetric models; for an overview of these approaches, see Ref. [152].

The models we study were first suggested in Refs. [153, 154], where the model on the chain was solved explicitly using the Bethe ansatz. Exploiting the additional tools that are available due to supersymmetry, further aspects of these models were understood: Using the Witten index and cohomology arguments, the number of ground states and some of their properties on several two-dimensional lattices were obtained in [155, 156]. This was used to demonstrate that the models exhibit surprising properties such as superfrustration [155], an exponential degeneracy of the ground state which is not lifted by quantum fluctuations. The case of the chain was analyzed in more detail: in Ref. [157], the authors explore properties of the ground state for finite systems. The spectrum and its relation to superconformal field theory was explored in detail in Ref. [158]. Recent advances include the study of perturbations of the model which preserve supersymmetry, namely staggered interactions [159, 160, 161].

The main purpose of this chapter will be to explore the properties of the model on the square ladder. It has been shown to be critical and is conjectured to be

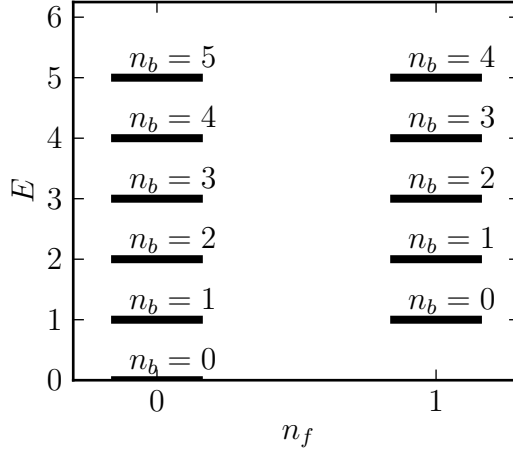


Figure 6.1: Spectrum of the supersymmetric harmonic oscillator with quantum numbers n_f, n_b . Key feature is the two-fold degeneracy between fermionic ($n_f = 1$) and bosonic ($n_f = 0$) states for all eigenvalues except the ground state at $E = 0$.

described by the second $\mathcal{N} = 2$ supersymmetric minimal CFT [156, 152], but this could not be confirmed numerically to this point. Instead, the spectrum shows severe discrepancies with the minimal model, for which no explanation has been found. In this thesis, we apply several approaches to this model in order to confirm its critical theory.

6.1 Supersymmetric lattice fermions

In the following, we will first introduce the basic notion of supersymmetry by the example of the supersymmetric harmonic oscillator, where we will closely follow the description of Ref. [162]. We will then move on to describe a supersymmetric model of interacting lattice fermions, which will be the focus for the rest of this chapter.

6.1.1 A single-particle example: the supersymmetric harmonic oscillator

Consider the standard harmonic oscillator, which, in appropriate units, is given by

$$H = p^2 + \frac{x^2}{4} \quad [x, p] = i. \quad (6.1)$$

Rewriting this into the standard raising and lowering operators, defined by

$$a = \frac{x}{2} + ip \qquad a^\dagger = \frac{x}{2} - ip \qquad [a^\dagger, a] = 1, \quad (6.2)$$

we have

$$H = a^\dagger a + \frac{1}{2}. \quad (6.3)$$

What does it mean to introduce supersymmetry into the harmonic oscillator? This is rather trivial physically, but nevertheless contains all the formal ingredients for $\mathcal{N} = 2$ supersymmetry. Let us define the operators

$$Q = a\psi^\dagger \qquad Q^\dagger = a^\dagger\psi, \quad (6.4)$$

where ψ, ψ^\dagger are fermionic annihilation and creation operators with the commutation relations

$$\{\psi, \psi^\dagger\} = 1 \qquad \{\psi, \psi\} = \{\psi^\dagger, \psi^\dagger\} = 0 \quad (6.5)$$

which commute with the bosonic operators. Consider now the Hamiltonian

$$H^s = \{Q, Q^\dagger\} \quad (6.6)$$

$$= a^\dagger a + \psi^\dagger \psi \quad (6.7)$$

$$= n_b + n_f. \quad (6.8)$$

Its eigenvectors can be written in an occupation number basis $|n_b, n_f\rangle$, where due to fermionic statistics $n_f \in \{0, 1\}$, and $n_b \in \{0, 1, \dots\}$ is the normal occupation number of the harmonic oscillator. The eigenstates are in correspondence to the eigenstates of the standard harmonic oscillator, $|n_b, n_f\rangle = |n\rangle \otimes |f\rangle$, where $|n\rangle$ are the eigenstates of the harmonic oscillator and $|f\rangle$ are the occupied and empty state in the fermionic Hilbert space.

Clearly, for $n_f = 0$, the spectrum of the Hamiltonian H^s is in one-to-one correspondence to that of the standard harmonic oscillator, up to a shift of $\frac{1}{2}$. The ground state is non-degenerate, whereas all other eigenvalues are two-fold degenerate, with one state in each sector of the fermion number:

$$\langle 0, 0 | H | 0, 0 \rangle = 0 \quad (6.9)$$

$$\langle n_b, 1 | H | n_b, 1 \rangle = \langle n_b + 1, 0 | H | n_b + 1, 0 \rangle \quad (6.10)$$

$$= n_b + 1. \quad (6.11)$$

In addition to the obvious symmetries, $[H, n_b] = [H, n_f] = 0$, Q and Q^\dagger are symmetries by construction,

$$[H, Q] = [H, Q^\dagger] = 0. \quad (6.12)$$

Finally, we have the anticommutation and nilpotency conditions

$$\{Q, Q\} = \{Q^\dagger, Q^\dagger\} = 0 \quad (6.13)$$

$$Q^2 = (Q^\dagger)^2 = 0. \quad (6.14)$$

Together, Eqns. (6.6), (6.13) and (6.14) form the $\mathcal{N} = 2$ supersymmetric algebra. The characteristic properties of these systems are

- ▷ a ground state with $E = 0$ if supersymmetry is unbroken,
- ▷ a two-fold degeneracy of excited states with one state in the "fermionic" (here, $n_f = 1$) and "bosonic" ($n_f = 0$) sector,
- ▷ conserved quantities Q, Q^\dagger .

Q and Q^\dagger are referred to as supercharges. \mathcal{N} refers to the number of supercharges, where in this case Q and Q^\dagger are considered separate supercharges despite their obvious relation.

As indicated above, this is merely a toy model, in particular since the bosonic and fermionic operators are not at all coupled in the Hamiltonian. Indeed, making a single-particle problem supersymmetric is possible whenever the potential permits a factorization into the form (6.6), which is true for a large class of one-dimensional potentials. The purpose of this exercise was therefore only to introduce the formal requirements for $\mathcal{N} = 2$ supersymmetry; in the next section, we will apply the same construction to a non-trivial model of interacting fermions.

6.1.2 A many-particle model

We will now construct explicitly a model for supersymmetric lattice fermions. This model was first described in Refs. [153, 154]. Let d_i^\dagger be a fermionic operator that creates a "hard-core fermion"; by hard-core, we mean that it has an infinite nearest-neighbor repulsion, or equivalently it can only be created if the adjacent sites are empty. We can define these in terms of normal fermionic operators c_i with the help of a projection operator

$$P_i = \prod_{\langle i, j \rangle} (1 - n_j), \quad (6.15)$$

where $\langle i, j \rangle$ denotes pairs of nearest neighbors. Note that P_i commutes with c_j and c_j^\dagger if either $i = j$ or i and j are not nearest neighbors; furthermore, $P_i^2 = P_i$. The operators d_i^\dagger are now defined as $d_i^\dagger = c_i^\dagger P_i$.

To obtain a supersymmetric model, we define as supercharges

$$Q^\dagger = \sum_i c_i^\dagger P_i \quad (6.16)$$

$$Q = \sum_i c_i P_i. \quad (6.17)$$

Without the hard-core projection, the supersymmetric Hamiltonian $H = \{Q, Q^\dagger\}$ becomes trivial:

$$H = \sum_{i,j} c_i^\dagger c_j + \sum_{i,j} c_i c_j^\dagger \quad (6.18)$$

$$= \sum_i (c_i^\dagger c_i + c_i c_i^\dagger) + \sum_{i \neq j} (c_i^\dagger c_j + c_i c_j^\dagger) \quad (6.19)$$

$$= \sum_i (n_i + (1 - n_i)) + \sum_{i \neq j} (c_i^\dagger c_j - c_j^\dagger c_i) \quad (6.20)$$

$$= \sum_i 1. \quad (6.21)$$

With the hard-core projection and i, j nearest neighbors, however,

$$P_j c_j c_i^\dagger P_i = 0 \quad (6.22)$$

$$P_i c_i^\dagger c_j P_j \neq 0, \quad (6.23)$$

so that the cancellation in the second term of (6.20) does not occur for pairs of nearest neighbors. One finds that the Hamiltonian in this case is given by

$$H = \sum_{\langle i,j \rangle} (P_i c_i^\dagger c_j P_j + P_j c_j^\dagger c_i P_i) + \sum_i P_i \quad (6.24)$$

The first term is a hopping term dressed with the hard-core projection; the second term can be interpreted as a potential term whose precise structure will depend on the lattice. The Hamiltonian preserves the number of fermions, $[H, \sum_i n_i] = 0$. We identify states with an odd number of particles as "fermionic" states, and "bosonic" otherwise. We will discuss the properties of this model on two specific lattices, the chain and the square ladder, in Sections 6.3 and 6.4, respectively.

6.2 Conformal field theory

In Section 1.2, we discussed the phenomenon of universality and scale-invariance of critical systems, which were both explained first by renormalization group theory.

For two-dimensional classical or one-dimensional quantum systems, conformal field theory was later established as an extremely powerful theoretical tool, which allows a very profound understanding of universality and many other aspects of criticality.

Conformal field theory is a widely studied subject and the literature is extensive. In this section, we will review a selection of basic concepts which are relevant for numerical studies of quantum phase transitions in one dimension. This section is mostly based on material from Refs. [163, 164].

6.2.1 Conformal symmetry in two dimensions

Conformal transformations are those transformations which leave the angles between two vectors unchanged. Formally, these are the transformations that change a metric $g_{\mu\nu}$ only by a local scale factor,

$$g'_{\mu\nu}(\vec{r}') = \Omega(\vec{r})g_{\mu\nu}(\vec{r}). \quad (6.25)$$

In dimensions $d > 2$, it can be shown that these transformations are rotations $\vec{r}' = R\vec{r}$, translations $\vec{r}' = \vec{r} + \vec{a}$, dilatations $\vec{r}' = b\vec{r}$ and special conformal transformations, which amount to an inversion, a translation and another inversion. The group formed by the conformal transformations in $d > 2$ is therefore finite-dimensional. In two dimensions, on the other hand, the conformal transformations are precisely those transformations $\vec{r}' = \vec{r} + \vec{\epsilon}$ for which

$$\partial_1\epsilon_1 = \partial_2\epsilon_2 \quad \partial_1\epsilon_2 = -\partial_2\epsilon_1. \quad (6.26)$$

Introducing complex coordinates,

$$z = r_1 + ir_2 \quad \bar{z} = r_1 - ir_2, \quad (6.27)$$

one recognizes (6.26) as the familiar Cauchy-Riemann equations, whose solutions are the analytic functions in \mathbb{C} . Therefore, in two dimensions, all analytic functions $z' = w(z)$ and $\bar{z}' = \bar{w}(\bar{z})$ are conformal transformations!

These form an infinite-dimensional group with the generators

$$l_n = -z^{n+1}\partial_z \quad (6.28a)$$

$$\bar{l}_n = -\bar{z}^{n+1}\partial_{\bar{z}} \quad (6.28b)$$

for $n \in \mathbb{Z}$. The commutation relations for these generators are given by

$$[l_n, l_m] = (n - m)l_{m+n} \quad (6.29a)$$

$$[\bar{l}_n, \bar{l}_m] = (n - m)\bar{l}_{n+m} \quad (6.29b)$$

$$[l_n, \bar{l}_m] = 0. \quad (6.29c)$$

A few of these generate easily recognizable transformations:

- ▷ $l_{-1} = -\partial_z$ generates translations.
- ▷ While l_0 alone is not simply to understand, linear combinations can be formed that generate translations and rotations in the complex plane. Reparametrizing the complex plane by $z = re^{i\phi}$, we have $l_0 = -\frac{1}{2}r\partial_r + \frac{i}{2}\partial_\phi$, and \bar{l}_0 analogous. Therefore, $l_0 + \bar{l}_0 = -r\partial_r$ generates dilatations, and $i(l_0 - \bar{l}_0) = -\partial_\phi$ generates rotations in the complex plane. These will become important at a later point.

Conformal field theories are characterized by a set of operators which have well-defined transformation behavior under the conformal transformations introduced above. We can categorize the operators $A(z, \bar{z})$ of the conformal field theory into three groups: primary, quasi-primary and secondary operators, where primary operators are a subset of quasi-primary operators. In the following, we will be concerned with primary and quasi-primary operators, which have a simple transformation law under a conformal transformation $z \rightarrow w(z)$, $\bar{z} \rightarrow \bar{w}(\bar{z})$:

$$A(z, \bar{z}) \rightarrow \left(\frac{\partial w}{\partial z}\right)^\Delta \left(\frac{\partial \bar{w}}{\partial \bar{z}}\right)^{\bar{\Delta}} A(w(z), \bar{w}(\bar{z})). \quad (6.30)$$

Primary operators are those which obey this transformation law under all conformal transformations, whereas quasi-primary operators are those which obey it only for transformations generated by l_{-1} , l_0 and l_1 (projective conformal transformation). The numbers Δ , $\bar{\Delta}$ are referred to as conformal weights of the operators, and $x = \Delta + \bar{\Delta}$ is the scaling dimension of the operator.

This transformation law is sufficient to severely constrain the form of correlation functions for quasi-primary operators. For example, the two-point functions are given by

$$\langle \phi(z_1, \bar{z}_1) \phi(z_2, \bar{z}_2) \rangle = C \left(\frac{1}{z_1 - z_2}\right)^{2\Delta} \left(\frac{1}{\bar{z}_1 - \bar{z}_2}\right)^{2\bar{\Delta}}. \quad (6.31)$$

At this point, the relation to the heuristic picture of critical systems becomes clear. A critical system is characterized by a divergent correlation length, i.e. there are operators whose correlations obey a power-law decay instead of the exponential decay expected for systems away from criticality. These are precisely the quasi-primary operators of the CFT, and the conformal weights describe the decay of these correlation functions. Furthermore, a relationship can be established between critical exponents of a theory and the conformal weights, but we will not explore this further in this thesis.

It turns out that the algebra (6.28) has to be extended in order to fully describe the symmetry of a quantum system governed by a conformal field theory. This extension depends on a number c , referred to as central charge; it will play a central role in the following discussion. Unfortunately, discussing the origin of this term

would go beyond the scope of this thesis. Instead, we now state the main result, the so-called Virasoro algebra, and then discuss its implications:

$$[L_n, L_m] = (n - m)L_{n+m} + \frac{1}{12}cn(n^2 - 1)\delta_{n+m,0} \quad (6.32a)$$

$$[\bar{L}_n, \bar{L}_m] = (n - m)\bar{L}_{n+m} + \frac{1}{12}cn(n^2 - 1)\delta_{n+m,0} \quad (6.32b)$$

$$[\bar{L}_n, L_m] = 0. \quad (6.32c)$$

The importance of this algebra lies in the fact that its elements are symmetries of the fixed-point Hamiltonian of the critical system and all eigenstates of the conformal field theory are eigenstates of the elements of the Virasoro algebra. Its representation theory therefore gives a classification of all states of the theory.

We will now move on to discuss three main results: i) the classification of an important set of CFTs, the minimal models, ii) how the representation theory of the Virasoro algebra affects the spectra of critical one-dimensional quantum systems, iii) how the entanglement entropies of critical one-dimensional quantum systems can be derived from CFT.

6.2.2 Minimal models

As we saw above, the correlation functions of a conformal field theory are described by the conformal weights of its quasi-primary operators. In the next sections, we will see that these conformal weights, together with the central charge, permit the calculation of many other physical quantities as well. The knowledge of the set of conformal weights and the central charge is therefore sufficient to extract a lot of information about the behavior of the physical system.

A central result is that under certain conditions, there is only a discrete set of allowed CFTs, whose central charge and conformal weights can be calculated from very simple equations. These CFTs are referred to as minimal models due to their relation to a set of statistical models at their critical point. This is an extremely powerful result, since it i) helps to identify the CFT underlying some critical microscopic system, as there is only a restricted number of possibilities, ii) helps to characterize the physical behavior of a system as soon as it is known which of the minimal models applies.

For a system without supersymmetry, the unitary CFTs with $c < 1$ form such a discrete set [165]. It can be enumerated by an integer $m \geq 2$; the central charge

and the conformal weights are given by

$$c = 1 - \frac{6}{m(m+1)} \quad (6.33a)$$

$$\Delta = \frac{[r(m+1) - sm]^2 - 1}{4m(m+1)} \quad (6.33b)$$

where r, s are integers with $1 \leq r \leq m-1$ and $1 \leq s \leq m$. For example, the critical transverse-field Ising model is described by the $m = 3$ minimal model, with conformal weights $\Delta = 0, 1/16, 1/2$ (not listing degeneracies). As one would expect, these are the exponents of certain spin correlation functions [166].

For supersymmetric conformal field theories, the Virasoro algebra is extended to include additional terms. There are two possible extensions, namely the Ramond algebra and the Neveu-Schwarz algebra; these will reappear later as different sectors of the theory. The minimal series in the case of $\mathcal{N} = 2$ supersymmetry is ([167]) again enumerated by an integer $k \geq 1$ and has

$$c = 3 - \frac{6}{k+2} \quad (6.34a)$$

$$\Delta = \frac{p(p+2) - r(r-2) - 4r\alpha + 2k(\frac{1}{2} - \alpha)^2}{4(k+2)} \quad (6.34b)$$

for $0 \leq p \leq k$ and $r = -p, -p+2, \dots, p$, and $\alpha = 0$ ($\alpha = 1/2$) for the Ramond (Neveu-Schwarz) sector. The first model in this series has $c = 1$ and conformal weights $\Delta = 0, 1/6$ in the Neveu-Schwarz sector; we will revisit this model later in this chapter.

6.2.3 Relation to finite systems

While it is intuitively clear that a critical system is related to a conformal field theory – after taking a continuum limit in an appropriate way, and in the thermodynamic limit – our considerations so far have not lead to an obvious way of relating the CFT description and a numerical calculation, which is generally performed for a microscopic Hamiltonian on the lattice, and usually in finite systems. The only applicable relation would be the constraint on correlation functions (6.31), which however in practice is not useful on small lattices, and if the microscopic representations of the quasi-primary operators are not known.

One way to establish a tight relation is by means of a numerical renormalization procedure like the MERA, which we will discuss in the next section. There are however also useful relations between the CFT description and properties of the microscopic system even on small lattices. In the next section, we will describe a surprising relation between the spectra of microscopic Hamiltonians and the

conformal weights of the quasi-primary operators. After this, we will turn our attention to a relation between the entanglement entropy on finite lattices and the central charge of the CFT. Together, these approaches provide the most powerful numerical tools for the identification of CFTs.

Consider the following mapping of a coordinate z in the complex plane to a coordinate w on a cylinder of infinite length,

$$z = e^x e^{iy} \rightarrow w = x + iy, \quad (6.35)$$

where $x \in \mathbb{R}$ and $y \in [0, 2\pi)$ with periodic boundary conditions, $y \equiv y + 2\pi$. It will be useful to think of x as *time* and y as *space* direction. Dilatations and rotations in the complex plane are translated into time and space translations:

$$z' = e^a z \rightarrow x' = x + a \quad (6.36)$$

$$z' = e^{ib} z \rightarrow y' = y + b. \quad (6.37)$$

As shown above, $L_0 + \bar{L}_0$ generates dilatations in the complex plane, and $i(L_0 - \bar{L}_0)$ generates rotations. This means that on the cylinder, these operators generate time and space translations. This suggests a direction connection to physical operators:

$$L_0 + \bar{L}_0 \sim H \quad (6.38)$$

$$i(L_0 - \bar{L}_0) \sim P. \quad (6.39)$$

These operators are defined on an infinitely long cylinder of finite circumference. Our identification of time and space direction already suggests the relation to a 1+1 dimensional quantum system with finite extent (and periodic boundary conditions) in space dimension, but infinite extent in the (imaginary) time direction, which is precisely the ground state of a finite one-dimensional lattice system.

Indeed, the fixed point Hamiltonian of the critical system is $H = \frac{2\pi}{L}(L_0 + \bar{L}_0)$. For the original microscopic Hamiltonian, subleading corrections are present, but nevertheless the leading part of the spectrum can be constructed from the eigenvalues of L_0 . To this end, we now state some of the main results of the representation theory in the Virasoro algebra. From a vacuum state, which is defined by $L_n|0\rangle = 0$, $n \geq -1$, states corresponding to primary operators ϕ can be created. These are eigenstates of L_n , $n > 0$:

$$L_n \phi = 0 \quad (n \geq 1) \quad (6.40)$$

$$L_0 \phi = \Delta \phi, \quad (6.41)$$

where Δ is a conformal weight. Together with the algebra (6.32), this yields the important result that for a state $\phi^{n_k, \dots, n_1} = L_{-n_k} \dots L_{-n_1} \phi$, $n_i > 0$,

$$L_0 \phi^{n_k, \dots, n_1} = (\Delta + n_1 + \dots + n_k) \phi^{n_k, \dots, n_1}. \quad (6.42)$$

The energies on a finite system are therefore, up to subleading corrections,

$$E_n = \frac{2\pi v}{L} (\Delta + \bar{\Delta} + n) \quad (6.43)$$

for non-negative integers n , and some proportionality constant v which we will not discuss here.

In most situations, subleading corrections appear at order $1/L^{1+1}$, but other situations are possible, for example the three-state Potts model, with corrections at $1/L^{1+0.8}$ [168], or the Heisenberg chain, where logarithmic terms appear [169]. Such terms may render an analysis based on finite-size spectra quite difficult and it becomes important to know the precise behavior in order to extrapolate to the infinite-size limit. Deducing the behavior from numerical data is very challenging. A simple approach, like performing a numerical fit to the form $E = a/L + b/L^c$, with fit parameters a, b, c , is usually not stable. A very useful, but rarely used procedure is the van den Broeck-Schwarz extrapolation scheme [170, 171]. It was used to extract the unusual exponent in [168]. We will show examples of its application below.

6.2.4 Conformal field theory and entropy

Another very well-known result from conformal field theory is the relation between the entanglement entropy in a one-dimensional system and the central charge of a related conformal field theory. If we denote the entanglement entropy between a block of l contiguous sites in an infinite system and the rest of the system as $S(l)$, we have for the entropy of this block [33]

$$S(l) \sim \frac{c}{3} \log l. \quad (6.44)$$

This relation has proven to be extremely useful in two ways:

- ▷ It has helped to identify the appropriate CFT description of many one-dimensional microscopic Hamiltonians. To obtain the central charge, one calculates the entanglement entropy for half of a finite chain of length L , which will approximately be

$$S_L \sim \frac{nc}{6} \log L, \quad (6.45)$$

where $n = 1$ for open and $n = 2$ for periodic boundary conditions. For reasonably large systems, which can be simulated with the DMRG method, such a fit often gives accurate results for the central charge.

- ▷ It has been useful in understanding where tensor network state methods can be used successfully, as their cost is related to the scaling of the entanglement entropy with system size.

In this chapter, we will make use of this relation in the first sense, namely to numerically identify the conformal field theories describing two supersymmetric lattice models.

Equation (6.45) only holds approximately. Many subleading corrections are known and will be discussed now. A precise relation for finite systems is given in Ref. [34], which also includes several generalizations. For our purpose, the relevant result is the scaling of entanglement entropy for a block of l sites at the end of a finite system of length L , which is

$$S(l) = \frac{c}{3} \log \left(\frac{L}{\pi} \sin \frac{\pi l}{L} \right) + S_0 \quad (6.46)$$

for periodic systems, and

$$S(l) = \frac{c}{6} \log \left(\frac{2L}{\pi} \sin \frac{\pi l}{L} \right) + S_0 \quad (6.47)$$

for open systems. In the constants S_0 , we have summed up several universal and non-universal contributions, which are not relevant for the purpose of this thesis and will not be discussed further.

Two possible ways of obtaining the central charge from the entropies are possible:

- ▷ For a given system size, one can perform a fit of sub-system entropies to Eqns. (6.46) and (6.47). Usually, this should be performed for several system sizes, as additional sub-leading corrections may affect the central charge for smaller systems.
- ▷ Alternatively, if results for a large number of system sizes are available, the entropy at the center of the chain can be fit to Eqn. (6.45). In some cases, this will suffer less from sub-leading corrections and may therefore be more accurate; this is particularly true if calculations are performed only for open systems, where oscillatory corrections are often present.

Both of these approaches can be advantageous in certain situations, and we will indeed find examples for both in the following sections.

An important correction to (6.47) was first observed numerically in Ref. [172] and later explained analytically in Refs. [173, 174]. The authors of [172] consider the XY chain, which maps exactly onto free fermions and is described by a CFT with central charge $c = 1$. When introducing open boundary conditions, they find an oscillating term in both the bond energies and the entropies. The magnitude of the correction to the entropies is well fit by

$$S^c(l) \sim \left(\frac{L}{\pi} \sin \frac{\pi l}{L} \right)^{-K}, \quad (6.48)$$

so that the entropy becomes $S^{\text{XY}}(l) = S(l) + \alpha(-1)^l S^c(L)$ with the $S(l)$ of (6.47), and some fit parameter α . K is the Luttinger parameter, which in this case takes the value $K = 1$.

A heuristic explanation for the existence of such an oscillatory part is the tendency of the antiferromagnetic spin chains to form local dimers, i.e. for two adjacent sites to form a (maximally entangled) singlet, which by entanglement monogamy implies that they are less entangled to their other neighbors. When using open boundary conditions, a finite amount of such dimerization leading to alternating terms in the bond energies and entropies will occur for any system size.

6.2.5 Relation to the MERA

The scale-invariant MERA is an explicit representation of a numerical renormalization group transformation, which, for the scale-invariant MERA, reaches a fixed point. In this section, we will discuss how to relate the fixed-point RG transformation to the central charge and scaling dimensions of the conformal field theory that describes this fixed point. This relation was first demonstrated in Refs. [95, 96].

From the descending superoperator, the fixed-point reduced density matrix ρ^{fp} is obtained, and the corresponding entropy $S(\rho^{\text{fp}}) = -\sum \lambda_\alpha \log_2 \lambda_\alpha$ is calculated, where the λ_α are eigenvalues of ρ^{fp} . Due to the structure of the fixed-point reduced density matrix, which is an object of rank 4, it is possible to take the trace over half of the system to obtain $\rho_{1/2}^{\text{fp}}$, and the corresponding entropy $S(\rho_{1/2}^{\text{fp}})$. The central charge is then obtain using (6.45) as

$$c = 3 \left(S(\rho^{\text{fp}}) - S(\rho_{1/2}^{\text{fp}}) \right). \quad (6.49)$$

Since the ansatz is constructed directly in the thermodynamic limit, none of the corrections to the entropy on finite systems that were discussed in the previous section are relevant in this situation.

Obtaining the scaling dimensions is based on the transformation properties of quasi-primary operators (6.30). For a global rescaling of coordinates, $w(z) = bz$ and $\bar{w}(\bar{z}) = b\bar{z}$, they should transform as

$$A(z, \bar{z}) \rightarrow b^{\Delta+\bar{\Delta}} A(w(z), \bar{w}(\bar{z})). \quad (6.50)$$

To relate this to the scale-invariant MERA, two key insights are necessary:

- ▷ The superoperators of the scale-invariant MERA are a coarse-graining transformation which rescales distance by a factor b ($b = 3$ for the ternary MERA). This connection can be made more explicit by considering the transformation properties of two-point correlators as calculated from the ternary MERA.

- ▷ The eigenvectors of the ascending superoperator are operators that, under the RG transformation, are mapped back to themselves, i.e. obey a transformation law of the form (6.50). The eigenvalues are precisely the prefactor $b^{\Delta+\bar{\Delta}}$.

We therefore must diagonalize (using some iterative, non-Hermitian diagonalization procedure such as the Arnoldi algorithm) the ascending superoperator and obtain its eigenvalues λ_α ; the scaling dimensions are then given by

$$(\Delta + \bar{\Delta})_\alpha = -\log_3 \lambda_\alpha, \quad (6.51)$$

In the limit of an exact representation of the state by the MERA, one could expect to find all quasi-primary descendants; in practice, not all correlation functions of the system can be represented with a finite number of parameters and only the primary fields and a few descendants are found. The eigenvectors of the ascending superoperator are microscopic representations of the quasi-primary fields of the CFT; however, as the scale-invariant ansatz is usually applied not directly to the Hamiltonian, but on top of a few translationally invariant layers of the MERA, they cannot easily be related to operators on the original Hilbert space on lattice \mathcal{L}_0 . It is also possible to extract the coefficient (C in Eqn. (6.31)) for two-point correlation functions, but we will not explore this possibility in the following.

An intriguing feature of the MERA is that these results can be obtained from an ansatz for the ground state of the infinite system directly, as opposed to performing fits to finite-size data. The results should therefore not be affected by finite-size corrections and be much more useable as "black box" to extract information about the critical theory.

6.3 Chain

We now turn to a discussion of the model described in Section 6.1.2 on two specific lattices, the chain and the ladder. Placing the model on the chain, the following Hamiltonian is obtained:

$$H = \sum_i (1 - n_{i-1})(c_i^\dagger c_{i+1} + c_{i+1}^\dagger c_i)(1 - n_{i+2}) + \sum_i n_i n_{i+2} + \sum_i (1 - 2n_i) \quad (6.52)$$

The potential term takes the form of a next-nearest neighbor repulsion and a chemical potential.

The spectrum of the supersymmetric model on the chain as well as its continuum limit is well understood [153, 154, 158]. It is described by the first $\mathcal{N} = 2$

supersymmetric minimal model, with

$$c = 1 \tag{6.53}$$

$$\Delta(\text{Neveu-Schwarz}) = 0, \frac{1}{6}, \frac{1}{6} \tag{6.54}$$

$$\Delta(\text{Ramond}) = \frac{1}{24}, \frac{1}{24}, \frac{3}{8}. \tag{6.55}$$

Finite chains with periodic boundary conditions correspond to the Ramond sector of the field theory, while the Neveu-Schwarz sector is obtained with anti-periodic boundary conditions, i.e. if the fermion picks up a phase π when hopping around the circle. For chains of length $L = 3j + p$, $p \in \{-1, 0, 1\}$, the ground state has $N = j$ fermions. With periodic boundary conditions, it is two-fold degenerate for chains of length $L = 3j$ and unique otherwise. With open boundary conditions, only the Ramond sector of the theory is realized and the zero-energy ground state is unique for all lengths except $L = 3j + 1$, where no zero-energy ground state exists.

In Figure 6.2, we show the finite-size spectrum of the supersymmetric chain for several chain lengths, and extrapolated to the thermodynamic limit. The Hamiltonian was diagonalized using a Jacobi-Davidson method, which is able to extract the degeneracies of the levels. The spectrum for each system size is separately rescaled to match the lowest non-vanishing level of the conformal tower $E' = 2h - c/12$. For the Neveu-Schwarz sector, the ground state is scaled to $E' = -1/12$; in the Ramond sector, the first excited state is scaled to $E' = 6/8 - 1/12 = 2/3$. The extrapolation to $L = \infty$ was performed using van den Broeck-Schwartz approximants. The extrapolated spectrum nicely matches the expectation from conformal field theory.

In the following, we will first discuss results for the entropy of the open and periodic chain. Similar results have been shown previously, e.g. in [158]. As most important new result, we will obtain a heuristic expression for the oscillatory part of the entropy for open chains. Furthermore, we will discuss results obtained with the MERA directly for the infinite system.

6.3.1 Entropy

To obtain the entropies for large system sizes, we have simulated the model on chains with periodic and open boundary conditions using the DMRG method. As the standard DMRG method is formulated for a Hilbert space with tensor-product structure, the hard-core constraint cannot easily be implemented on the level of

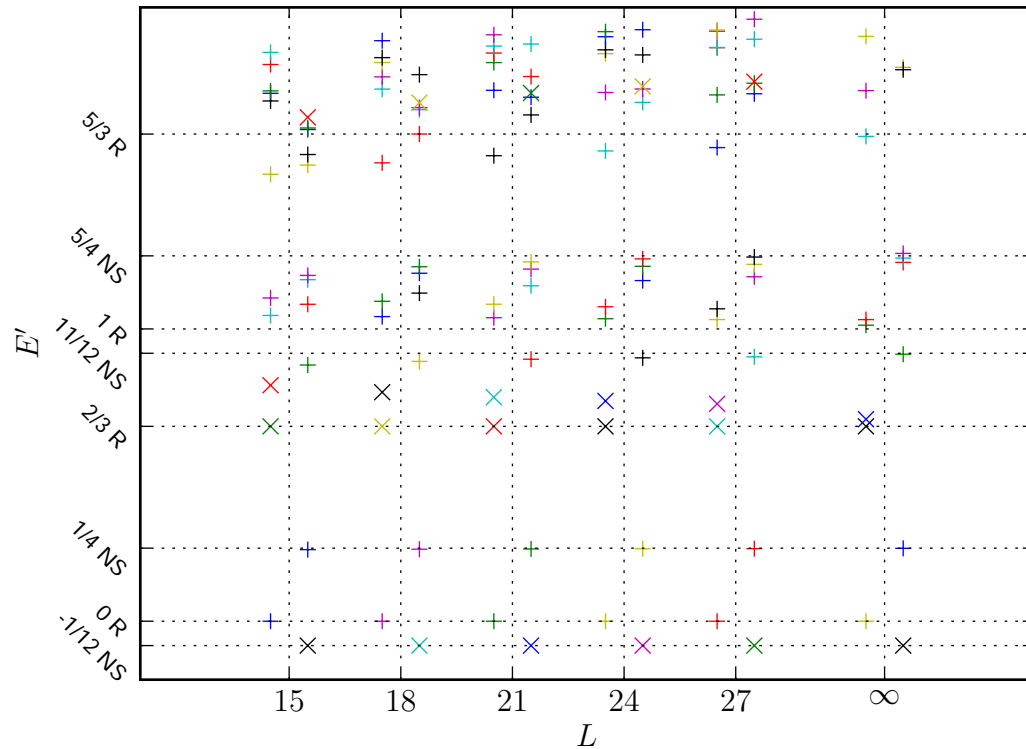


Figure 6.2: Rescaled energies for finite chains of the supersymmetric lattice model. The energy have been rescaled such that the lowest non-vanishing energy matches the expected levels. Points on the left are obtained with periodic, those on the right with anti-periodic boundary conditions. + indicates a doubly degenerate level, x a non-degenerate level. Extrapolations are performed with van den Broeck-Schwartz approximants as discussed in the text. The labels on the energy axis indicate whether the state occurs in the Neveu-Schwartz sector, corresponding to anti-periodic boundary conditions, or the Ramond sector, which corresponds to periodic boundary conditions.

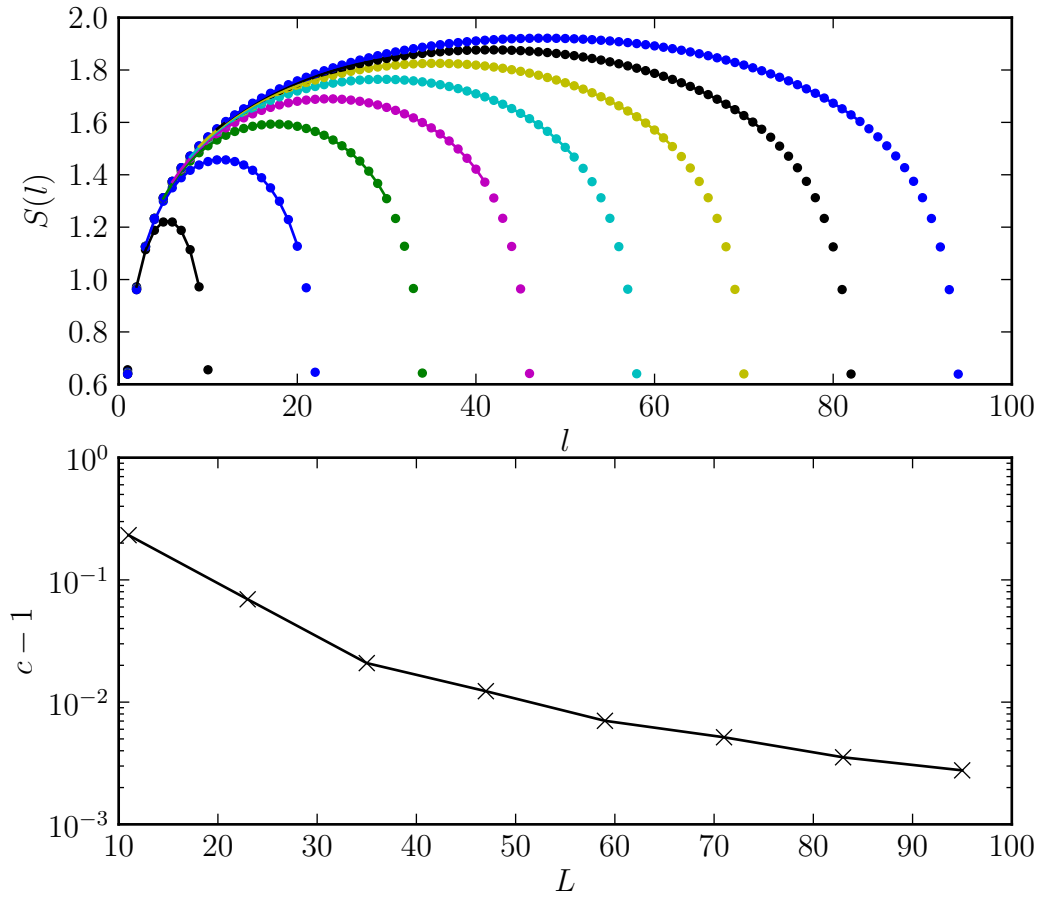


Figure 6.3: Subsystem entropies for periodic chains with $L = 3j - 1$, $N = j$, and j up to 32 ($L \leq 95$). In the top panel, crosses indicate the numerical data, while the lines indicate fits according to (6.46), where at most $1/8$ of the sites at the ends of the chain were discarded.

the state. We therefore add a penalty term to the Hamiltonian, given by

$$H_p = p \sum_i n_i n_{i+1} \quad (6.56)$$

with $p > 0$. Numerically we find that a small value $p \sim 1 \dots 5$ is sufficient to suppress violations of the hard-core constraint. A Jordan-Wigner transformation (cf. Eqn. (2.29)) is used to map the system to a spin system; the only term with a non-trivial sign is the hopping around the boundary in the periodic case.

For the case of periodic boundary conditions, we also use standard DMRG methods, i.e. we treat the system as an open system with a long-range interaction term connecting the leftmost and rightmost sites. We run the simulations at fixed truncation error, but limit the bond dimension to $M = 1000$. In many simulations, in particular for open chains, this limit is not reached in the simulation, indicating that our results should be very accurate. We can confirm convergence of the results by checking that the ground state energy is close to $E = 0$; generally, a deviation smaller than 10^{-8} is obtained, which can be attributed to the numerical accuracy of the eigensolver we use. We have also calculated the densities on each site (one-point function) and compared against known results [158].

For periodic boundary conditions, the entropies are very accurately described by the simple expression (6.46). Results for chains of length $L = 3j - 1$ and $N = j$ for j up to 32 are shown in Fig. 6.3. For the fit, we have discarded at most 1/8 of the points at the ends of the chain to remove effects due to corrections for very small block sizes. For small systems, subleading corrections lead to significant corrections of estimate for the central charge, but for the larger system sizes, very accurate fits are obtained.

For open boundary conditions, strong oscillating corrections to the entropy appear, which make simple fits such as (6.47) impossible. In our case, the oscillations display a three-sublattice structure, which is symmetric around the center for one sublattice, but asymmetric for the other two. This resembles the structure of the density [157, 158]. A reasonable fit is obtained by combining three correction terms similar to the one used in [172]:

$$f_1(l) = S_0 + \frac{1}{6} \log \left(\frac{2L}{\pi} \sin \frac{\pi x}{L} \right) \quad (6.57a)$$

$$f_2(l) = \alpha_1 \left(\frac{L}{\pi} \sin \frac{\pi x}{L} \right)^{-1/3} \quad (6.57b)$$

$$f_3(l) = \alpha_2 \left(\frac{L}{\pi} \sin \frac{\pi x}{2L} \right)^{-1/3} . \quad (6.57c)$$

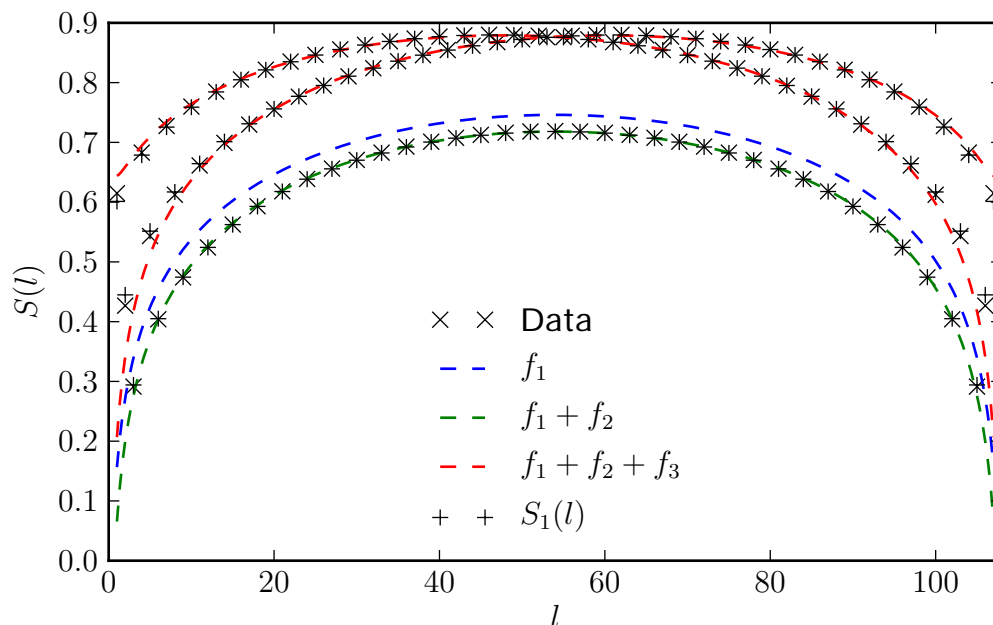


Figure 6.4: Subsystem entropies for all three sublattices of an open chain of length $L = 108$ (crosses). The lines illustrate the terms of Eqn. (6.57), where the red lines are $f_1(l) + f_2(l) + f_3(l)$ and $f_1(l) + f_2(l) + f_3(L - l)$, i.e. reflected around the center of the chain. Plus signs indicate a fit to (6.59).

The first term coincides with (6.46) for $c = 1$. The subsystem entropies for the three sublattices are then well described by:

$$l \bmod 3 = 0 : S(l) = f_1(l) + f_2(l) \quad (6.58a)$$

$$l \bmod 3 = 1 : S(l) = f_1(l) + f_2(l) + f_3(l) \quad (6.58b)$$

$$l \bmod 3 = 2 : S(l) = f_1(l) + f_2(l) + f_3(L - l). \quad (6.58c)$$

Fixing the central charge at $c = 1$ leaves three fit parameters, S_0 , α_1 and α_2 . An example is shown in Fig. 6.4.

In [174], such corrections were analyzed in a more general way and we can

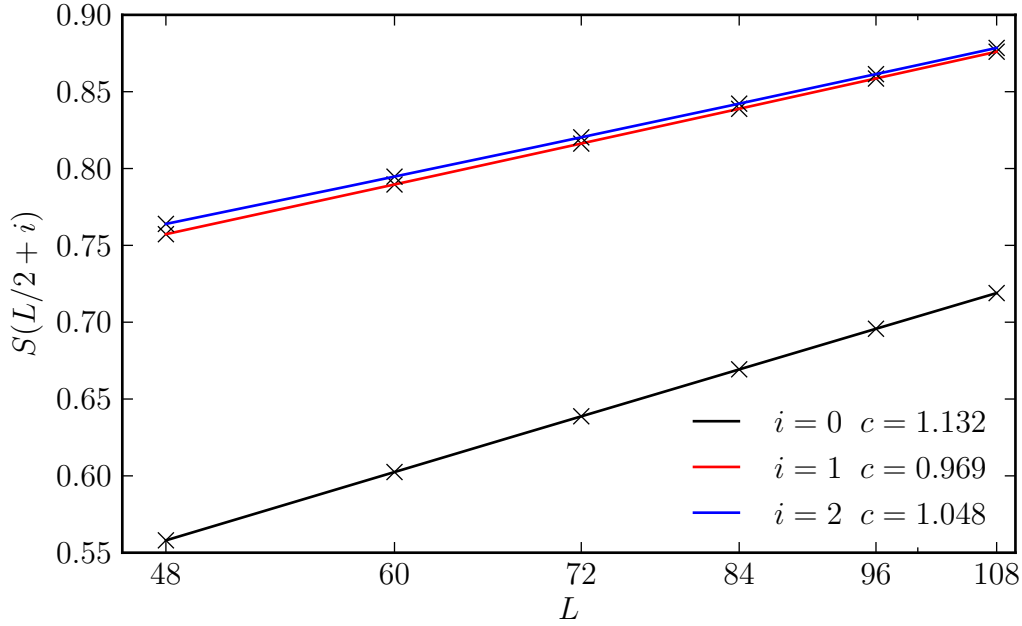


Figure 6.5: Fits of the entropy for bonds close to the center of the chain to (6.45). $i = 0$ corresponds to the center of the chain.

adapt Eqn. (70) from that paper for our situation to find:

$$S_1(l) = \frac{1}{6} \left[\frac{4(L+3)}{\pi} \sin \left(\frac{\pi(2l+3)}{2(L+3)} \right) |\sin k'_F| \right] + c'_1 \quad (6.59a)$$

$$- 4a_1 \sin(k'_F(2l+2)) \left[\frac{4(L+3)}{\pi} \sin \left(\frac{\pi(2l+3)}{2(L+3)} \right) |\sin k'_F| \right]^{-1/3} \quad (6.59b)$$

$$k'_F = k_F \frac{L}{L+2} + \frac{\pi}{2(L+2)} \quad (6.59c)$$

$$k_F = \pi/3 \quad (6.59d)$$

Free parameters in this case are a_1 and c'_1 . An example is also shown in Fig. 6.4. While this expression makes the three-sublattice structure less apparent, it achieves even better agreement with the numerically obtained data.

We have also performed the fit according to the second scheme described in Section 6.2.4, i.e. fitting the entropies for sites on the three sublattices close to the center of the chain according to the form (6.45). Noticing that for fixed l/L , the oscillating terms of both (6.57) and (6.59) take a much simpler form, we can take

these into account by performing a fit to

$$S(L/2) = S_0 + \frac{c}{6} \log L + \alpha L^{-1/3}, \quad (6.60)$$

where α is an additional fit parameter related to the fit parameters in (6.58). Our results are shown in Fig. 6.5. The fact that the accuracy for $i = 0$ is worse is related to the behavior of the coefficients α_1, α_2 in (6.58): we find that α_2 is much larger than α_1 and has less finite-size corrections. Therefore, (6.60) works better in cases where the correction due to α_2 is present.

6.3.2 MERA

The Hamiltonian on the chain (6.52) has a four-point term consisting of a hopping from i to $i + 1$ and the corresponding projection operators on sites $i - 1$ and $i + 2$. Incorporating this directly into the MERA is computationally not favorable, as it will lead to a broader light cone and therefore increase the computational cost. We therefore join several sites of the physical chain to a block, which will serve as effective physical site in the MERA simulation. This has several advantages:

- ▷ For a block size larger than 3, all operators become nearest-neighbor operators.
- ▷ Similar to DMRG, the MERA is based on a Hilbert space with tensor-product structure. We therefore again have to use the penalty term (6.56) to enforce the hard-core constraint. The constraint can be enforced explicitly within the block by keeping only those states which form valid configurations, which improves convergence significantly.
- ▷ Since the lowest level of the MERA structure we use groups three sites into one, the bond dimension for the lowest level is limited to $2^3 = 8$ without blocking. By blocking L sites, we can increase this to 2^{3L} , which may lead to better convergence.

Since the fermions are spinless and the construction of our MERA is in the thermodynamic limit immediately, a fermionic exchange sign does not have to be taken into account and the system can be treated like a spin system.

For our simulations, we use the ternary MERA structure (cf. Fig. 2.21). We use a \mathbb{Z}_2 subgroup of the particle number conservation to speed up simulations. In the following results, we will denote the bond dimension of the MERA we use as χ ; by this, we will refer to the total bond dimension. We keep the size of the symmetry sectors equal for all bonds except the physical ones. On finite systems, the model on the chain displays a three-sublattice translational structure.

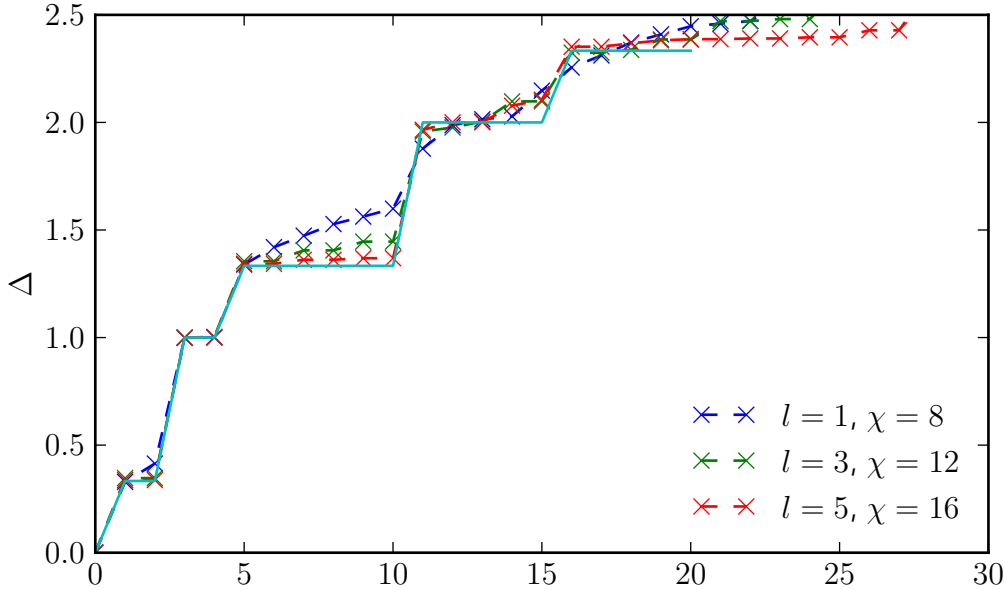


Figure 6.6: Scaling dimensions obtained from a MERA with l layers and total bond dimension χ exploiting \mathbb{Z}_2 symmetry. The line indicates the first few of the exactly known scaling dimensions and degeneracies.

Parameters	Central charge c
$l = 1, \chi = 8$	0.996
$l = 3, \chi = 12$	1.018
$l = 5, \chi = 16$	1.016

Figure 6.7: Central charge obtained from a MERA simulation of the supersymmetric model on the chain. Parameters correspond to those of Fig. 6.6.

However, since we group three physical sites into one site of the MERA, we expect to find a translationally invariant state after convergence.

Starting from a random initial state, we increase both the number of independent layers l below the scale-invariant MERA and the bond dimension step by step, taking the last state as initial state which is expanded by inserting random isometric transformations. The central charge is accurate already for a small bond dimension. The scaling dimensions, however, become much more accurate as we take more layers and a higher bond dimension into account, as shown in Fig. 6.6.

For supersymmetric CFTs, it can be expected that only one sector of the theory is realized by the MERA. As a variational method, it should realize the

lowest-energy state of the theory; in the case of the first minimal model, this is the vacuum occurring in the Neveu-Schwarz sector. Indeed we find that the MERA reproduces accurately the scaling dimensions expected in the Neveu-Schwarz sector of the CFT.

6.4 Square ladder

After studying the well-understood case of the supersymmetric model on the chain, we move on to a quasi-one-dimensional lattice, the square ladder. It is believed to be critical as well, and an attempt to determine its critical theory was made in [156, 152]. It was conjectured to be described by the second minimal $\mathcal{N} = 2$ superconformal field theory, which has central charge $c = 1.5$ and scaling dimensions

$$\Delta(\text{Neveu-Schwarz}) = 0, \frac{1}{8}, \frac{1}{8}, \frac{1}{4}, \frac{1}{4}, \frac{1}{2} \quad (6.61)$$

$$\Delta(\text{Ramond}) = \frac{1}{16}, \frac{1}{16}, \frac{1}{16}, \frac{5}{16}, \frac{9}{16}, \frac{9}{16}. \quad (6.62)$$

However, no consistent interpretation of the data in terms of a CFT was obtained. We therefore revisit this model and attempt to extract information about the critical theory based on the same numerical tools that we have successfully applied to the case of the chain.

We first compare this against the central charge extracted from entanglement entropy data obtained with DMRG. We then perform exact diagonalization for larger systems to check whether the discrepancy between numerics and the minimal model is due to finite-size corrections. We also check whether the densities (one-point function) for open ladders agrees with theoretical expectations. Finally, we discuss results obtained using the MERA.

The ground state on the square ladder occurs at quarter filling, i.e. at fermion number $N = L/2$. The number of ground states can be calculated also for the case of the square ladder. It is expected that for periodic boundary conditions, the zero-energy ground state is three-fold degenerate for even lengths, and unique otherwise. With anti-periodic boundary conditions, the ground state is unique and has $E < 0$, which approaches 0 as L is increased.

To confirm that the system is indeed critical, we check whether the energies of excited states with one and two fermions added or removed vanish; this is equivalent to confirming that the charge gap vanishes. We calculate the energies of the ground state in different particle number sectors using DMRG for system sizes between $L = 20$ and $L = 100$ and extrapolate to $L \rightarrow \infty$ using a polynomial in $1/L$. Our results confirm quite accurately that such charge excitations are

gapless. A similar analysis can be performed for a few excited states in a particle number sector obtained by exact diagonalization; while the system sizes we can study are much smaller in this case, an extrapolation still strongly suggests that the energies vanish as $1/L$.

6.4.1 Entropy

We attempt to confirm the value of $c = 1.5$ for the central charge by calculating subsystem entropies with DMRG and performing the same analysis that we have done for the chain. To improve convergence for large systems, it turns out to be necessary to join several physical sites into a block and enforce the hard-core constraint exactly by keeping only allowed configurations. While usually the Jordan-Wigner transformation for a ladder should introduce additional signs, the hard-core constraint makes all signs trivial except for terms hopping around the boundary.

The unknown central charge and the large finite-size corrections make it difficult to conjecture an expression analogous to (6.58) for the ladder. We therefore resort to the other two approaches, namely (anti-)periodic systems that do not display oscillatory behavior, and fitting the entropy at the center of the system as a function of the total system size.

We first discuss the results obtained for anti-periodic boundary conditions shown in Fig. 6.8. We have simulated systems of length up to $L = 86$ using up to $M = 2400$ states. As the system becomes highly entangled, $M = 2400$ is not sufficient to reach convergence in the number of states for the largest system sizes, but can serve as a very good estimate. Finite-size corrections are clearly much more relevant than in the case of the chain. As opposed to open systems or blocks embedded in an infinite system, there is currently no theoretical understanding of such corrections to the entropy for periodic systems. We therefore cannot extract with certainty a value for the central charge from this data. While they naively seem to indicate a central charge $c \sim 1.6$, this result would be highly unexpected; a more plausible explanation are additional terms in the entropy whose origin is not understood.

For open systems, we repeat our analysis of the entropy of block size $l = L/2$ and $l = L/2 + 1$ as we did for the chain. Since we have no expression for the oscillating part, we attempt to take them into account by performing a fit to

$$S(L/2) = S_0 + \frac{c}{6} \log L + \alpha L^b. \quad (6.63)$$

Note that we have introduced an additional fit parameter, b . For open systems, we can access quite large system sizes and therefore reliably extract the exponent.

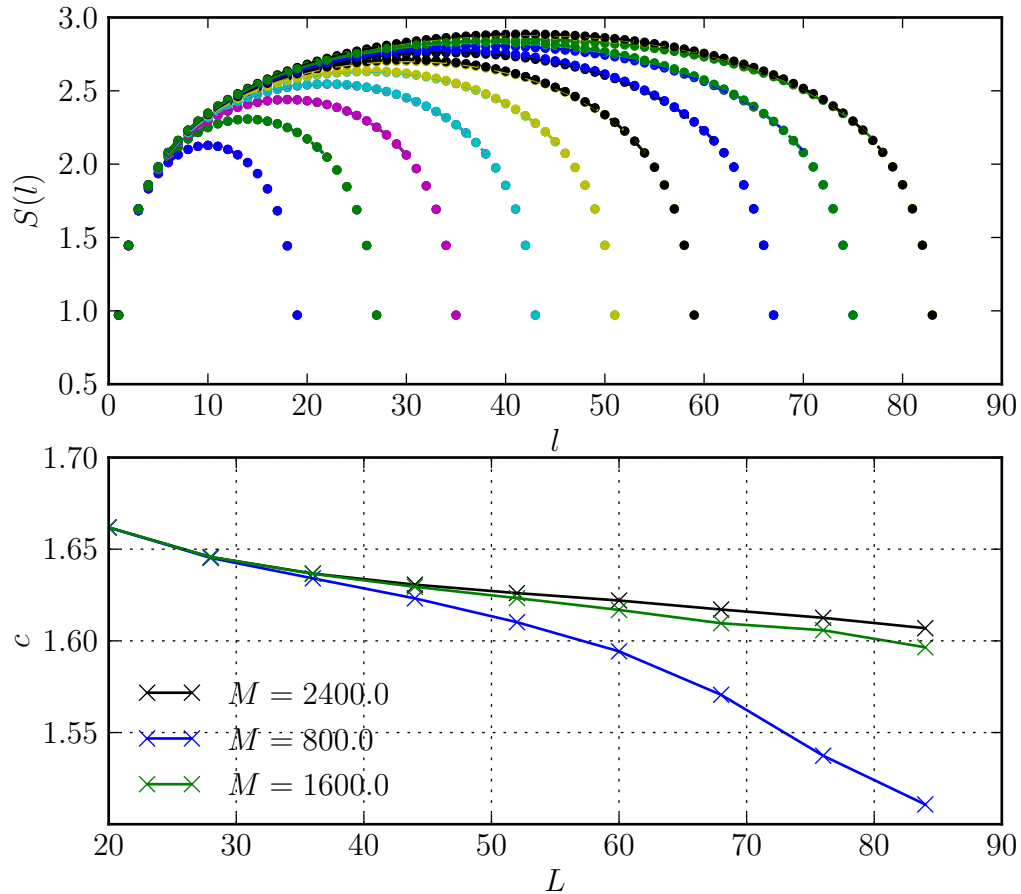


Figure 6.8: Entropy fits for the square ladder with antiperiodic boundary conditions.

Results are shown in Fig. 6.9, where we also show a fit to the simple form $S(L/2) = S_0 + \frac{1.5}{6} \log L$. Again results indicate a central charge larger than $c = 1.5$, as none of the lines collapse to a straight line with slope 1.5 even for large system sizes; instead, even for the more accurate case $i = 1$, the slope appears to increase for larger system sizes.

6.4.2 Finite-size spectra

To illustrate the problem observed with the square ladder, consider Fig. 6.10, which shows the spectrum of the square ladder for lengths $L = 8, \dots, 24$. The Hilbert

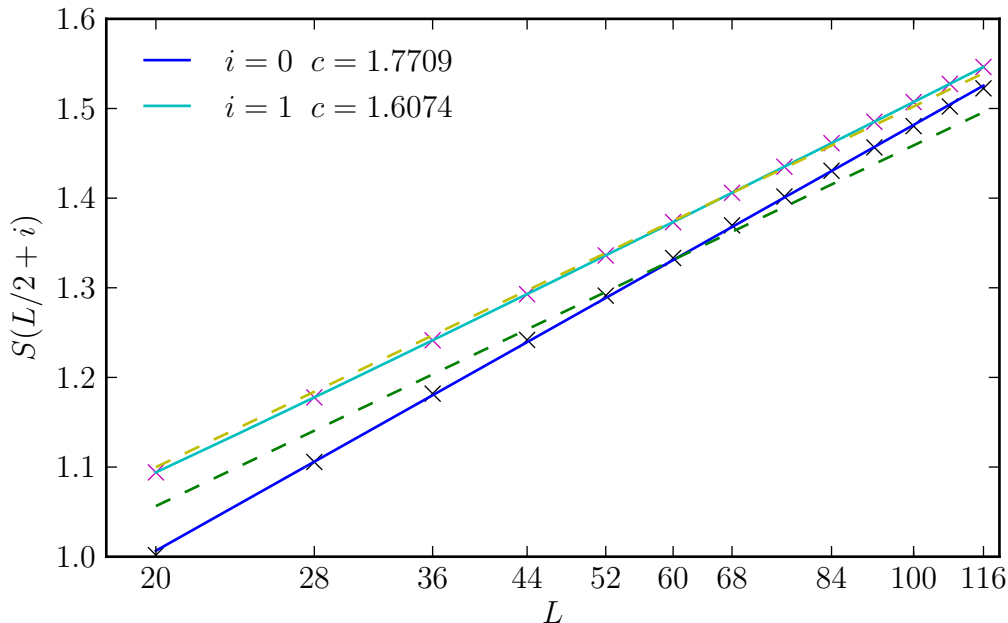


Figure 6.9: Entropy fits for open ladders. Crosses indicate numerical data; solid lines indicate a fit to (6.63); dashed lines indicate a fit to $S_0 + \frac{1.5}{6} \log L$. The data do not collapse onto a straight line with slope 1.5/6 even for the largest system sizes.

space of the largest system contains roughly 300 million states, which was diagonalized using the Lanczos algorithm; for the smaller systems, the Jacobi-Davidson algorithm was used which requires more memory but permits the determination of degeneracies. Both algorithms are implemented in the ALPS library [8]. The spectra were rescaled so that the lowest non-vanishing energy matches the expected value for the second $\mathcal{N} = 2$ supersymmetric minimal theory and levels were approximated using van den Broeck-Schwartz approximants, which we have shown to be reliable in the case of the chain.

Consider first the Ramond sector, corresponding to periodic boundary conditions: The first important observation is that a state at $E' = 1$ is missing, and none of the higher states appear to come down in energy to yield $E' = 1$ after extrapolation. For the next levels, $E' = 3/2$ and $E' = 2$, the finite-size extrapolation of some excited levels appears to match, albeit with a rather steep extrapolation. Between these levels, we find a large number of additional states for which we have no consistent interpretation.

In the Neveu-Schwarz sector, a similar picture is found. The level $E' = 3/8$ is missing completely, and agreement for $E' = 7/8$ and $E' = 9/8$ is not good; only

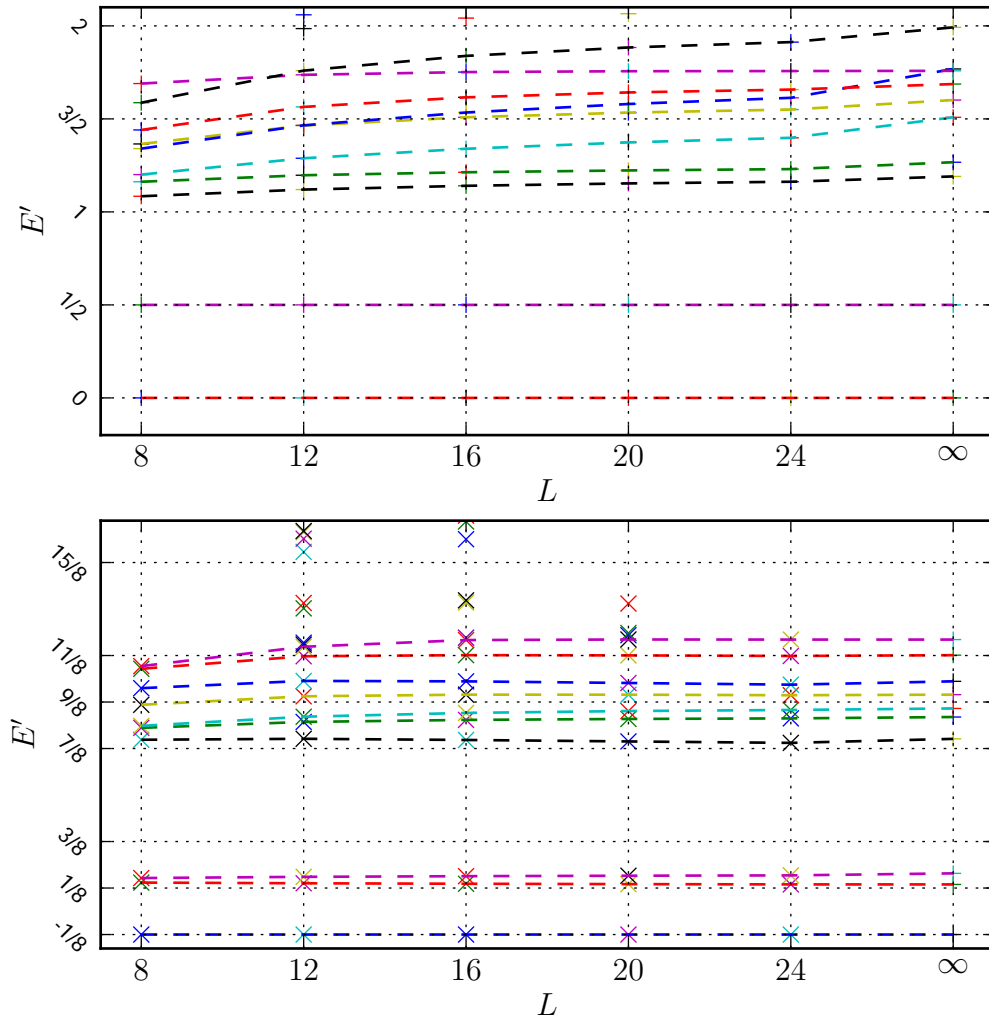


Figure 6.10: Rescaled spectra for the square ladder. Results in the Ramond sector (periodic BCs) are shown in the top panel, Neveu-Schwarz sector (antiperiodic BCs) in the bottom panel. Lines are guide to the eye. We have introduced some "level crossings" between $L = 8$ and $L = 12$ to improve the extrapolation.

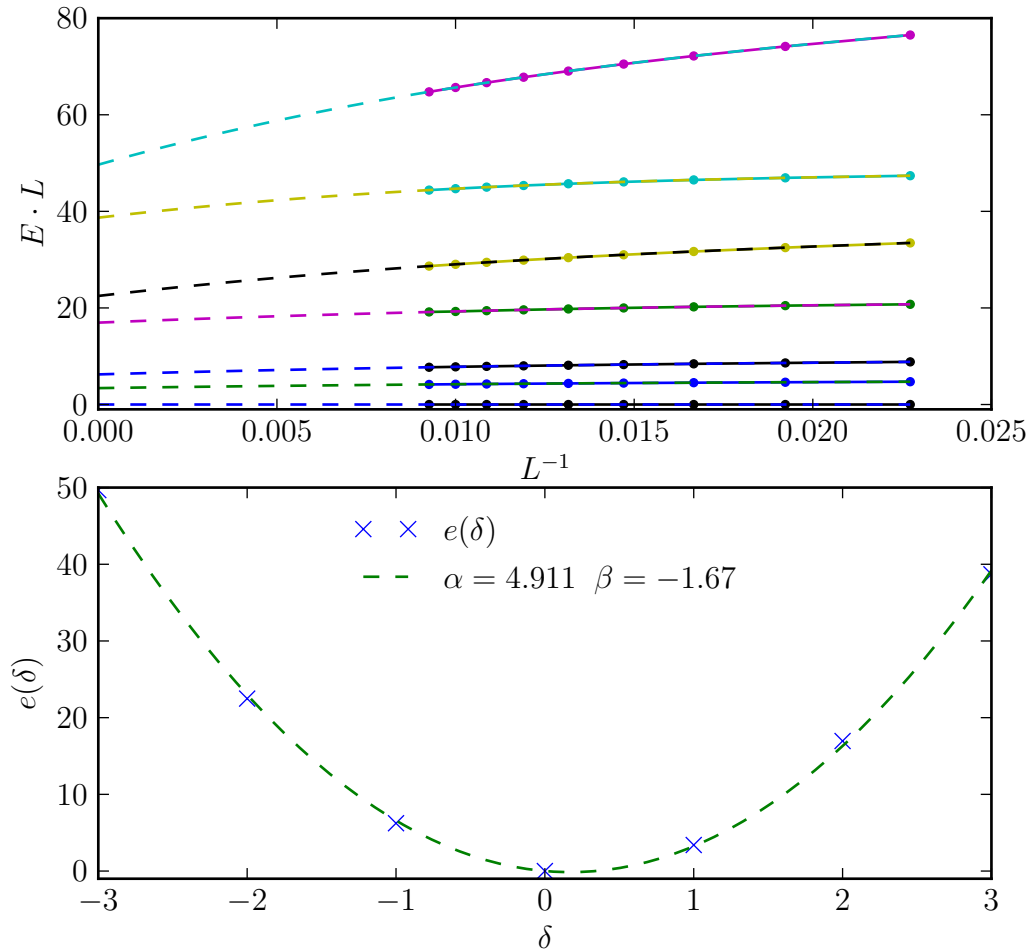


Figure 6.11: Extrapolation of the ground state energy in different particle number sectors.

$E' = 11/8$ is matched well after extrapolation. Again, a large number of states are found which cannot be attributed to any level of the CFT.

A different approach is to study the ground state energy when doped away from the ground state at quarter filling. Since the ground state energy for different quantum number sectors can be reliably calculated with DMRG for much larger system, this approach may suffer less from finite-size corrections. Field theoretical

arguments indicate that the ground state energy should behave like

$$E = aE_{\text{CFT}}/L + \text{subleading terms} \quad (6.64)$$

$$E_{\text{CFT}} = \delta^2 + 2m_0\delta, \quad (6.65)$$

where $\delta = N - L/2$ is the doping away from quarter filling, and m_0 some constant. For the infinite-size limit of $E(\delta) \cdot L$, which we will denote as $e(\delta)$, we expect to find

$$e(\delta) = \alpha\delta^2 + \beta\delta. \quad (6.66)$$

Performing this analysis for finite systems reveals that the energies are not symmetric around $\delta = 0$: while a good fit can be obtained for $\delta < 0$ and $\delta > 0$ separately, a single fit does not seem to describe the behavior [152]. To understand whether this behavior is due to finite-size corrections or persists in the thermodynamic limit, we perform DMRG simulations for the ground state energy with various particle numbers for system sizes of up to $L = 120$. In order to reach convergence, we must again group several sites into a block and enforce the constraint on the Hilbert space exactly.

With the energies we obtain, we perform a fit to the form

$$E(\delta) \cdot L = e(\delta) + b(\delta)/L + c(\delta)/L^2 + d(\delta)/L^3 \quad (6.67)$$

for each value of δ . We find that with all terms included, a symmetric behavior of $e(\delta)$ is obtained to good accuracy; our results are shown in Fig. 6.11. Such a collapse is not observed if any of the terms are omitted, which indicates that finite-size corrections, even to higher orders, are very relevant in this problem. We also point out that this finite-size scaling ansatz is not justified by rigorous arguments, but instead merely a conjecture; as we discussed earlier, many other subleading correction terms are conceivable and may lead to better results.

6.4.3 Density

The one-point function or local density for open chains was first calculated using number-theoretical methods by Beccaria et al in [157]. The density oscillates exhibiting a characteristic three-sublattice structure with an amplitude that decays away from the ends of the chain. The authors performed finite-size scaling of the data and found good agreement with

$$\langle n_i \rangle - 1/3 = f_+((i - k_+)/\tilde{L})\tilde{L}^{-\nu} \quad i \bmod 3 = 2 \quad (6.68a)$$

$$\langle n_i \rangle - 2/3 = f_-((i - k_-)/\tilde{L})\tilde{L}^{-\nu'} \quad i \bmod 3 = 1 \quad (6.68b)$$

where $\tilde{L} = L/3 + 1$ and $k_{\pm} = (L \pm 1)/2$. The best data collapse is observed for $\nu = \nu' = 0.33(2)$, which suggests a relation to the scaling dimension $\Delta + \bar{\Delta} = 1/6 + 1/6 = 1/3$ which is found in the first supersymmetric minimal model.

This relation was made more precise in [158], where the density was related to the one-point function of an operator in the conformal field theory, whose expectation value for open chains could be calculated and was found to agree with the results of Beccaria et al.

A similar behavior is found in the more general setting of Luttinger liquids. In Ref. [175], density oscillations of open systems are discussed for charge-density wave (CDW) states and Luttinger liquids. For CDW states, translational symmetry is broken in the thermodynamic limit. Open boundary conditions, which break translational invariance also on finite systems, will then induce an oscillation with an amplitude that decays slowly to a finite value in the center of the system. In Luttinger liquids, translational symmetry is not broken in the infinite system, but boundaries also cause oscillations. Their decay is found to be related to the Luttinger liquid parameter K , which is the exponent of the slowest-decaying correlation function and hence directly related to the conformal weights. For finite systems, the authors of [175] obtain the expression

$$n_i \sim \frac{1}{L^K} \frac{\cos(2\pi ni + \beta)}{\sin(\pi i/L)^K}, \quad (6.69)$$

where n determines the wavelength of oscillations. This is clearly reminiscent of the expression obtained in [158] for the case of the supersymmetric chain. Also, this expression suggests a scaling ansatz of the form (6.68) with $K = \nu$.

We now apply these methods to results for the square ladder, which we have obtained numerically using DMRG simulations of open ladders of lengths between $L = 20$ and $L = 100$. The densities on the both chains are equal, and we observe a \mathbb{Z}_2 structure of the density on the rungs, i.e. different densities on even and odd rungs. For the finite-size scaling, we therefore modify the ansatz Eqn. (6.68) and use

$$\langle n_i \rangle - \langle n_k \rangle = f_{\pm}((i - k)/L)L^{-\nu} \quad (6.70)$$

where i enumerates rungs, $k = L/2$ and f_{\pm} applies to odd and even rungs, respectively. $\langle n_k \rangle$ approaches $1/4$ in the thermodynamic limit. Eqn. (6.69) and the analogy to the chain also suggest an expression for the FSS ansatz functions f_{\pm} . We expect good agreement with

$$f_{\pm} = \pm C \frac{\sin(\pi x')}{\cos(\pi x')^K}, \quad (6.71)$$

where we have defined $x' = (i - k)/L$ and C is a fit parameter. The role of sin and cos is interchanged with respect to (6.69) due to a shift of $\pi/2$ in the parameters. Based on (6.69), we expect that the exponent K equals ν and ν' and that it is found to be one of the scaling dimensions of the CFT.

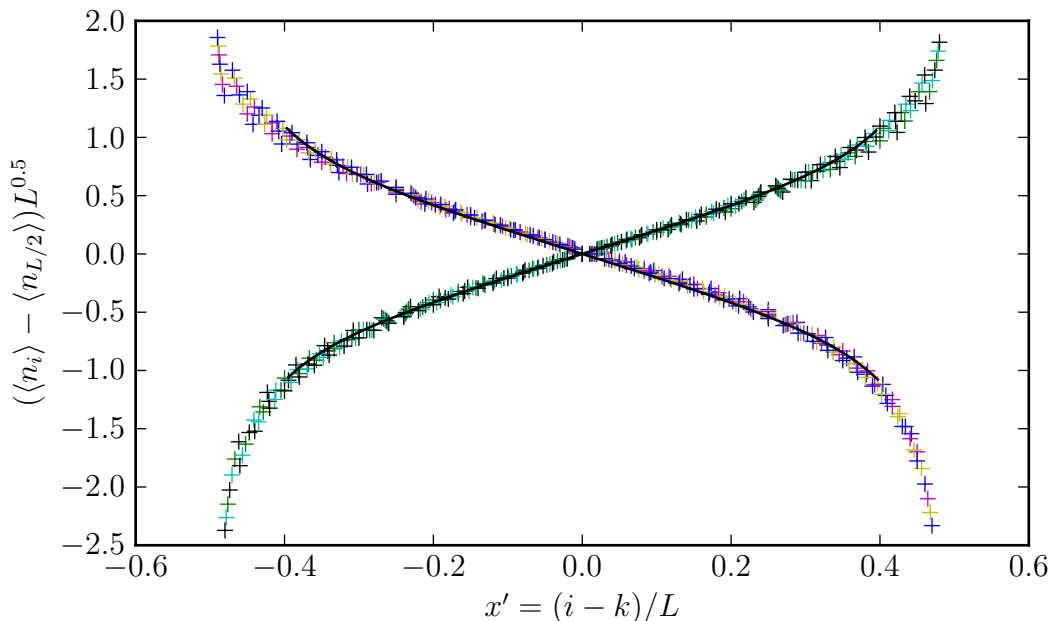


Figure 6.12: Finite-size scaling of the density for open square ladders (crosses) and fit to (6.71) (solid black lines). i indicates the rung. Different colors indicate data for different system sizes, where we have excluded system sizes $L < 50$. The fit is restricted to $-0.4 < x' < 0.4$.

Our results for the finite-size scaling are shown in Fig. 6.12. For $\nu = \nu' = K$, we observe both good data collapse away from the boundaries of the system and good agreement with (6.71). This suggests the presence of a quasi-primary operator with scaling dimension $\Delta + \bar{\Delta} = 1/2$, which is indeed present in the second supersymmetric minimal model.

Instead of performing finite-size scaling and a fit of the FSS ansatz functions separately, a similar result can be obtained by fitting to finite systems directly using an appropriately adapted expression. We find good agreement also in this case, as shown in Fig. 6.13. Such an expression for finite systems can, analogous to the chain, be derived directly from the CFT [176]. We find excellent agreement with the numerical data; also, after an appropriate change of variables, it coincides with (6.70) and (6.71).

6.4.4 MERA results

We have also simulated the model on the square ladder using the MERA. We again use a ternary MERA and group several physical sites into one site for the MERA

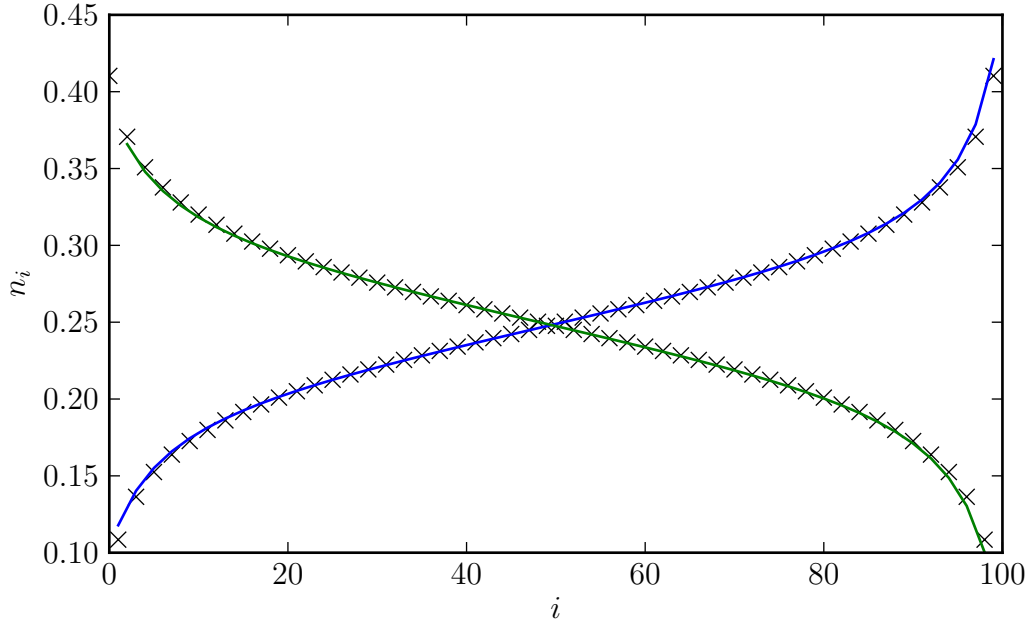


Figure 6.13: Fit of an adapted form of Eqn. (6.71) to the density profile of an open ladder of length $L = 100$. The crosses indicate numerical data; the green and blue line show the fit for the two branches $i \bmod 2 = 0, 1$.

to properly accommodate the operators, which involve up to 8 sites on 4 rungs in the case of the square ladder. The minimum number of sites we have to group in this case is 6 sites, corresponding to 3 rungs.

This leads to a subtlety when attempting to exploit particle number conservation: as the filling should be $1/4$, the reduced density matrix for such a block of 6 sites should have the most relevant contributions for states with a fractional particle number $n = 1.5$. Therefore, in this particular setup, although the Hamiltonian preserves particle number, we cannot easily use a $U(1)$ or \mathbb{Z}_2 invariant ansatz, as this would require us to use a basis with fractional particle numbers on some bonds. Indeed we find empirically that using a \mathbb{Z}_2 invariant ansatz leads to a wrong filling.

However, in the case of the square ladder, there is an additional \mathbb{Z}_2 symmetry which is not a subgroup of the $U(1)$ particle number conservation, but instead related to the \mathbb{Z}_2 symmetry between the two chains that form the ladder. Consider the operator

$$g_{\mathbb{Z}_2} = \exp(i\pi(n_u - n_l)), \quad (6.72)$$

where n_u and n_l are the particle number operators on the upper and lower chain, respectively. This operator commutes with the Hamiltonian and we can choose

a basis of its eigenstates for the three allowed states on a rung where the state with no fermions forms the irreducible representation labelled $+$ and the other two states, with one fermion on either the upper or lower site, form the irreducible representation labelled $-$, which has dimension 2. Using this basis, we can construct the \mathbb{Z}_2 symmetric version of the MERA following the description of Chapter 3.

We have performed simulations for a MERA with bond dimension up to $\chi = 20$ and two independent layers below the scale-invariant ansatz. With such an ansatz, we are able to reproduce a central charge in the vicinity of $c = 1.5$. However, we do not obtain scaling dimensions smaller than 1, which would indicate that no relevant operators are present in the theory. This seems extremely unlikely and must be taken as indication that the bond dimension is not sufficient to accurately capture correlation functions.

Chapter 7

The SU(3) Heisenberg model

7.1 The model

Recent advances in experiments on cold atomic gases have raised interest in systems consisting of several flavors of interacting fermions, which can be realized for example as different hyperfine states of alkali atoms [177] or nuclear spin states of ytterbium [178] or alkaline-earth atoms [179]. A model Hamiltonian to describe such systems is the N -flavor fermionic Hubbard model given by

$$H = -t \sum_{\langle i,j \rangle} \sum_{\alpha} c_{i\alpha}^{\dagger} c_{j\alpha} + U \sum_i \sum_{\alpha,\beta} n_{i\alpha} n_{i\beta}, \quad (7.1)$$

where α, β run over the different flavors, $\langle i, j \rangle$ runs over pairs of nearest neighbors on the lattice and i runs over all sites of the lattice.

The two-flavor case corresponds to the spin- $\frac{1}{2}$ Hubbard model (cf. Section 5.1). It is generally accepted that the ground state at half filling, i.e. when each lattice site is occupied by exactly one fermion, is an antiferromagnetic Mott insulator. The transition to a Mott insulator has recently been observed in experiments on cold atoms [180, 181]; the observation of the antiferromagnetic spin order is still open. As discussed in Section 5.1, the spin- $\frac{1}{2}$ Heisenberg model is believed to be a good low-energy model for the spin degrees of freedom.

For the more general case $N > 2$, it is expected that at certain fillings, Mott insulating states will also emerge [182, 183]. However, the spin order (or flavor order) in this case is not understood yet. This has raised interest in generalizations of the spin- $\frac{1}{2}$ Heisenberg model, namely SU(N) Heisenberg models. Analogous to the $N = 2$ case, these are obtained as second-order expansion of the above N -flavor fermionic Hubbard model in t/U at a filling such that each site is occupied

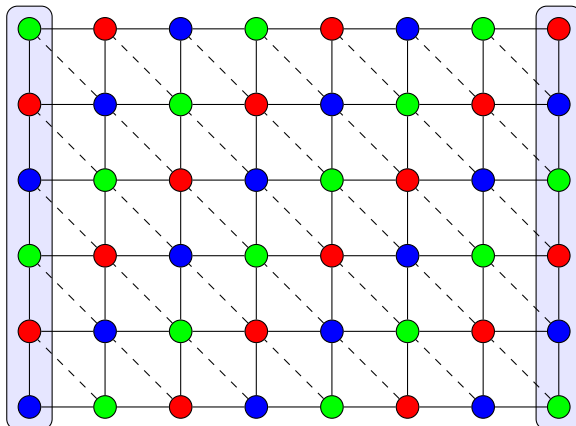


Figure 7.1: Proposed three-sublattice order for the SU(3) Heisenberg model on the square and triangular lattice. The triangular lattice is obtained from the square lattice by adding couplings along the dashed bonds shown above. Blue boxes indicate the sites that are pinned to a specific flavor in our simulations in order to explicitly break SU(3) symmetry.

by exactly one particle. The Hamiltonian is

$$H = \sum_{\langle i,j \rangle} \sum_{\alpha,\beta} |\alpha_i \beta_j\rangle \langle \beta_i \alpha_j| \quad (7.2)$$

where the first sum runs over pairs of nearest neighbors and the second sum over flavors. In this chapter, we will focus on the case of the SU(3) Heisenberg model, where $\alpha, \beta \in \{A, B, C\}$.

The same model is obtained for a particular choice of the couplings of the spin-1 bilinear-biquadratic model (cf. Eqn. (8.13)):

$$H = \sum_{\langle i,j \rangle} \left[\cos \theta (\vec{S}_i \cdot \vec{S}_j) + \sin \theta (\vec{S}_i \cdot \vec{S}_j)^2 \right], \quad (7.3)$$

For a discussion of physical realizations of this model, we refer to [184]. At $\theta = \pi/4$, the two models are equivalent up to a shift and rescaling of the energy. In the remainder of this chapter, we will use the convention of (7.2).

In a pioneering work, Papanicolao [185] studied the phase diagram of this model on the square lattice as a function of θ and proposed that the case $\theta = \pi/4$ corresponds to a phase transition from the antiferromagnetically ordered phase (adiabatically connected to the purely bilinear case) to a "semi-ordered phase" for which the semiclassical arguments presented do not predict the order, but only some constraints which can be fulfilled by several different orders.

The situation changes for the closely related case of the triangular lattice (equivalent to introducing a coupling on one of the diagonals of each plaquette of the square lattice), where semi-classical arguments already suggest a three-sublattice ordering as depicted in Fig. 7.1. The stability of this order against quantum fluctuations was confirmed in [184].

For the square lattice, this three-sublattice ordering is one of the candidate ground states obtained from semiclassical arguments, but a number of other possibilities have been explored as well [186, 187, 177, 188]. Recent results strongly indicate that the same type of three-sublattice order is stabilized by quantum fluctuations [189], however, the mechanism is very different: in the case of the triangular lattice, the order is obtained already from semi-classical arguments and quantum fluctuations only renormalize local moments, which is a situation similar to that of the $SU(2)$ Heisenberg model on bipartite lattices. In the case of the square lattice, on the other hand, it is suggested that the order is selected only by quantum fluctuations.

In this chapter, we aim to confirm the presence of a three-sublattice order by means of combining two tensor network state algorithms, namely the projected entangled-pair states on infinite lattices and finite-lattice density matrix renormalization group calculations. The iPEPS simulations referred to in this chapter were performed by Philippe Corboz.

7.2 Methods

Our DMRG simulations are performed based on mapping the two-dimensional system to a chain following the pattern shown in Fig. 2.3. We will generally refer to the extent in the horizontal direction as length, and in the vertical direction as width of the system. The Hamiltonian preserves the number of particles for each flavor separately, which would suggest three $U(1)$ symmetries, but due to the constraint that $n_A + n_B + n_C = 1$ on each site, only two $U(1)$ symmetries remain, which we exploit in our simulations. We use the single-site optimization scheme explained in Section 2.1.1 augmented by the improvement suggested in [61].

In practical calculations, it turns out that convergence is much harder to reach than for other ordered systems such as the spin- $\frac{1}{2}$ Heisenberg model. This applies in particular to the case of the square lattice, where a simple mean-field state ($M = 1$ limit) is not necessarily a good starting point for the simulation. We therefore use several different random initial states and increase the bond dimension very quickly with the number of sweeps in order to avoid trapping in local minima. Together with the large number of operators and the large amount of entanglement we observe, this restricts our simulations to relatively small system sizes. Nevertheless, we can access much larger systems than exact diagonalization

with sufficient accuracy.

Due to the technical difficulties, we do not attempt high-accuracy extrapolations of the data. Instead, we repeat simulations for a large number of bond dimensions M in the range $M = 800$ to $M = 4800$ in order to obtain an estimate of how well results are converged with respect to the bond dimension; also, we use the three best points to perform a linear extrapolation, but this data must be taken with caution.

We expect that in the thermodynamic limit, the $SU(3)$ symmetry is spontaneously broken. If an appropriate basis is chosen (i.e. after an appropriate $SU(3)$ rotation), one flavor becomes stronger on each site, i.e.

$$n_\alpha > n_\beta = n_\gamma \quad \alpha, \beta, \gamma \in \{A, B, C\}. \quad (7.4)$$

In this case, we can define the local moment

$$\langle m \rangle = \frac{3}{2} \left(\max_{\alpha=A,B,C} \langle n_\alpha \rangle - \frac{1}{3} \right), \quad (7.5)$$

which should acquire a finite value in the range $\langle m \rangle \in [0, 1]$.

As the PEPS simulations are carried out on an infinite lattice, spontaneous symmetry breaking can occur and therefore the moment can be measured directly. On finite systems, the symmetry is never broken spontaneously and one would conventionally use the relation

$$\langle n_\alpha \rangle^2 = \lim_{d \rightarrow \infty} (\langle n_{\alpha,i} n_{\alpha,i+3d} \rangle - \langle n_{\alpha,i} \rangle \langle n_{\alpha,i+3d} \rangle) \quad (7.6)$$

to extract information about the moments. This however requires large systems and very accurate estimates for the correlation functions, which are hard to obtain from a DMRG simulation in two dimensions. We therefore follow the prescription of Refs. [137, 55] and break $SU(3)$ symmetry explicitly by introducing fields at the boundaries of the system. The local moments can then be measured locally, preferably on sites far away from the pinning fields. The pinning fields also fix the direction of the symmetry breaking to be along the basis vectors.

We introduce a column of pinned sites at each end of the system, as shown in Fig. 7.1. We choose the system sizes such that the unpinned sites form a square, i.e. the system size including pinned sites is $(L + 2) \times L$. Pinning is done with a flavor-specific chemical potential of magnitude 1. In addition, such pinning fields reduce the entanglement in the system. Simulations were performed for both open and cylindrical boundary conditions.

An important question when performing finite-size DMRG simulations is the appropriate choice of boundary conditions. From an entanglement point of view, open boundary conditions appear favorable; also, these will have fewer long-range

operators in the mapping to a chain. From a physical point of view, on the other hand, periodic boundary conditions are often preferred as they eliminate boundary effects. A compromise suggested e.g. in [137] is to use cylindrical boundary conditions. In the example of the mapping of Fig. 2.3, boundary conditions would be chosen open along the horizontal and periodic along the vertical direction. From an entanglement point of view, this offers the advantage that entanglement is not too strongly affected by growing the system in the horizontal direction. When growing the system in the vertical direction, on the other hand, the entanglement growth due to the area law implies an exponentially growing cost regardless of the boundary conditions.

Physically, such boundary conditions are compatible with the approach of pinning two columns, which preserves translational invariance in the vertical direction. In order not to frustrate the three-sublattice order, such boundary conditions should only be chosen for systems whose width is a multiple of three. For other system sizes, shifted cylindrical boundary conditions can be used. For example, for a system of width 5, the bottom site of column i must be connected to the top site of column $i + 1$ to obtain a system without additional frustration.

7.3 Results

7.3.1 Boundary conditions and pinning fields

Fig. 7.2 shows the bond energies of a $(6 + 2) \times 6$ system simulated with open and cylindrical boundary conditions. The magnetizations we obtain in the two cases are vastly different: in the case of open boundary conditions, a finite and relatively large moment is observed, while in the case of cylindrical boundary conditions, extrapolating in M suggests a vanishing moment.

For an explanation of this behavior, consider Fig. 7.3, which shows the energy per site for open and periodic chains as a function of the system length. For periodic boundary conditions, the limiting value is approached from below, while for open boundary conditions, it is approached from above; also, finite-size corrections are also particularly strong in the case of periodic chains. The system therefore prefers to form a state consisting of a product of chains which wrap the periodic boundary conditions in the vertical direction, which is clearly visible in the strong anisotropy of the bond energies in the lower panel of Fig. 7.2. A similar pattern emerges for other widths when shifted cylindrical boundary conditions are used.

Another subtlety occurs for systems sizes for which the pattern of our pinning fields allows two different ordered states. For these cases, at a sufficiently large

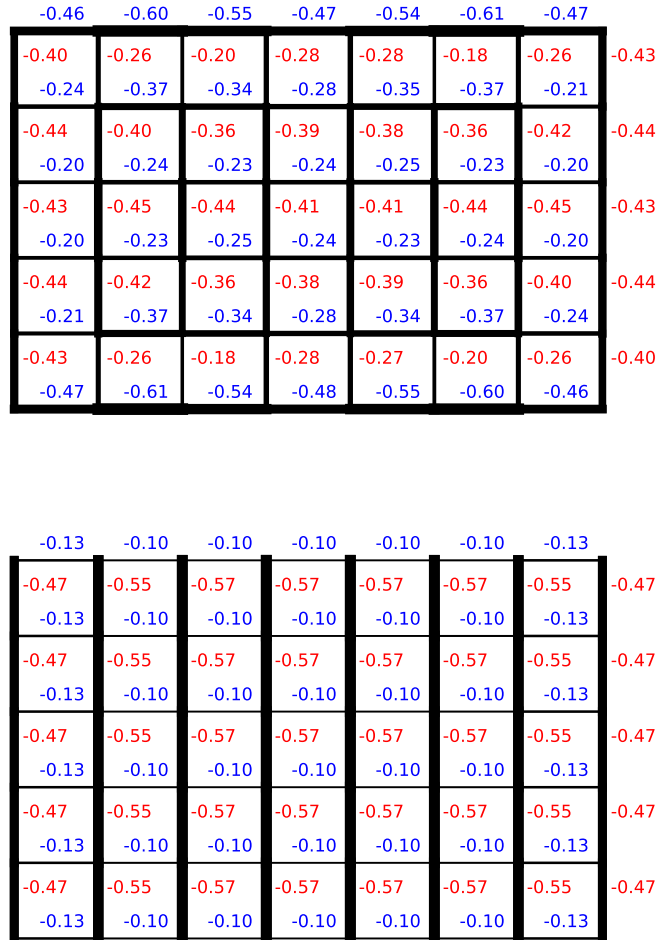


Figure 7.2: Bond energies (horizontal: blue, vertical: red) for a $(6+2) \times 6$ system where two columns at each side are pinned. Top panel: Open boundary conditions. Bottom panel: Cylindrical boundary conditions. Both simulations were performed with $M = 4800$ states. In the case of cylindrical boundary conditions, the local moments almost vanish.

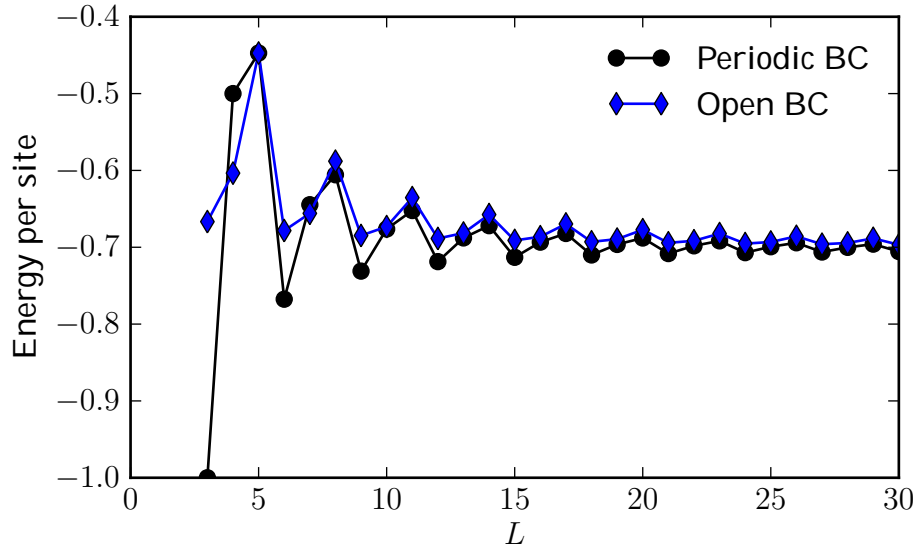


Figure 7.3: Energy per site for the $SU(3)$ Heisenberg model on chains with open and periodic boundary conditions. The key difference is that in the case of open boundaries, the energy approaches the infinite-size limit from above, while for periodic boundary conditions, it is approached from below.

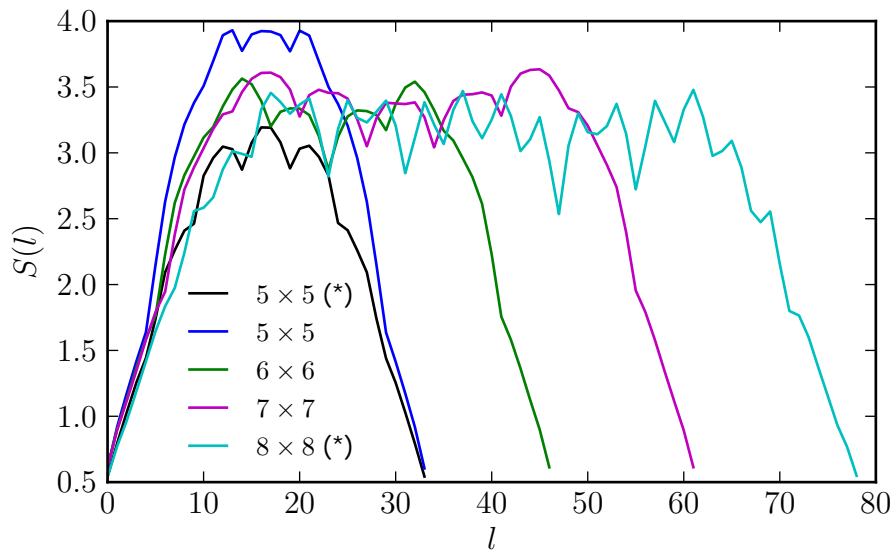


Figure 7.4: Entanglement entropy as a function of block size l along the mapping of Fig. 2.3. Stars indicate systems with additionally pinned sites to select a unique order.

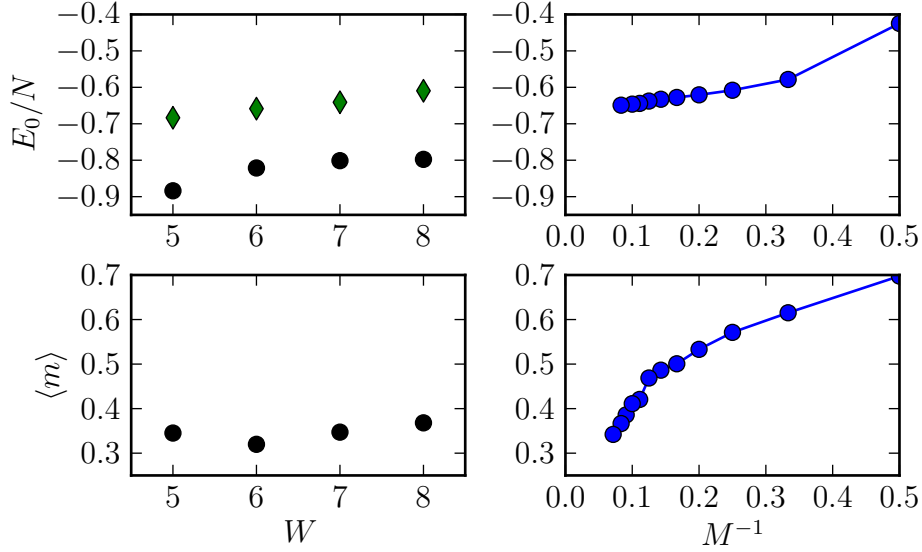


Figure 7.5: Left panels: Energy and local moment of the SU(3) Heisenberg model on the square lattice extrapolated to $M \rightarrow \infty$ for several system sizes (cf. Fig. 7.7). The energies shown as black circles are the total energies of the system, i.e. including pinning fields; green diamonds are the bulk energy estimates obtained as described in the text. Right panels: iPEPS data for various values of the bond dimension M . The energies should correspond to the bulk energy estimates of the DMRG results.

bond dimension, a superposition of both types of order will occur and lead to a significant decrease of the local moment (except on sites where the two types of order coincide) and a significant increase of the entropy. In these cases, we pin two additional sites to uniquely select the order. The effect on the entropy can be seen for the $(5 + 2) \times 5$ system in Fig. 7.4.

7.3.2 Energy and local moment

In Figs. 7.7 and 7.8, we show the finite- M values for the energy and magnetization for the square and triangular lattice on systems of size $(5 + 2) \times 5$ to $(8 + 2) \times 8$ with bond dimensions in the range from $M = 800$ to $M = 4800$. Extrapolations are performed by a linear fit to the best three points in M^{-1} . The energies shown include contributions from the pinning fields. For odd system sizes, the magnetization is measured at the central site of the system; for even system sizes, the magnetization is averaged over the four sites that make up the central plaquette

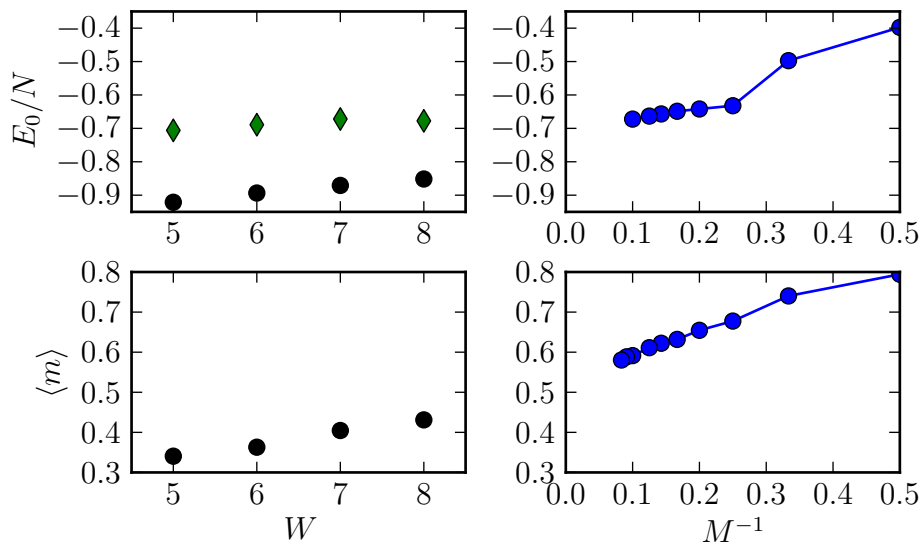


Figure 7.6: Results for the triangular lattice, analogous to those of Fig. 7.5.

of the system.

To estimate the energy per site in the bulk of the system, i.e. free of boundary and pinning effects, we calculate the (interaction) energy separately on each bond on the lattice and proceed as follows:

- ▷ In the case of the square lattice and even system sizes, we average over the four bonds surrounding the central plaquette of the system.
- ▷ In the case of the square lattice and odd system sizes, we average over four central plaquettes.
- ▷ In the case of the triangular lattice and odd system sizes, we average over the bonds adjacent to the central site.
- ▷ In the case of the triangular lattice and even system sizes, we average over four sites at the center of the system.

Figures 7.5 and 7.6 show our estimates for the local moment and energies on finite systems with open boundary conditions in comparison with data obtained for infinite systems using the iPEPS method. The results shown were obtained with the simplified update scheme described in Section 2.2.2 and expectation values were extracted with a variant of the corner-transfer matrix method [93].

Comparing the estimates for the bulk energy, we find good agreement between the methods on both lattices. Finite-size corrections of the DMRG results are small for this quantity, which suggests that we can take the value for the largest system size as estimate for the thermodynamic limit. In the case of iPEPS, ground

state energies converge quickly with the bond dimension M .

While both methods confirm the presence of a three-sublattice order for the triangular and the square lattice, a quantitative comparison of the local moment is challenging. In the case of the square lattice, finite-size corrections of the local moments are very mild, but not systematic. We can therefore only take the value for the largest system, which is $\langle m \rangle \approx 0.37$, as estimate. The iPEPS data show a significant drop of the magnetization for large values of the bond dimension; however, it is not clear to what extent this may be an artefact of the update method or other technical aspects. Results for the largest bond dimensions are compatible with a magnetic moment on the order of $\langle m \rangle \approx 0.3 \dots 0.4$, which is consistent with the DMRG data.

In the case of the triangular lattice, the finite-size corrections of the DMRG data are stronger but also more systematic and seem to point at a local moment on the order of $\langle m \rangle \approx 0.5$. This is consistent with the iPEPS data, which do not show the significant decrease of the local moment that was observed in the case of the square lattice. A higher value for the local moment than in the case of the square lattice is also expected from other, semi-classical arguments.

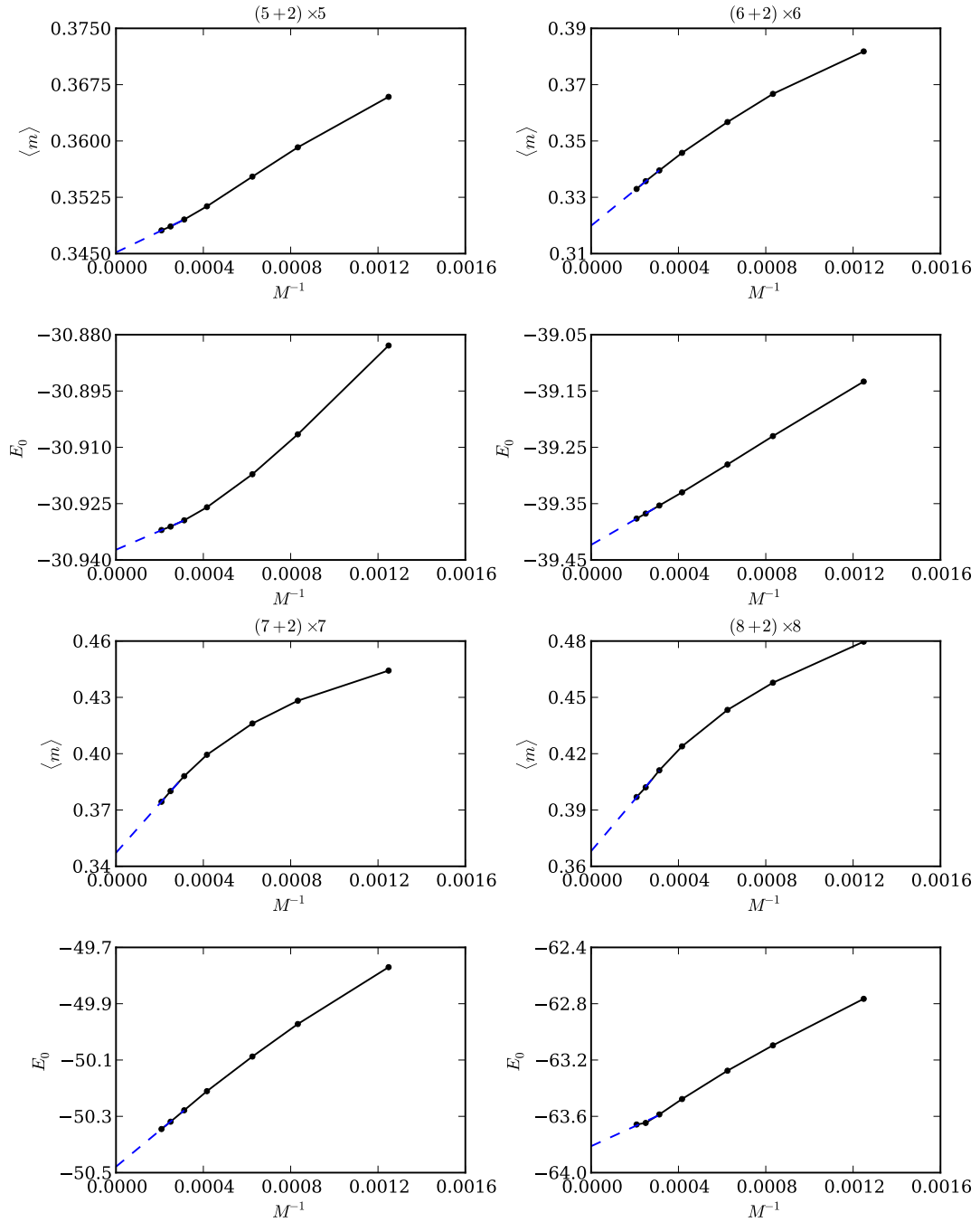


Figure 7.7: Finite- M data and extrapolation for several system sizes of the $SU(3)$ Heisenberg model on the square lattice. Extrapolation is performed by a linear fit in M^{-1} to the three largest values of M available. For $(5+2) \times 5$ and $(8+2) \times 8$, two additional sites were pinned to select a unique order.

7.3 Results

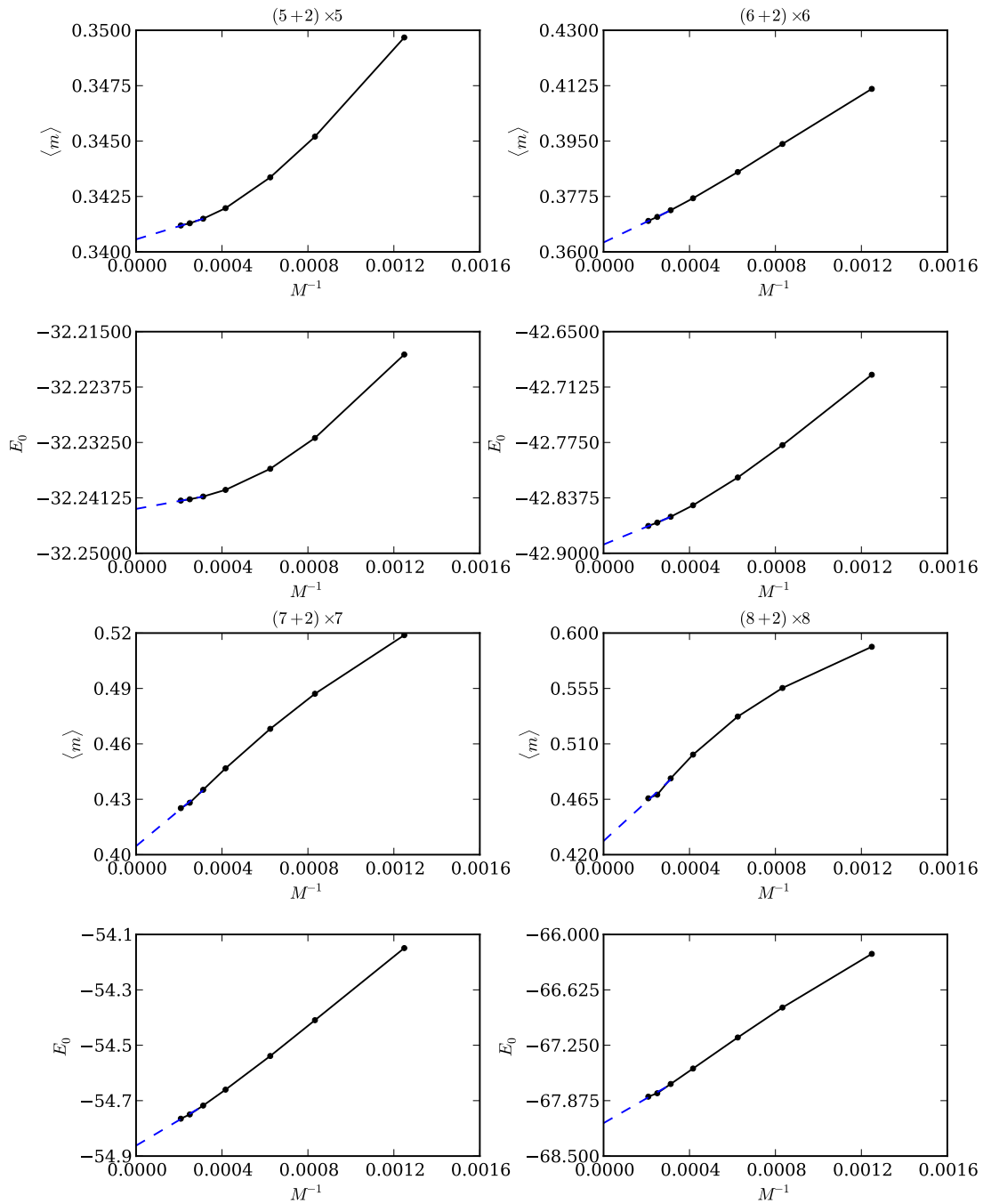


Figure 7.8: Finite- M data for the triangular lattice. No additional pinning is required in this case as the additional interaction terms select the order uniquely.

Chapter 8

Indistinguishability

In this chapter, which is based on work published in Refs. [2, 9], we will discuss an approach to identify phases and phase transitions in situations where simple order parameters are either not known, or do not exist. Such a situation commonly occurs for models exhibiting topological order [11], where local order parameters do not exist. Examples which we study are the AKLT model [190] or the Toric code [191]. Our approach will be useful in situations where the existence of a local order parameter is not excluded, but its precise form is unknown.

A related problem is confirming the relevance of some effective model to the description of a more complicated model, or, similarly, checking whether some variational ansatz is able to capture the essential physics of a more complicated state. For this purpose, it is useful to have a measure confirming that the ground state of the effective and the realistic model share the same physical properties. Defining such a measure in cases where order parameters are not known is again a difficult problem, and no general solution is known.

Currently, several approaches exist to address such problem:

- ▷ To check variational ansatz states, comparing the energy to the full solution is a useful measure of quality. However, many interesting physical systems are characterized by a competition of several ground states, which may have similar energies but vastly different physical properties. The energy alone cannot serve as measure of quality in such cases.
- ▷ A widely used approach, which is also useful for detecting phase transitions, is the fidelity (overlap). In the context of phase transitions, it was first applied in Ref. [192].
- ▷ For detecting quantum phase transitions, the entanglement entropy is a useful measure [193, 194]. Its scaling with system size changes at a phase transition, which leads to a peak if a parameter is tuned across the transition for a given system size.

In the following, we investigate a measure for assessment of ansatz wavefunctions that allows for a clear identification of a particular phase. We refer to this measure as indistinguishability I . It has origins in quantum state discrimination [195, 196, 197]. We demonstrate the use of this indistinguishability measure by application to the assessment of ansatz wavefunctions for the ground state of several different models: i) the transverse Ising chain, ii) the spin-one bilinear-biquadratic Heisenberg chain, and iii) the Toric code. The first example provides a simple test of the approach while the latter allows us to exploit its power to analyze a challenging and rich model whose solution has not yet been fully characterized.

The measure is particularly well suited for tensor network state methods that can easily obtain the reduced density matrices. For our calculations on one-dimensional systems, we use the iTEBD method described in Section 2.1.2, from which we obtain the ground state in the form of a matrix-product state.

8.1 Indistinguishability

Given two states Ψ_A and Ψ_E and corresponding reduced density matrices $\rho_A^{(n)}$, $\rho_E^{(n)}$, which have support on n sites, we define the indistinguishability $I_n(A,E)$ as the probability of error in distinguishing the two states with an n -particle measurement:

$$I_n(A, E) = \frac{1}{2} - \frac{1}{4} \text{Tr} |\rho_E^{(n)} - \rho_A^{(n)}| \quad (8.1)$$

where $\text{Tr}|\mathcal{O}|$ is the trace norm of \mathcal{O} [195, 196, 197]. The last term in Eqn. (8.1) is a well known statistical distance measure, the Kolmogorov distance between two probability distributions. When $I_n(A,E)$ is zero, the states are distinguishable and the ansatz wavefunction Ψ_A is clearly a bad approximation to Ψ_E . However, when it is non-zero, there is a finite probability that an n -particle measurement can not distinguish the ansatz from the numerical wavefunction, implying that the ansatz provides a good description of the state up to n -particle correlators. $I_n(A,E) = 1/2$ corresponds to maximum indistinguishability, implying identical states.

Since the measure is defined in terms of reduced density matrices, the state indistinguishability implicitly scans all correlators with up to n particles, to yield a single number that quantifies the ability of an optimally chosen set of n -particle correlators to distinguish two states [195, 196]. $1 - I_n$ gives the probability that an optimally chosen correlation function involving at most n particles will be able to distinguish the two states.

An important question is how n has to be chosen to reliably distinguish states. We will encounter situations where a fixed n is sufficient independent of the total system size N , but also a situation where n has to scale with N in order to reliably

distinguish the states. In cases where a small constant value of $n \sim \mathcal{O}(1)$ suffices to characterize the correlators (i.e., two states can be distinguished locally), we define I_n to be *intensive* in N . Such two states belong to the same n -particle *correlator class* if I_n remains finite in the thermodynamic limit (i.e., as $N \rightarrow \infty$). On the other hand, if two states can not be distinguished locally and therefore n needs to scale with N , we define I_n to be *extensive*. In this situation, we use the scaling of n with N to identify correlator classes [2]. The precise scaling behavior of n with N (e.g., $n \sim \mathcal{O}(N)$ or $n \sim \mathcal{O}(\sqrt{N})$) provides us with a key feature to reliably distinguish phases.

8.1.1 Quantum Chernoff bound

In some situations, it may be more useful to consider the scaling of the indistinguishability with the total system size instead of the value for fixed n and N . The scaling to the thermodynamic limit can be quantified in terms of the quantum Chernoff bound (QCB). Assuming that on sufficiently large scales, a translationally invariant ground state can be regarded as a tensor product of subblocks (or copies), a recent result [198] for the indistinguishability of many copies of the system shows that we should expect an exponential dependence for large n , i.e. $I_n \sim \exp(-n\xi_{\text{CB}})$, where the QCB can be identified in the thermodynamic limit from

$$\xi_{\text{CB}}^{\text{lim}} = - \lim_{n \rightarrow \infty} \log(I_n)/n \quad (8.2)$$

with $n = N/2$. A remarkable relation [198] connects the QCB directly to the reduced density matrices of *finite* blocks, namely

$$\xi_{\text{CB}}^{\text{lim}} \equiv \xi_{\text{CB}}^\rho \quad (8.3)$$

with

$$\xi_{\text{CB}}^\rho = - \log \min_{0 \leq s \leq 1} \text{Tr} \left[(\rho_A^{(n)})^s (\rho_E^{(n)})^{1-s} \right], \quad (8.4)$$

thereby allowing a direct evaluation in terms of the reduced density matrices $\rho_E^{(n)}$ and $\rho_A^{(n)}$. Using either of these expressions for the QCB we can then identify correlator classes in the thermodynamic limit: small values of ξ_{CB} correspond to large values of I_n and indicate a successful ansatz.

8.1.2 Calculating I using matrix-product states

Our simulation uses an MPS approximation to a state in the full spin Hilbert space. We choose a representation that is closely related to the canonical form

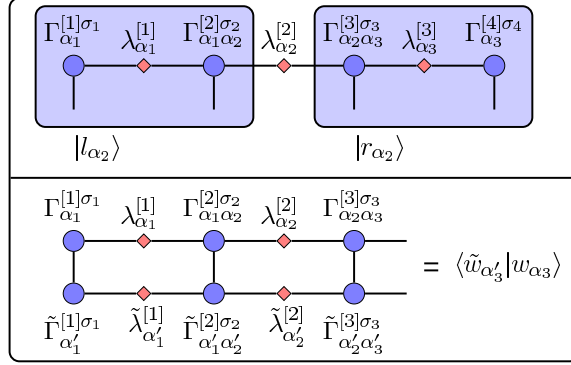


Figure 8.1: Top: Schematic of the matrix product decomposition of a four-site lattice. The circles indicate sites, i , with an applied tensor, $\Gamma^{[i]}$, and the diamonds denote bonds which carry Schmidt coefficients, $\lambda^{[i]}$, on the i^{th} bond. The shading indicates a decomposition into left and right subsystems described by a renormalized basis $|l_\alpha\rangle$ and $|r_\alpha\rangle$ of eigenvectors of the respective reduced density matrices. Bottom: Schematic depicting an overlap of two matrix product states. The top line corresponds to a state A (e.g., an ansatz state) in the matrix product representation while the bottom line corresponds to a second state E (e.g., an exact state).

of an infinite matrix product state introduced in Section 2.1.3. The coefficients $c(\{\sigma_i\})$ of the expansion of the state in the σ^z -basis,

$$|\Psi\rangle = \sum_{\{\sigma_i\}} c(\{\sigma_i\}) |\sigma_1\rangle \dots |\sigma_N\rangle \quad (8.5)$$

are given as a product of matrices:

$$c(\{\sigma_i\}) = \sum_{\alpha_1, \dots, \alpha_N} \Gamma_{\alpha_1}^{[1]\sigma_1} \lambda_{\alpha_1}^{[1]} \Gamma_{\alpha_1\alpha_2}^{[2]\sigma_2} \lambda_{\alpha_2}^{[2]} \dots \Gamma_{\alpha_N}^{[N]\sigma_N}, \quad (8.6)$$

where α indexes the auxiliary state space (of size M), Γ are rank three tensors that must be determined, and the coefficients λ are the Schmidt eigenvalues of a bipartite splitting of the system at that site, i.e. they are equal to the eigenvalues of the reduced density matrices obtained by such a splitting. In the following we denote MPS states as $|\Psi\rangle = (\Gamma_{\alpha_i\beta_i}^{[i]\sigma_i}, \lambda_{\beta_i}^{[i]})$.

As was discussed before, the accuracy of the MPS approximation depends on the decay of these eigenvalues and can be controlled by tuning the matrix dimension M . In the case of the Ising model in a transverse field, the Schmidt coefficients are found to decay very quickly. We therefore perform our calculations with a matrix size $M = 100$ and up to $N = 64$ spins. Imaginary time evolution is

used to project into the ground state. We apply a first-order Trotter decomposition with an initial time-step $d\tau = 0.05$, which is decreased to $d\tau = 0.0001$ during the simulation. Trotter errors are therefore negligible. In what follows an "exact" state (E) refers to an MPS approximation to the exact ground state.

Once the ground state has been found, we must obtain the density matrix in a common, orthonormal basis $\{|v_a\rangle\}$ for both the ansatz and exact states. We first join the two bases by concatenating Schmidt coefficients and the tensors blockwise, i.e. for two states $|\Psi\rangle = (\Gamma_{\alpha_i\beta_i}^{[i]\sigma_i}, \lambda_{\beta_i}^{[i]})$, $|\tilde{\Psi}\rangle = (\tilde{\Gamma}_{\alpha_i\beta_i}^{[i]\sigma_i}, \tilde{\lambda}_{\beta_i}^{[i]})$ we have $|\hat{\Psi}\rangle$ given by

$$\hat{\Gamma}_{\alpha\beta}^{[i]\sigma} = \begin{cases} \Gamma_{\alpha\beta}^{[i]\sigma} & \alpha, \beta \in \{1, \dots, M\} \\ \tilde{\Gamma}_{\alpha-M, \beta-M}^{[i]\sigma} & \alpha, \beta \in \{M+1, \dots, 2M\} \end{cases} \quad (8.7)$$

$$\hat{\lambda}_{\alpha}^{[i]} = \begin{cases} \lambda_{\alpha}^{[i]} & \alpha \in \{1, \dots, M\} \\ \tilde{\lambda}_{\alpha-M}^{[i]} & \alpha \in \{M+1, \dots, 2M\}. \end{cases} \quad (8.8)$$

We define the overlap matrix of two sets of states $|w_m\rangle = (\Gamma_{\alpha\beta}^{[i]\sigma_i}, \lambda_{\beta}^{[i]})$ and $|\tilde{w}_m\rangle = (\tilde{\Gamma}_{\alpha\beta}^{[i]\sigma_i}, \tilde{\lambda}_{\beta}^{[i]})$ describing some part of the system (bottom panel, Fig. 8.1), which are taken to be the Schmidt eigenvectors of a bipartite decomposition of the system:

$$\langle \tilde{w}_{\alpha'_n} | w_{\alpha_n} \rangle = \sum_{\mathcal{F}} \mathcal{F} \left(\overline{\prod_i \tilde{\Gamma}_{\alpha'_i \alpha_i}^{[i]\sigma_i} \tilde{\lambda}_{\alpha'_i}^{[i]}} \prod_i \Gamma_{\alpha_i \alpha_i}^{[i]\sigma_i} \lambda_{\alpha_i}^{[i]} \right), \quad (8.9)$$

where the summation runs over all orthogonal spin configurations and \mathcal{F} indicates the summation over all remaining indices. This allows us to find a transformation that we can use to orthonormalize the basis of $|\hat{\Psi}\rangle$ for a specific bipartition.

The reduced density matrices can now be computed using

$$\rho_{a,b}^{\text{red}} = \sum_{\alpha, \beta, t} \lambda_{\alpha} \lambda_{\beta} \langle v_a | l_{\alpha} \rangle \langle l_{\beta} | v_b \rangle \langle r_t | r_{\alpha} \rangle \langle r_{\beta} | r_t \rangle. \quad (8.10)$$

$|r_{\alpha}\rangle$ and $|l_{\alpha}\rangle$ denote states obtained from a right and left partitioning of the lattice (top panel, Fig. 8.1). The sum over states $|r_t\rangle$ traces out the right $N - n$ sites.

8.2 Indistinguishability for quantum phase transitions

8.2.1 Ising chain in transverse field

We first apply the indistinguishability measure to the simplest model with a quantum phase transition, the ferromagnetic transverse Ising model:

$$H_{\text{Is}} = - \sum_i \sigma_i^x \sigma_{i+1}^x - h \sum_i \sigma_i^z. \quad (8.11)$$

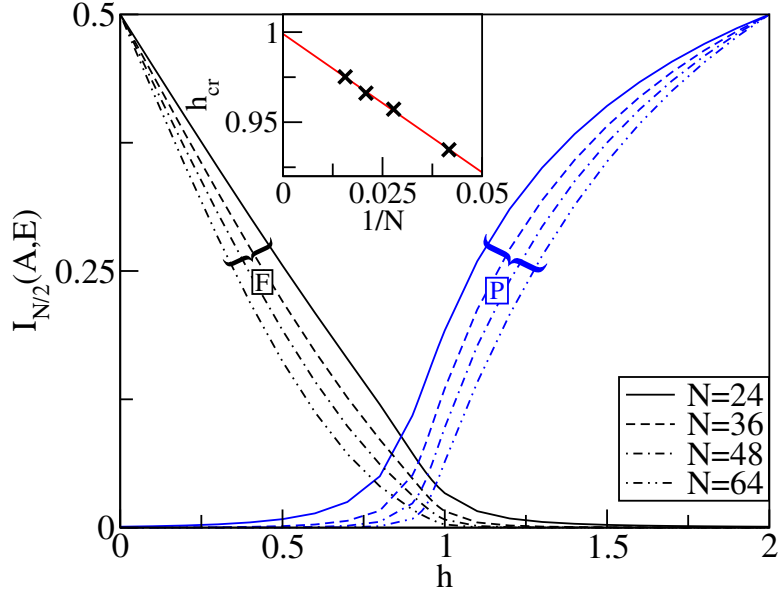


Figure 8.2: (color online) Indistinguishability $I_{N/2}(A, E)$ plotted as a function of magnetic field h for the one-dimensional transverse quantum Ising model for several different system sizes, N , and two different ansatz states, $A = F$, (ferromagnetic, $h_{\text{ref}} = 0$, black lines) and $A = P$ (paramagnetic, $h_{\text{ref}} = 2$, blue lines). The inset plots the crossing point of $I_{N/2}(F, E)$ and $I_{N/2}(P, E)$, with Ψ_P evaluated for $h_{\text{ref}} = 100$, versus N^{-1} . A straight line fit yields a quantum critical point at $h_{\text{cr}} = 0.999(1)$ as $N \rightarrow \infty$, in agreement with standard results.

Here σ_i^α , $\alpha = x, y, z$ are the Pauli matrices and the sites i are located on an N -site chain with open boundary conditions. The model displays a quantum phase transition at $h = 1$.

Physically motivated ansatz wavefunctions can be defined for Eqn. (8.11) by noting that for $h > 1$ the ground state is a paramagnet with exponentially decaying correlators, $\langle \sigma_0^x \sigma_j^x \rangle \sim \exp(-j/\xi)$, while for $h < 1$ the ground state is in the ferromagnetically ordered phase with long range order, $\langle \sigma_0^x \sigma_j^x \rangle \sim m^2$ for $j \rightarrow \infty$, where m is the spontaneous magnetization. On the ferromagnetic side the exact $h \rightarrow 0$ ground state (one of the two degenerate ground states) is given by: $\Psi_F = \prod_i |\uparrow\rangle_i$, while on the paramagnetic side in the limit $h \rightarrow \infty$ we have: $\Psi_P = \prod_i |\rightarrow\rangle_i$. Without relying on the explicit behavior of any correlation functions, we will show using I_n that for $h \neq 1$ the wavefunctions fall into two distinct correlator classes that are defined by the above ansatz states for the limiting cases. I_n thus allows an efficient test of the accuracy of ansatz states in reproducing all n -particle correlation functions of the exact state, without explicit calculation of these. We further show that the location of the transition can be accurately identified.

We focus here on calculations for large values of n that will allow us to analyze the scaling of I_n when this is an intensive quantity. Thus we consider $n = N/2$, where the total number of spins N varies. The indistinguishability $I_{n=N/2}$ of the numerically obtained ground state of Eqn. (8.11) was computed with the ferromagnetic and paramagnetic ansatz states Ψ_F and Ψ_P . It is convenient to represent the ansatz states by numerically obtained states calculated with the MPS formalism for appropriate reference values of transverse field h . Thus we define $\Psi_E(h)$ to be a numerically exact state calculated with the MPS formalism for a transverse field h . For the ferromagnetic ansatz we use $\Psi_F = \Psi_E(h_{\text{ref}} = 0)$. The paramagnetic ansatz Ψ_P can be well represented by $\Psi_E(h_{\text{ref}})$ for large values of h_{ref} . For most calculations with Ψ_P it is sufficient to use $h_{\text{ref}} = 2$ but larger values of h_{ref} will be used when extracting information about the phase transition.

The calculated indistinguishabilities $I_{N/2}(F, E)$ and $I_{N/2}(P, E)$ are shown in the main panel of Fig. 8.2 as a function of h for several system sizes. For $h \lesssim 1$, we find $I_{N/2}(F, E)$ large with a weak decay with N . In contrast, we find here a strong suppression of $I_{N/2}(P, E)$ as $N \rightarrow \infty$, implying that an optimally chosen correlator of up to $N/2$ particles will not successfully distinguish the exact state from Ψ_A^F but will successfully distinguish the exact state from the paramagnetic state for large enough N . For $h \gtrsim 1$, we find the reverse situation.

We can use I_n to accurately identify the phase transition point, h_{cr} . We search for the critical point by finding the h at which $I_{N/2}(F, E) = I_{N/2}(P, E)$ and extrapolating to the thermodynamic limit. The inset of Fig. 8.2 shows a linear extrapolation in $1/N$ that agrees with the known solution, $h_{\text{cr}} = 1$.

We compute the QCB for each of the two phases in the transverse Ising model to demonstrate that the existence of two distinct correlator classes can also be found via the scaling exponent of I_n . Fig. 8.3 plots the QCB versus h evaluated with two different methods. The dotted lines plot the finite size extrapolation of $\xi_{\text{CB}}^{\text{lim}}$ for both a ferromagnetic ($h_{\text{ref}} = 0$, black) and antiferromagnetic ($h_{\text{ref}} = 2$, blue) ansatz. The remaining lines show how the data collapse towards this line for several discrete N values. We see that the scaling exponent, ξ_{CB} , correctly identifies correlator classes on either side of the critical point. Precise location of the critical point from the QCB is complicated by the need to extrapolate an exponent and the associated numerical error. Location from the scaling of I_n as in Fig. 8.2 is more direct and appears more robust in this case.

The critical point can be defined in terms of the indistinguishability as the unique point in parameter space that, for a given ansatz wavefunction, separates regions characterized by dramatically different scaling of I_n . As demonstrated above, both the direct evaluation of I_n and evaluation of the QCB allow the critical point between two phases to be located as the point where the indistinguishability measures for the two different ansatz functions are equal. To further characterize

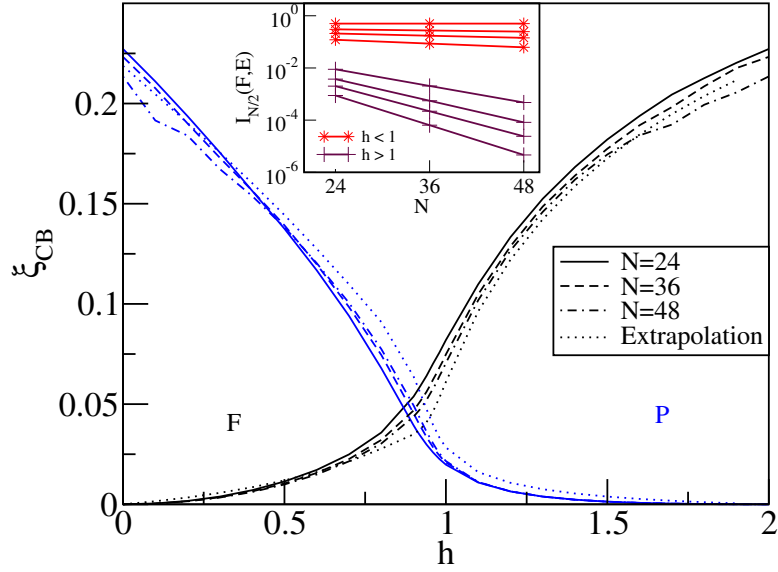


Figure 8.3: (color online) The quantum Chernoff bound versus magnetic field using the extrapolation of indistinguishability, $\xi_{\text{CB}}^{\text{lim}}$, (dotted line) and the reduced density matrices directly, ξ_{CB}^{ρ} , (solid, dashed and dot-dashed). A suppression of ξ_{CB} indicates success for the ferromagnetic, F, black lines (paramagnetic, P blue lines) ansatz for $h \lesssim 1$ ($h \gtrsim 1$). The inset plots shows a log plot of $I_{N/2}(F, E)$ versus N for several h to show an abrupt change in scaling near $h = 1$.

the critical point for finite sized systems we can define an indistinguishability susceptibility for $I_n(h_{\text{ref}}, h)$ by

$$\begin{aligned} \chi_{I_n} &= \lim_{h \rightarrow \pm h_{\text{ref}}} \frac{dI_n(\Psi_{\text{E}}(h_{\text{ref}}), \Psi_{\text{E}}(h))}{dh} \\ &= \lim_{\varepsilon \rightarrow 0} \frac{0.5 - I_n(\Psi_{\text{E}}(h_{\text{ref}}), \Psi_{\text{E}}(h_{\text{ref}} \pm \varepsilon))}{\pm \varepsilon}. \end{aligned} \quad (8.12)$$

Eqn. (8.12) should coincide with the maximum of the derivative of $I_n(h_{\text{ref}}, h)$ for a given h_{ref} . Our direct calculations of I_n show that for the transverse Ising model, the critical point can be identified with a peak in $\chi_{I_{N/2}}$ versus h .

8.2.2 Spin-1 bilinear-biquadratic chain

We now apply our distinguishability measure to analyze a richer model with ground states characterized by more complicated correlators, namely the bilinear-

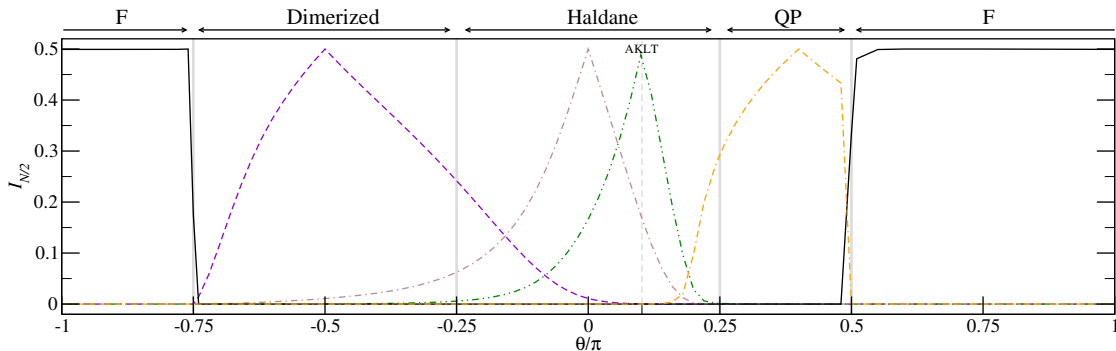


Figure 8.4: Indistinguishability versus θ for the bilinear-biquadratic Heisenberg model, Eqn. 8.13, with $N = 36$ and $n = 18$. Distinct correlator classes surround 5 different reference states for which $I_{N/2} = 1/2$: the ferromagnetic (solid), quadrupolar (dot-double dashed), Haldane (dot-dashed) and dimerized (dashed) phases. The AKLT point (double dot-dashed) at $\theta = \tan^{-1}(1/3)$ appears within the Haldane phase.

biquadratic Heisenberg chain defined by

$$H_{\text{bl-bq}} = \sum_i [\cos \theta (\mathbf{S}_i \mathbf{S}_{i+1}) + \sin \theta (\mathbf{S}_i \mathbf{S}_{i+1})^2], \quad (8.13)$$

where \mathbf{S} is the spin-1 operator and θ a parameter. A growing body of analytical and numerical work has shown that this model hosts a variety of ground state phases (for a review see Ref. [199] and references therein).

An integrable point [190, 200] at $\theta_{\text{AKLT}} = \tan^{-1} 1/3$ has a particularly simple form for the exact ground state that belongs to a class of VBS wavefunctions related to the Laughlin ansatz state [201]. The VBS state at θ_{AKLT} can be written as $\Psi_{\text{VBS}} = \prod_i (a_i^\dagger b_{i+1}^\dagger - b_i^\dagger a_{i+1}^\dagger) |0\rangle$, where a and b annihilate Schwinger bosons defined by $S^x + iS^y = a^\dagger b$, $S^z = (a^\dagger a - b^\dagger b)/2$, and $a^\dagger a + b^\dagger b = 2$. Ψ_{VBS} characterizes a state with exponentially decaying local correlators. The AKLT state is also characterized by hidden, long-ranged chain correlators [202]. Notably, this state does not break translational symmetry. On a finite chain with open boundary conditions, a four-fold degeneracy appears which is related to open spin-1/2 degrees of freedom at the ends of the chain.

We address the phases of this model from the point of view of ansatz states by taking five specific values of θ as reference points to capture the various possible phases. In particular, we choose $\theta_{\text{ref}} = \pi$ for the ferromagnetic (F) phase, $\theta_{\text{ref}} = 0.4\pi$ for the quadrupolar (QP) phase, $\theta_{\text{ref}} = 0$ and $\theta_{\text{ref}} = \theta_{\text{AKLT}}$ for the Haldane phase (corresponding to the Heisenberg and AKLT states) and $\theta_{\text{ref}} = -\pi/2$ for the dimerized phase. In addition to these ansatzes defined by the ground states of the

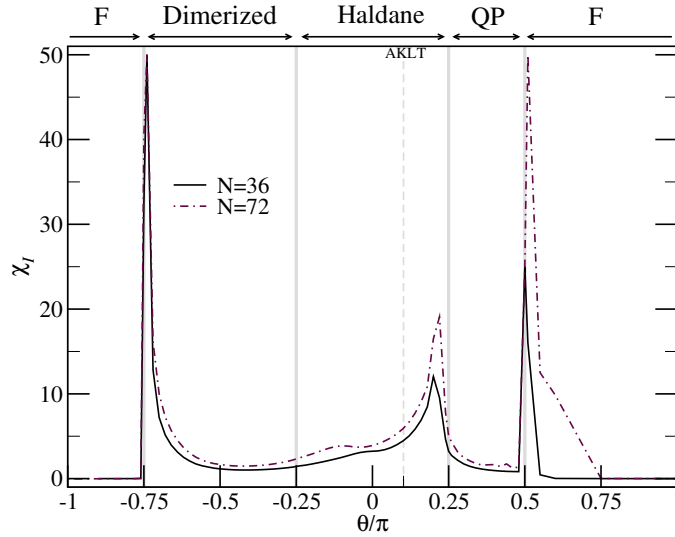


Figure 8.5: Indistinguishability susceptibility, Eqn. 8.12, computed for the bilinear-biquadratic chain, Eqn. 8.13. Here we use $N = 36, 72$, $n = N/2$ and $\varepsilon = 0.02$ for the relevant part of the phase diagram. The peaks indicate phase transitions. In the case of discontinuous transitions, peaks remain finite only due to the discretization of the values of h_{ref} .

Hamiltonian Eqn. (8.13) for the five reference θ values, we shall also consider a trial wave function for a fully dimerized state, obtained at $\theta = -\pi/2$ with a modified Hamiltonian that results from omitting all even-bond terms in Eqn. (8.13).

Since, with the exception of the AKLT state, analytic forms for the ground state wave function at these reference points are not known, the ansatz wavefunctions are obtained by numerical solution for the ground state of Eqn. (8.13) at the reference values of θ_{ref} . These numerical solutions Ψ_A are generated with the matrix product approach of Section 8.1.2 at θ_{ref} , just as the exact solutions Ψ_E are generated at arbitrary values of θ . We then calculate the indistinguishability measure, $I_{N/2}$, for system sizes $N = 24 \dots 72$ with open boundary conditions. Due to this choice of boundary conditions, we need to take N as a multiple of 3 in order to be able to capture correlations at $k = 2\pi/3$ which are important in the quadrupolar phase.

A typical result, for $N = 36$, is presented in Fig. 8.4, which shows $I_{N/2}$ as a function of θ for the five different correlator classes defined by the above values of θ_{ref} . The general variation of $I_{N/2}$ for each correlator class is consistent with what is known about the phase boundaries in this system [199, 202, 203], but also reveals several remarkable features: First, the ferromagnetic ansatz is seen to be indistinguishable from the exact ground state over a wide range of θ values, $\theta \leq -3\pi/4$ and $\theta \geq +\pi/2$, with sharp, possibly first order, transitions signaling disappearance of the ferromagnetic state at $\theta = \pi/2$ and $-3\pi/4$. Second, the

ground state of the Heisenberg point at $\theta = 0$ is in the same correlator class as the AKLT state, supporting suggestions that there is a finite range of θ over which the ground state has the symmetry of the AKLT state [202]. Third, although the indistinguishability for h_{ref} in the Haldane phase drops quickly as the dimerized phase is approached ($\theta \rightarrow -\pi/4$), the signature of the phase transition does not appear as strongly as the alternative Haldane to quadrupolar transition ($\theta \rightarrow +\pi/4$) for this system size.

Additionally, we have calculated the $n = N/2$ indistinguishability susceptibility, Eqn. 8.12, for this model with $N = 36$ and $N = 72$ (Fig. 8.5). The sharp transitions from the ferromagnetic state are reflected in large peaks in the susceptibility; the height of these peaks is controlled only by the discretization of the θ values. These sharp peaks at $\theta = \pi/2$ and $-3\pi/4$ are consistent with the possibility of first order transitions out of the ferromagnetic phase. A well-pronounced transition also appears between the Haldane and the quadrupolar phase, with a pronounced shift due to finite size effects. The indistinguishability susceptibility is thus sensitive to the difference between first order and continuous phase transitions, with the latter showing finite size shifts due to the divergence of the intrinsic length scales.

We note that, in contrast to the clear signatures for transitions from the ferromagnetic phase and from the Haldane to quadrupolar phase, the transition from the dimerized phase to the Haldane phase is only very weak at these system sizes. A small peak does emerge at $N = 72$, but for $N = 36$ the peak corresponding to the transition appears considerably flattened out, almost to a plateau, and is also considerably shifted in location. To understand this behaviour, we analyzed the fully dimerized ansatz state derived at $\theta = -\pi/2$ with the omission of all even-bond terms in Eqn. (8.13), as described above. Fig. 8.6 (b) shows that the indistinguishability for this ansatz state is relatively small, never exceeding 0.25, implying that this fully dimerized ansatz only poorly describes the dimerized phase of Eqn. (8.13), even in the proximity of the maximally dimerized point around $\theta/\pi = -0.5$. Our results thus confirm that there are strong fluctuations away from a simple state consisting entirely of products of dimers and that it is therefore difficult to precisely characterize the nature of the ground state in this parameter region.

To analyze the degree of dimerization we define a dimerization order parameter:

$$D = \frac{1}{N} \sum_{\text{bond } i} |H_i - H_{i+1}| \quad (8.14)$$

with $H_i = [\cos \theta (\mathbf{S}_i \mathbf{S}_{i+1}) + \sin \theta (\mathbf{S}_i \mathbf{S}_{i+1})^2]$. In these units, the fully dimerized state is characterized by $D = 2.63$. We can then demonstrate the degree of dimerization by direct evaluation of Eqn. 8.14. This is plotted in Fig. 8.6 (c), which shows a

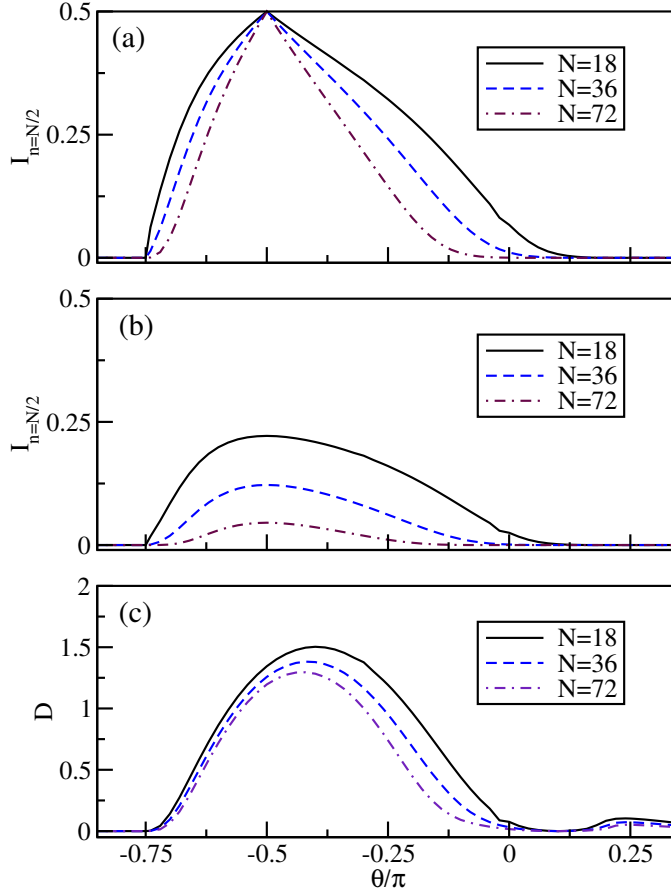


Figure 8.6: Analysis of the dimerized phase. (a) MPS ground state for $\theta = -\pi/2$ as the reference state. For small system sizes, the reference state remains a good ansatz state far beyond $\theta/\pi = -0.25$ into the Haldane regime. (b) $I_{N/2}$ for a strongly dimerized reference state obtained for $\theta = -\pi/2$ by omitting even-bond terms from the Hamiltonian, Eqn. (8.13). The indistinguishability remains small even around the maximally dimerized point near $\theta/\pi = -0.5$, indicating that a product of dimers only poorly characterizes the system. (c) Dimerization order parameter (Eqn. (8.14)) for three system sizes. The dimerization remains finite far towards the AKLT point, rendering the Haldane and dimerized phases hard to distinguish on small length scales.

finite dimerization far into the Haldane regime. For the smallest system sizes, the dimerization order parameter vanishes only at the AKLT point. This is due to the explicit breaking of translational symmetry induced by our use of open boundary conditions as well as to our restricted system sizes. We therefore expect that the weak peak in the susceptibility at $N = 72$ should become more pronounced with larger system sizes or with periodic boundaries.

8.3 Indistinguishability in the Toric Code

8.3.1 Review of the Toric Code

The toric code Hamiltonian was constructed as an exactly soluble model with a topologically ordered ground state and anyonic excitations [191, 204]. We briefly review the model and discuss its symmetry properties. The model is given by:

$$H_T = - \sum_v \prod_{j \in v} \sigma_j^x - \sum_p \prod_{j \in p} \sigma_j^z, \quad (8.15)$$

where the σ_j denote Pauli matrices at sites j on the bonds of the square lattice. The first product is over the four sites surrounding the vertex v while the second product is over the four sites around each plaquette p .

When placed on a torus, the model possesses two distinct one-dimensional \mathbb{Z}_2 symmetries. The operators $\prod_{j \in w'} \sigma_j^x$ and $\prod_{j \in w} \sigma_j^z$ both commute with H_T where w' is a loop along vertices and w is a loop along bonds. These one-dimensional operators form closed loops around either cycle of a torus. They can be used to classify topological ground state sectors.

The ground state of the toric code is then given as the equal-amplitude superposition of vortex-free states:

$$|\Psi_i\rangle = \sum_{|\xi\rangle \in \chi_i} f_i |\xi\rangle, \quad (8.16)$$

where χ_i are four spaces of such vortex-free configurations distinguished by the expectation value of the operator $\prod_{i \in w} \sigma_i^z$ for two inequivalent non-contractible loops w_1, w_2 wrapping around the torus in two different directions. f_i is a normalization factor which is equal for all sectors. By a vortex-free configuration, we mean a basis state $|\xi\rangle$ for which $\prod_{i \in \delta p} \sigma_i^z = +1$ for all plaquettes δp .

8.3.2 Computed Indistinguishability

Given the above ground states of the toric code, we can analytically compute the indistinguishability between two topologically distinct sectors. We consider a

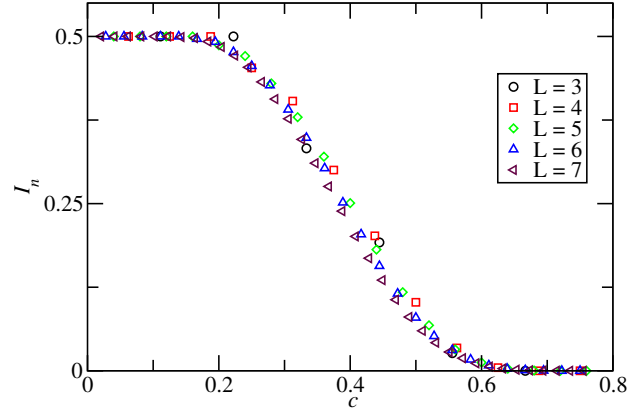


Figure 8.7: (Color online) Plot of the n -particle indistinguishability versus $c = n/N$ for several different system sizes computed using Monte Carlo selection of random but contiguous collections of spins for the toric code on a two-dimensional periodic lattice with $N = 2L^2$ spins. The graph shows data collapse and a linear scaling of n with system size, N , in contrast to a $N^{1/2}$ scaling for properly chosen spins (Eq. 8.17).

square lattice \mathcal{L} with spins located on L bonds along each dimension to give a total of $N = 2L^2$ sites. A block \mathcal{Q} of n sites is chosen for calculating I_n . The remaining sites in the lattice are denoted as \mathcal{R} , i.e., $\mathcal{L} = \mathcal{Q} \cup \mathcal{R}$.

To compute I_n we must find $\rho_A^{\mathcal{Q}}$ and $\rho_B^{\mathcal{Q}}$, the reduced density matrices on a subset $\mathcal{Q} \subset \mathcal{L}$ for two different states A and B , respectively. From Eq. 8.16 we find that the matrix elements of $\rho_A^{\mathcal{Q}} - \rho_B^{\mathcal{Q}}$ are given by:

$$\begin{aligned}
 & \langle v_{\mathcal{Q}} | \rho_A^{\mathcal{Q}} - \rho_B^{\mathcal{Q}} | w_{\mathcal{Q}} \rangle \\
 &= \sum_{|u_{\mathcal{R}}\rangle} f^2 \left\{ \sum_{|\xi_1\rangle, |\xi_2\rangle \in \chi_A} \langle v_{\mathcal{Q}} u_{\mathcal{R}} | \xi_1 \rangle \langle \xi_2 | w_{\mathcal{Q}} u_{\mathcal{R}} \rangle \right. \\
 & \quad \left. - \sum_{|\xi_1\rangle, |\xi_2\rangle \in \chi_B} \langle v_{\mathcal{Q}} u_{\mathcal{R}} | \xi_1 \rangle \langle \xi_2 | w_{\mathcal{Q}} u_{\mathcal{R}} \rangle \right\} \\
 &= \sum_{|u_{\mathcal{R}}\rangle} f^2 \left\{ \delta_A(|v_{\mathcal{Q}} u_{\mathcal{R}}\rangle) \delta_A(|w_{\mathcal{Q}} u_{\mathcal{R}}\rangle) \right. \\
 & \quad \left. - \delta_B(|v_{\mathcal{Q}} u_{\mathcal{R}}\rangle) \delta_B(|w_{\mathcal{Q}} u_{\mathcal{R}}\rangle) \right\}. \tag{8.17}
 \end{aligned}$$

Here, the states $|u_{\mathcal{R}}\rangle$ are all basis states on the sublattice \mathcal{R} , and $\delta_A(|\phi\rangle) = 1$ if $|\phi\rangle \in \text{span}(\chi_A)$, 0 otherwise.

The above expression shows that if \mathcal{Q} supports two in-equivalent loops w_1, w_2 , all sectors can be distinguished, as expected. If it only supports one such loop, only half of the sectors can be distinguished. If it does not wrap around the boundary,

no sectors can be distinguished. I_n is always either 0 or 1/2. The above explicit calculation therefore shows that for a wisely chosen \mathcal{Q} , such that it wraps the boundary ($w_1, w_2 \in \mathcal{Q}$), correlators of size $n = \mathcal{O}(\sqrt{N})$ are sufficient to reliably distinguish topological sectors.

We now ask how many measurements on *randomly* chosen spins are needed to distinguish topological sectors of the toric code. For simplicity, we consider only the case of distinguishing two sectors, i.e., we look for clusters wrapping around the torus in one non-trivial way. We seek the probability $\Pi(p)$ that a fraction p of randomly chosen sites forms a cluster that wraps around the boundary. This is the problem of percolation with periodic boundary conditions. For this problem, it is well-known that a critical p_c exists such that in the thermodynamic limit, $\Pi = 1$ for $p > p_c$ and $\Pi = 0$ otherwise. The critical behavior is in fact identical to that of standard percolation with free boundary conditions [205, 206]. These well-known results from percolation theory indicate that in order to distinguish sectors of the ground state based on purely randomly chosen sites, a cluster size $n \sim \mathcal{O}(N)$ is necessary.

A different situation occurs if we choose sites randomly, but as a contiguous blocks. The probability for a contiguous cluster of size n to wrap around the boundary, which we denote as ϱ , is given by:

$$\varrho(n) = \int_{p_c}^1 dp \delta(NP(p) - n), \quad (8.18)$$

where P is the probability for one site to lie in the percolating cluster for a completely random choice of sites. We then have $I_n = (1 - \varrho(n))/2$. We do not expect a sharp transition to appear in this quantity because there is a finite but exponentially small probability for a random block of size $n \geq \sqrt{N}$ to wrap around the boundary.

Scaling theory dictates that the behavior of P in the thermodynamic limit and in the critical region is governed by $P \sim (p - p_c)^\beta$. The divergence of the correlation length is described by $\xi \sim (p - p_c)^{-\nu}$; however, on finite systems this is bounded by L and therefore $(p - p_c) \sim L^{-1/\nu}$. We then have $P \sim L^{-\beta/\nu}$ or, equivalently, a critical cluster size $n_c \sim L^{2-\beta\nu} = L^D$, where D is the fractal dimension. If one were to grow only one cluster in the system, the probability for this cluster to percolate should increase rapidly at $n \sim \mathcal{O}(L^D)$. In two dimensions, the value of D is 91/48. We can therefore expect that a contiguous cluster of size

$$n \sim \mathcal{O}(L^{91/48}) \quad (8.19)$$

is sufficient to distinguish two sectors of the ground state.

To verify the above statement we compute I_n explicitly using a direct-sampling Monte Carlo method. We draw the configurations of a cluster with n connected

sites from a uniform distribution and measure the probability for such a cluster to support a loop wrapping around the boundary, $P(\text{loop}) = \varrho(n)$. The results of I_n versus linear scaling ratio:

$$c = \frac{n}{N}, \tag{8.20}$$

for several L are shown in Figure 8.7. The data collapse beyond a regime where finite-size effects are relevant, which agrees with the expected scaling $n \sim \mathcal{O}(L^D)$. The difference between $L^{91/48}$ and L^2 is too small to be distinguished numerically.

We have thus shown that the indistinguishability reveals the size of the operators required to identify topological sectors. For suitably chosen blocks we find $n = \mathcal{O}(\sqrt{N})$ whereas randomly chosen sites lead to $n = \mathcal{O}(N)$. In the case where a random, but contiguous choice of sites is made, the necessary block size is $n = \mathcal{O}(L^{91/48})$. I_n thus yields topologically relevant information without requiring a precise identification of the non-local symmetries defining each sector.

Chapter 9

Conclusion and outlook

9.1 Projected entangled-pair states

In the first part of this thesis, we have applied projected entangled-pair states on infinite lattices to a series of models for which we can compare to accurate results obtained with Quantum Monte Carlo. We have confirmed that the iPEPS method can be applied with excellent accuracy to first-order phase transitions using the example of the spin-flop transition in the hard-core boson model. The stability of a homogeneous system across the phase transition allows us to determine the nature of the phase transition and locate it very accurately. We expect that this will prove to be useful for applications where phase separation and coexisting order are hard to distinguish based on finite-size simulations.

The isotropic Heisenberg model and the phase transition in the dimerized Heisenberg model prove to be difficult test cases for tensor network state algorithms. The accuracy we obtain with the current computational resources is not comparable to that obtained with Quantum Monte Carlo simulations. This is due to large quantum fluctuations around the mean-field limit, which are hard to capture in a low-entanglement approximation.

To improve upon these results, we have developed a general formalism for introducing Abelian symmetries into tensor network state algorithms. The formalism relies only on properties of irreducible representations of the symmetry group and allows a generic implementation for a large class of symmetries. The formalism can be applied to any tensor network state algorithm; in this thesis, it was implemented in both projected entangled-pair states and the multi-scale entanglement renormalization ansatz. For the case of MPS, it is equivalent to the conventional approach.

Since the implementation requires additional approximations, benchmark calculations confirming the validity of the approach are required. This is particularly

important in the case of $U(1)$ symmetry, where restrictions on the allowed quantum numbers have to be introduced. In order to assess the validity, we have applied our method to the spin- $\frac{1}{2}$ Heisenberg model on an infinite square lattice with the symmetry groups \mathbb{Z}_q for $q = 2, 3$ and $U(1)$.

Our results for the finite groups show that no accuracy is lost due to the symmetric decomposition of tensors. At the same time, the number of variational parameters and the computational effort is significantly reduced. We therefore expect that exploiting these symmetries will become very useful in the context of tensor networks states.

In the case of the continuous symmetry group $U(1)$, we were able to achieve much larger bond dimensions. Nevertheless, the accuracy does not reach the level that can be obtained with finite symmetry groups. We expect, however, that if a sufficiently large number of symmetry sectors is taken into account, the accuracy will eventually become comparable to the non-symmetric case. Further research is required to understand this, in particular how this behaves for different models such as bosonic models with particle number conservation. Also, a scheme that reliably picks the relevant symmetry sectors on the auxiliary bonds and in the environment tensors without strong dependence on the initial state may be very useful.

For a frustrated model on the square lattice, we have shown that the method converges to results that agree with expectations based on mean-field simulations and previous results obtained using the Coupled-Cluster Method. Whereas the applicability of path integral Monte Carlo methods to such systems is limited by the sign problem, the accuracy of iPEPS is only limited by the entanglement of the ground state and frustration does not introduce additional difficulties. We therefore expect that the method will become a valuable tool for such systems.

We expect that PEPS, along with other tensor network state methods, will become a valuable tool for studying frustrated spin systems and fermionic systems where few reliable methods are available. For example, recent results in Ref. [104] indicate that iPEPS is competitive with the best known variational states for the two-dimensional t - J model. In that study, iPEPS and DMRG results were combined to increase confidence in the results. This will likely be a widely used approach in the future, as the different approximations – well-understood convergence with the bond dimension, but a limitation to finite and relatively small systems in the case of DMRG and few available bond dimensions, but no need for finite-size extrapolation in the case of iPEPS – can complement one another. In this thesis, such a combination of techniques was applied to the $SU(3)$ Heisenberg model in Chapter 7.

9.2 Supersymmetric lattice fermions

Using a variety of numerical approaches, we have explored criticality in a model of interacting fermions on the chain and square lattice. The case of the chain is well-understood and served as a case study to accumulate experience with our numerical approaches. We demonstrated that the MERA is able to accurately find the central charge and scaling dimensions and confirm that the continuum limit of this model is described by the first $\mathcal{N} = 2$ supersymmetric minimal model. For finite systems, we obtained an expression for the oscillatory part of the entropy due to open boundary conditions, which we confirmed for a wide range of system sizes.

In the case of the square ladder, on the other hand, the model poses serious challenges to our numerical approaches. Matching the spectrum obtained from exact diagonalization to the second minimal model has turned out to be difficult, as only few levels are obtained accurately, but many additional levels appear for which no explanation in terms of the minimal model can be found.

The reliability of fits to finite-size entropies for open and periodic systems is impaired by large subleading corrections, which cannot be accounted for as an analytical form is not known. Such strong finite-size corrections for the entropy are highly unusual and to our knowledge have not been observed previously. In Ref. [173], several cases for unusual corrections are discussed, but a numerical analysis for a specific model is still open; also, their results do not apply directly to finite systems. It is therefore still open whether the corrections we obtain are connected to those of Ref. [173].

Some evidence in favor of the second minimal model as appropriate theory for the ladder was found studying the density (one-point function) on open ladders. Our numerical results are in good agreement with the hypothesis that the density is a quasi-primary operator with conformal weight $1/4$. A strong tie to the minimal model can be established by an explicit calculation of the density on open ladders, which gives excellent agreement with numerical results.

Applying the MERA to the case of the square ladder has turned out to be challenging. Simulations are rendered difficult by the large number of sites that have to be grouped in order to accommodate the operators. Also, the bond dimension we reach does not seem to be sufficient to accurately describe the correlation functions and therefore extract the scaling dimensions. Nevertheless, a value of the central charge close to $c = 1.5$ was confirmed.

Several directions for future research suggest themselves: Understanding the finite-size corrections of the block entropies for finite systems may help to explain the deviation from the expected central charge. This will be useful in a more general context as finite-size entropy calculations are increasingly being used as tool to determine the central charge for critical one-dimensional systems. The

problem can also be tackled from a very different side by analyzing the phase diagram of the model under perturbations. The only known perturbation that does not break supersymmetry is staggering of the couplings. For the case of the chain, this has been analyzed in detail; a similar analysis for the ladder appears as natural route to understand its critical behavior.

9.3 The $SU(3)$ Heisenberg model

We have studied the $SU(3)$ Heisenberg model using two different approaches, namely projected entangled-pair states on infinite lattices and density-matrix renormalization group on finite lattices. Using this combination of techniques, we were able to understand the ground state both in the thermodynamic limit and on finite systems. In particular, the DMRG simulations allowed us to understand the effect of the boundary conditions on the order.

Both approaches clearly confirm the presence of a characteristic three-sublattice order. On small systems, this order may be suppressed by taking periodic or cylindrical boundary conditions as a state made up of isolated chains of length 6 becomes energetically favorable. We therefore use open boundary conditions to extract quantitative results.

Both methods suggest a local moment between 30 % and 40 % of the saturation value in the case of the square lattice, and close to 50 % in the case of the triangular lattice. Agreement between the methods is good for both the energy and local moments. The DMRG results can therefore be taken as confirmation of the iPEPS result, which is obtained on infinite lattices and is therefore free of uncertainties due to boundary and finite-size effects, but displays a strong dependence on the value of the bond dimension.

Our results also underline the usefulness of finite-size DMRG calculations for two-dimensional systems, which, despite of their exponential scaling in the width of the system, allow the investigation of much larger system sizes than exact diagonalization. This effect is even more pronounced in the case of models with a larger physical dimension where exact diagonalization is limited to very small systems, while DMRG simulations do not necessarily suffer equally.

9.4 Indistinguishability

In many situations, numerically obtained wavefunctions have to be compared against ansatz wavefunctions or wavefunctions obtained for a different effective model or a different set of parameters. We have introduced the indistinguishability as a means of comparing wavefunctions if simple local order parameters do

not exist or are unknown. The indistinguishability I_n quantifies the ability of any set of n -particle correlators to distinguish two states, with a value $I_n > 0$ in the thermodynamic limit showing that two states lie in the same correlator class and a value $I_n = 0$ indicating that they lie in different classes. The scaling to the thermodynamic behavior was discussed and it was shown that the quantum Chernoff bound provides an effective means of analyzing the scaling behavior from small systems.

We first applied the method to two one-dimensional examples, the well-known Ising chain in transverse field, and the spin-1 bilinear-biquadratic chain. We compare physically motivated ansatz wavefunctions for the various phases of these models against numerically obtained wavefunctions and show that the phase boundaries can be accurately obtained from the indistinguishability. Furthermore, we define the indistinguishability susceptibility as additional measure to locate quantum phase transitions.

Secondly, we have applied the indistinguishability for a model which exhibits topological order, the Toric code. We have considered the question of how many sites n are necessary to reliably distinguish the different degenerate ground states of the Toric code in a system with a total of N sites. We find that if the sites are carefully chosen, $n \sim \mathcal{O}(\sqrt{N})$ is sufficient, while for a randomly chosen (but contiguous) block of spins, $n \sim \mathcal{O}(N)$ is required.

List of publications

- [1] B. Bauer, G. Vidal, and M. Troyer, “Assessing the accuracy of projected entangled-pair states on infinite lattices,” *Journal of Statistical Mechanics: Theory and Experiment*, P09006(2009)
- [2] B. Bauer, V.W. Scarola, K.B. Whaley, and M. Troyer, “Distinguishing phases with ansatz wave functions,” *Physical Review B* **81**, 085118 (2010)
- [3] B. Bauer, E. Gull, S. Trebst, M. Troyer, and D.A. Huse, “Optimized broad-histogram simulations for strong first-order phase transitions: droplet transitions in the large-Q Potts model,” *Journal of Statistical Mechanics: Theory and Experiment*, P01020(2010)
- [4] K. Marti, B. Bauer, M. Reiher, and M. Troyer, “Complete-graph tensor network states: A new fermionic wave function ansatz for molecules,” *New J. Phys.* **12**, 103008 (2010)
- [5] D. Koop, E. Santos, B. Bauer, M. Troyer, J. Freire, and C.T. Silva, “Bridging Workflow and Data Provenance Using Strong Links,” *Lecture Notes in Computer Science* **6187**, 397 (2010)
- [6] P. Corboz, R. Orus, B. Bauer, and G. Vidal, “Simulation of strongly correlated fermions in two spatial dimensions with fermionic projected entangled-pair states,” *Physical Review B* **81**, 165104 (2010)
- [7] B. Bauer, P. Corboz, R. Orús, and M. Troyer, “Implementing global abelian symmetries in projected entangled-pair state algorithms,” *Phys. Rev. B* **83**, 125106 (2011)
- [8] B Bauer *et al.*, “The ALPS project release 2.0: open source software for strongly correlated systems,” *Journal of Statistical Mechanics: Theory and Experiment* **2011**, P05001 (2011)
- [9] Hao Wang, B. Bauer, M. Troyer, and V. W. Scarola, “Identifying quantum topological phases through statistical correlation,” *Phys. Rev. B* **83**, 115119 (2011)

LIST OF PUBLICATIONS

Bibliography

- [10] D. C. Tsui, H. L. Stormer, and A. C. Gossard, “Two-Dimensional Magneto-transport in the Extreme Quantum Limit,” *Phys. Rev. Lett.* **48**, 1559–1562 (1982)
- [11] X.-G. Wen, “Topological order in rigid states,” *Int. J. Mod. Phys B* **4**, 239 (1990)
- [12] R. B. Laughlin, “Anomalous Quantum Hall Effect: An Incompressible Quantum Fluid with Fractionally Charged Excitations,” *Phys. Rev. Lett.* **50**, 1395–1398 (May 1983)
- [13] J. G. Bednorz and K. A. Müller, “Possible high- T_c superconductivity in the Ba-La-Cu-O system,” *Zeitschrift für Physik B Condensed Matter* **64**, 189–193 (1986)
- [14] F. C. Zhang and T. M. Rice, “Effective Hamiltonian for the superconducting Cu oxides,” *Phys. Rev. B* **37**, 3759–3761 (Mar 1988)
- [15] S. R. White, “Density matrix formulation for quantum renormalization groups,” *Phys. Rev. Lett.* **69**, 2863 (1992)
- [16] F. Verstraete and J. I. Cirac, “Renormalization algorithms for Quantum-Many Body Systems in two and higher dimensions,” Preprint(2004), [arXiv:cond-mat/0407066](https://arxiv.org/abs/cond-mat/0407066)
- [17] Y.-Y. Shi, L.-M. Duan, and G. Vidal, “Classical simulation of quantum many-body systems with a tree tensor network,” *Phys. Rev. A* **74**, 022320 (2006)
- [18] G. Vidal, “Entanglement Renormalization,” *Phys. Rev. Lett.* **99**, 220405 (2007)
- [19] G. Vidal, “Class of Quantum Many-Body States That Can Be Efficiently Simulated,” *Phys. Rev. Lett.* **101**, 110501 (2008)

- [20] Norbert Schuch, Michael M. Wolf, Frank Verstraete, and J. Ignacio Cirac, “Simulation of Quantum Many-Body Systems with Strings of Operators and Monte Carlo Tensor Contractions,” *Phys. Rev. Lett.* **100**, 040501 (2008)
- [21] Anders W. Sandvik, “Scale-Renormalized Matrix-Product States for Correlated Quantum Systems,” *Phys. Rev. Lett.* **101**, 140603 (Oct 2008)
- [22] F Mezzacapo, N Schuch, M Boninsegni, and J I Cirac, “Ground-state properties of quantum many-body systems: entangled-plaquette states and variational Monte Carlo,” *New Journal of Physics* **11**, 083026 (2009)
- [23] Hitesh J. Changlani, Jesse M. Kinder, C. J. Umrigar, and Garnet Kin-Lic Chan, “Approximating strongly correlated wave functions with correlator product states,” *Phys. Rev. B* **80**, 245116 (Dec 2009)
- [24] R. Hübener, C. Kruszynska, L. Hartmann, W. Dür, F. Verstraete, J. Eisert, and M. B. Plenio, “Renormalization algorithm with graph enhancement,” *Phys. Rev. A* **79**, 022317 (Feb 2009)
- [25] R. Hübener, V Nebendahl, and W Dür, “Concatenated tensor network states,” *New Journal of Physics* **12**, 025004 (2010)
- [26] Ling Wang, Ying-Jer Kao, and Anders W. Sandvik, “Plaquette renormalization scheme for tensor network states,” *Phys. Rev. E* **83**, 056703 (May 2011)
- [27] Tobias J Osborne, “Hamiltonian Complexity,” Preprint(2011), [arXiv:1106.5875](https://arxiv.org/abs/1106.5875)
- [28] Matthias Troyer and Uwe-Jens Wiese, “Computational Complexity and Fundamental Limitations to Fermionic Quantum Monte Carlo Simulations,” *Phys. Rev. Lett.* **94**, 170201 (May 2005)
- [29] J. Eisert, M. Cramer, and M. B. Plenio, “Colloquium: Area laws for the entanglement entropy,” *Rev. Mod. Phys.* **82**, 277–306 (2010)
- [30] G Vitagliano, A Riera, and J I Latorre, “Volume-law scaling for the entanglement entropy in spin-1/2 chains,” *New Journal of Physics* **12**, 113049 (2010)
- [31] G. Vidal, J.I. Latorre, E. Rico, and A. Kitaev, “Entanglement in Quantum Critical Phenomena,” *Phys. Rev. Lett.* **90**, 227902 (2003)
- [32] M B Hastings, “An area law for one-dimensional quantum systems,” *Journal of Statistical Mechanics: Theory and Experiment* **2007**, P08024 (2007)

- [33] Christoph Holzhey, Finn Larsen, and Frank Wilczek, “Geometric and renormalized entropy in conformal field theory,” *Nuclear Physics B* **424**, 443 – 467 (1994)
- [34] Pasquale Calabrese and John Cardy, “Entanglement entropy and quantum field theory,” *Journal of Statistical Mechanics: Theory and Experiment* **2004**, P06002 (2004)
- [35] M. Cramer, J. Eisert, M. B. Plenio, and J. Dreißig, “Entanglement-area law for general bosonic harmonic lattice systems,” *Phys. Rev. A* **73**, 012309 (Jan 2006)
- [36] Michael M. Wolf, “Violation of the Entropic Area Law for Fermions,” *Phys. Rev. Lett.* **96**, 010404 (Jan 2006)
- [37] Fabien Alet, Sylvain Capponi, Nicolas Laflorencie, and Matthieu Mambrini, “Valence Bond Entanglement Entropy,” *Phys. Rev. Lett.* **99**, 117204 (Sep 2007)
- [38] Ravindra W. Chhajlany, Piotr Tomczak, and Antoni Wójcik, “Topological Estimator of Block Entanglement for Heisenberg Antiferromagnets,” *Phys. Rev. Lett.* **99**, 167204 (Oct 2007)
- [39] Ann B. Kallin, Iván González, Matthew B. Hastings, and Roger G. Melko, “Valence Bond and von Neumann Entanglement Entropy in Heisenberg Ladders,” *Phys. Rev. Lett.* **103**, 117203 (Sep 2009)
- [40] Norbert Schuch, Michael M. Wolf, Frank Verstraete, and J. Ignacio Cirac, “Entropy Scaling and Simulability by Matrix Product States,” *Phys. Rev. Lett.* **100**, 030504 (Jan 2008)
- [41] Norbert Schuch, Ignacio Cirac, and Frank Verstraete, “Computational Difficulty of Finding Matrix Product Ground States,” *Phys. Rev. Lett.* **100**, 250501 (2008)
- [42] Norbert Schuch and J. Ignacio Cirac, “Matrix product state and mean-field solutions for one-dimensional systems can be found efficiently,” *Phys. Rev. A* **82**, 012314 (2010)
- [43] A.Y. Kitaev, A.H. Shen, and M.N. Vyalyi, *Classical and Quantum Computation*, Graduate Studies in Mathematics (Oxford University Press, 2002)
- [44] Norbert Schuch and Frank Verstraete, “Computational complexity of interacting electrons and fundamental limitations of density functional theory,” *Nat. Phys.* **5**, 732–735 (10 2009)

- [45] Julia Kempe, Alexei Kitaev, and Oded Regev, “The Complexity of the Local Hamiltonian Problem,” *SIAM Journal on Computing* **35**, 1070–1097 (2006)
- [46] Roberto Oliveira and Barbara M. Terhal, “The complexity of quantum spin systems on a two-dimensional square lattice,” *Quant. Inf. and Comp.* **8**, 900 (2008)
- [47] Dorit Aharonov, Daniel Gottesman, Sandy Irani, and Julia Kempe, “The Power of Quantum Systems on a Line,” *Communications in Mathematical Physics* **287**, 41–65 (2009)
- [48] Kenneth G. Wilson, “The renormalization group: Critical phenomena and the Kondo problem,” *Rev. Mod. Phys.* **47**, 773–840 (Oct 1975)
- [49] S. R. White and R. M. Noack, “Real-space quantum renormalization groups,” *Phys. Rev. Lett.* **68**, 3487–3490 (Jun 1992)
- [50] U. Schollwöck, “The density-matrix renormalization group,” *Rev. Mod. Phys.* **77**, 259–315 (2005)
- [51] S. Östlund and S. Rommer, “Thermodynamic Limit of Density Matrix Renormalization,” *Phys. Rev. Lett.* **75**, 3537 (1995)
- [52] R. J. Baxter, “Dimers on a Rectangular Lattice,” *Journal of Mathematical Physics* **9**, 650–654 (1968)
- [53] M. Fannes, B. Nachtergaele, and R. Werner, “Finitely correlated states on quantum spin chains,” *Communications in Mathematical Physics* **144**, 443–490 (1992)
- [54] S. Liang and H. Pang, “Approximate diagonalization using the density-matrix renormalization-group method: A two-dimensional perspective,” *Phys. Rev. B* **49**, 9214 (1994)
- [55] E.M. Stoudenmire and S.R. White, “Studying Two Dimensional Systems With the Density Matrix Renormalization Group,” Preprint(2011), [arXiv:1105.1374](https://arxiv.org/abs/1105.1374)
- [56] G. Vidal, “Efficient Classical Simulation of Slightly Entangled Quantum Computations,” *Phys. Rev. Lett.* **91**, 147902 (2003)
- [57] G. Vidal, “Classical Simulation of Infinite-Size Quantum Lattice Systems in One Spatial Dimension,” *Phys. Rev. Lett.* **98**, 070201 (2007)

- [58] Ulrich Schollwöck, “The density-matrix renormalization group in the age of matrix product states,” *Annals of Physics* **326**, 96–192 (2011)
- [59] C. Lanczos, “An Iteration Method for the Solution of the Eigenvalue Problem of Linear Differential and Integral Operators,” *J. Res. Natl. Bur. Stand.* **45**, 255 (1950)
- [60] Gerard L. G. Sleijpen and Henk A. Van der Vorst, “A Jacobi-Davidson Iteration Method for Linear Eigenvalue Problems,” *SIAM Review* **42**, 267–293 (2000)
- [61] Steven R. White, “Density matrix renormalization group algorithms with a single center site,” *Phys. Rev. B* **72**, 180403 (Nov 2005)
- [62] Guifré Vidal, “Efficient Simulation of One-Dimensional Quantum Many-Body Systems,” *Phys. Rev. Lett.* **93**, 040502 (Jul 2004)
- [63] F. Verstraete, J. J. García-Ripoll, and J. I. Cirac, “Matrix Product Density Operators: Simulation of Finite-Temperature and Dissipative Systems,” *Phys. Rev. Lett.* **93**, 207204 (Nov 2004)
- [64] Steven R. White and Adrian E. Feiguin, “Real-Time Evolution Using the Density Matrix Renormalization Group,” *Phys. Rev. Lett.* **93**, 076401 (Aug 2004)
- [65] A J Daley, C Kollath, U Schollwöck, and G Vidal, “Time-dependent density-matrix renormalization-group using adaptive effective Hilbert spaces,” *Journal of Statistical Mechanics: Theory and Experiment* **2004**, P04005 (2004)
- [66] R. Orús and G. Vidal, “Infinite time-evolving block decimation algorithm beyond unitary evolution,” *Phys. Rev. B* **78**, 155117 (2008)
- [67] G. Sierra and M. A. Martin-Delgado, “The Density Matrix Renormalization Group, Quantum Groups and Conformal Field Theory,” Preprint(1998), [arXiv:cond-mat/9811170](https://arxiv.org/abs/cond-mat/9811170)
- [68] Tomotoshi Nishino and Kouichi Okunishi, “A Density Matrix Algorithm for 3D Classical Models,” *Journal of the Physical Society of Japan* **67**, 3066–3072 (1998)
- [69] T. Nishino, K. Okunushi, Y. Hieida, N. Maeshima, and Y. Akutsu, “Self-consistent tensor product variational approximation for 3D classical models,” *Nucl. Phys. B* **575**, 504–512 (2000)

- [70] Y. Nishio, N. Maeshima, A. Gendiar, and T. Nishino, “Tensor Product Variational Formulation for Quantum Systems,” Preprint(2004), [arXiv:cond-mat/0401115](#)
- [71] J. Jordan, R. Orús, G. Vidal, F. Verstraete, and J. I. Cirac, “Classical Simulation of Infinite-Size Quantum Lattice Systems in Two Spatial Dimensions,” *Phys. Rev. Lett.* **101**, 250602 (2008)
- [72] T. Nishino, Y. Hieida, K. Okunushi, N. Maeshima, Y. Akutsu, and A. Gendiar, “Two-Dimensional Tensor Product Variational Formulation,” *Prog. Theor. Phys.* **105**, 409–417 (2001)
- [73] Nobuya Maeshima, Yasuhiro Hieida, Yasuhiro Akutsu, Tomotoshi Nishino, and Kouichi Okunishi, “Vertical density matrix algorithm: A higher-dimensional numerical renormalization scheme based on the tensor product state ansatz,” *Phys. Rev. E* **64**, 016705 (Jun 2001)
- [74] A. Gendiar, N. Maeshima, and T. Nishino, “Stable Optimization of a Tensor Product Variational State,” *Progr. Theor. Phys.* **110**, 691–699 (2003)
- [75] A. Gendiar, T. Nishino, and R. Derian, “Estimation of the Magnetic Critical Exponent by Tensor Product Variational Approach,” *Acta Phys. Slov.* **55**, 141 (2005)
- [76] H.C. Jiang, Z.Y. Weng, and T. Xiang, “Accurate Determination of Tensor Network State of Quantum Lattice Models in Two Dimensions,” *Phys. Rev. Lett.* **101**, 090603 (2008)
- [77] Z.-C. Gu, M. Levin, and X.-G. Wen, “Tensor-entanglement renormalization group approach to 2D quantum systems,” *Phys. Rev. B* **78**, 205116 (2008)
- [78] Z. Y. Xie, H. C. Jiang, Q. N. Chen, Z. Y. Weng, and T. Xiang, “Second Renormalization of Tensor-Network States,” *Phys. Rev. Lett.* **103**, 160601 (2009)
- [79] Román Orús and Guifré Vidal, “Simulation of two-dimensional quantum systems on an infinite lattice revisited: Corner transfer matrix for tensor contraction,” *Phys. Rev. B* **80**, 094403 (2009)
- [80] Ling Wang, Iztok Pižorn, and Frank Verstraete, “Monte Carlo simulation with tensor network states,” *Phys. Rev. B* **83**, 134421 (Apr 2011)
- [81] Iztok Pižorn, Ling Wang, and Frank Verstraete, “Time evolution of projected entangled pair states in the single-layer picture,” *Phys. Rev. A* **83**, 052321 (May 2011)

-
- [82] V. Murg, F. Verstraete, and J. I. Cirac, “Variational study of hard-core bosons in a two-dimensional optical lattice using projected entangled pair states,” *Phys. Rev. A* **75**, 033605 (Mar 2007)
- [83] Jacob Jordan, Román Orús, and Guifré Vidal, “Numerical study of the hard-core Bose-Hubbard model on an infinite square lattice,” *Phys. Rev. B* **79**, 174515 (2009)
- [84] Pochung Chen, Chen-Yen Lai, and Min-Fong Yang, “Numerical study of spin-1/2 XXZ model on square lattice from tensor product states,” *J. Stat. Mech.* **2009**, P10001 (2009)
- [85] A. Isacsson and Olav F. Syljuasen, “Variational treatment of the Shastry-Sutherland antiferromagnet using projected entangled pair states,” *Phys. Rev. E* **74**, 026701 (2006)
- [86] V. Murg, F. Verstraete, and J. I. Cirac, “Exploring frustrated spin systems using projected entangled pair states,” *Phys. Rev. B* **79**, 195119 (May 2009)
- [87] Bo Li, Sheng-Hao Li, and Huan-Qiang Zhou, “Quantum phase transitions in a two-dimensional quantum XYX model: Ground-state fidelity and entanglement,” *Phys. Rev. E* **79**, 060101 (Jun 2009)
- [88] Pochung Chen, Chen-Yen Lai, and Min-Fong Yang, “Field-induced spin supersolidity in frustrated $S = \frac{1}{2}$ spin-dimer models,” *Phys. Rev. B* **81**, 020409 (2010)
- [89] Y.-H. Chan, Y.-J. Han, and L.-M. Duan, “Supersolid and charge-density-wave states from anisotropic interaction in an optical lattice,” *Phys. Rev. A* **82**, 053607 (Nov 2010)
- [90] Michael Lubasch, Valentin Murg, Ulrich Schneider, J. Ignacio Cirac, and Mari-Carmen Banuls, “Adiabatic preparation of a Heisenberg antiferromagnet using an optical superlattice,” Preprint(2011), [arXiv:1106.1628](https://arxiv.org/abs/1106.1628)
- [91] N. Schuch, M. Wolf, F. Verstraete, and J.I. Cirac, “The computational complexity of PEPS,” *Phys. Rev. Lett.* **98**, 140506 (2007)
- [92] Tomotoshi Nishino and Kouichi Okunishi, “Corner Transfer Matrix Renormalization Group Method,” *Journal of the Physical Society of Japan* **65**, 891–894 (1996)
- [93] Philippe Corboz, Jacob Jordan, and Guifré Vidal, “Simulation of fermionic lattice models in two dimensions with projected entangled-pair states: Next-nearest neighbor Hamiltonians,” *Phys. Rev. B* **82**, 245119 (Dec 2010)

BIBLIOGRAPHY

- [94] Iztok Pižorn and Frank Verstraete, “Fermionic implementation of projected entangled pair states algorithm,” *Phys. Rev. B* **81**, 245110 (2010)
- [95] Robert N. C. Pfeifer, Glen Evenbly, and Guifré Vidal, “Entanglement renormalization, scale invariance, and quantum criticality,” *Phys. Rev. A* **79**, 040301 (2009)
- [96] V. Giovannetti, S. Montangero, and Rosario Fazio, “Quantum Multiscale Entanglement Renormalization Ansatz Channels,” *Phys. Rev. Lett.* **101**, 180503 (2008)
- [97] G. Evenbly and G. Vidal, “Algorithms for entanglement renormalization,” *Phys. Rev. B* **79**, 144108 (2009)
- [98] P. Corboz, G. Evenbly, F. Verstraete, and G. Vidal, “Simulation of interacting fermions with entanglement renormalization,” *Phys. Rev. A* **81**, 010303(R) (2010)
- [99] P. Corboz and G. Vidal, “Fermionic multi-scale entanglement renormalization ansatz,” *Phys. Rev. B* **80**, 165129 (2009)
- [100] Christina V. Kraus, Norbert Schuch, Frank Verstraete, and J. Ignacio Cirac, “Fermionic projected entangled pair states,” *Phys. Rev. A* **81**, 052338 (2010)
- [101] T. Barthel, C. Pineda, and J. Eisert, “Contraction of fermionic operator circuits and the simulation of strongly correlated fermions,” *Phys. Rev. A* **80**, 042333 (2009)
- [102] Q.-Q. Shi, S.-H. Li, J.-H. Zhao, and H.-Q. Zhou, “Graded Projected Entangled-Pair State Representations and An Algorithm for Translationally Invariant Strongly Correlated Electronic Systems on Infinite-Size Lattices in Two Spatial Dimensions,” Preprint(2009), [arXiv:0907.5520](https://arxiv.org/abs/0907.5520)
- [103] Z.-C. Gu, F. Verstraete, and X.-G. Wen, “Grassmann tensor network states and its renormalization for strongly correlated fermionic and bosonic states,” Preprint(2010), [arXiv:1004.2563](https://arxiv.org/abs/1004.2563)
- [104] P. Corboz, S.R. White, G. Vidal, and M. Troyer, “Stripes in the two-dimensional t-J model with infinite projected entangled-pair states,” Preprint(2011), [arXiv:1104.5463](https://arxiv.org/abs/1104.5463)
- [105] M Reiher and A Wolf, *Relativistic Quantum Chemistry* (Wiley-VCH, 2009)

-
- [106] Steven R. White and Richard L. Martin, “Ab initio quantum chemistry using the density matrix renormalization group,” *The Journal of Chemical Physics* **110**, 4127–4130 (1999)
- [107] G. K.-L. Chan *et al.*, “An Introduction to the Density Matrix Renormalization Group Ansatz in Quantum Chemistry,” in *Frontiers in Quantum Systems in Chemistry and Physics*, Progress in Theoretical Chemistry and Physics, Vol. 18 (Springer Netherlands, 2008) pp. 49–65
- [108] Konrad Heinrich Marti and Markus Reiher, “The Density Matrix Renormalization Group Algorithm in Quantum Chemistry,” *Zeitschrift für Physikalische Chemie* **224**, 583–599 (2010)
- [109] Ö. Legeza and J. Sólyom, “Optimizing the density-matrix renormalization group method using quantum information entropy,” *Phys. Rev. B* **68**, 195116 (2003)
- [110] Gerrit Moritz, Bernd Artur Hess, and Markus Reiher, “Convergence behavior of the density-matrix renormalization group algorithm for optimized orbital orderings,” *The Journal of Chemical Physics* **122**, 024107 (2005)
- [111] Debashree Ghosh, Johannes Hachmann, Takeshi Yanai, and Garnet Kin-Lic Chan, “Orbital optimization in the density matrix renormalization group, with applications to polyenes and beta-carotene,” *The Journal of Chemical Physics* **128**, 144117 (2008)
- [112] G. Barcza, Ö. Legeza, K. H. Marti, and M. Reiher, “Quantum-information analysis of electronic states of different molecular structures,” *Phys. Rev. A* **83**, 012508 (Jan 2011)
- [113] David A. Huse and Veit Elser, “Simple Variational Wave Functions for Two-Dimensional Heisenberg Spin-1/2 Antiferromagnets,” *Phys. Rev. Lett.* **60**, 2531–2534 (1988)
- [114] A. W. Sandvik and G. Vidal, “Variational Quantum Monte Carlo Simulations with Tensor-Network States,” *Phys. Rev. Lett.* **99**, 220602 (2007)
- [115] Germán Sierra and Tomotoshi Nishino, “The density matrix renormalization group method applied to interaction round a face Hamiltonians,” *Nuclear Physics B* **495**, 505 – 532 (1997)
- [116] J. Dukelsky, M. A. Martín-Delgado, T. Nishino, and G. Sierra, “Equivalence of the variational matrix product method and the density matrix renormalization group applied to spin chains,” *EPL (Europhysics Letters)* **43**, 457 (1998)

BIBLIOGRAPHY

- [117] Wada Tatsuaki, “Interaction-round-a-face density-matrix renormalization-group method applied to rotational-invariant quantum spin chains,” *Phys. Rev. E* **61**, 3199–3206 (2000)
- [118] Wada Tatsuaki and Tomotoshi Nishino, “Interaction-round-a-face density-matrix renormalization-group method,” *Computer Physics Communications* **142**, 164 – 167 (2001)
- [119] Ian P. McCulloch and Miklos Gulácsi, “Density Matrix Renormalisation Group Method and Symmetries of the Hamiltonian,” *Aust. J. Phys.* **53**, 597–612 (2000)
- [120] Ian P. McCulloch and Miklos Gulácsi, “Total spin in the density matrix renormalization group algorithm,” *Phil. Mag. Lett.* **81**, 447 – 453 (2001)
- [121] I. P. McCulloch and M. Gulácsi, “The non-Abelian density matrix renormalization group algorithm,” *EPL (Europhysics Letters)* **57**, 852 (2002)
- [122] Lukasz Cincio, Jacek Dziarmaga, and Marek M. Rams, “Multiscale Entanglement Renormalization Ansatz in Two Dimensions: Quantum Ising Model,” *Phys. Rev. Lett.* **100**, 240603 (Jun 2008)
- [123] H. H. Zhao, Z. Y. Xie, Q. N. Chen, Z. C. Wei, J. W. Cai, and T. Xiang, “Renormalization of tensor-network states,” *Phys. Rev. B* **81**, 174411 (2010)
- [124] G. Evenbly, P. Corboz, and G. Vidal, “Nonlocal scaling operators with entanglement renormalization,” *Phys. Rev. B* **82**, 132411 (2010)
- [125] Sukhwinder Singh, Robert N. C. Pfeifer, and Guifre Vidal, “Tensor network states and algorithms in the presence of a global U(1) symmetry,” *Phys. Rev. B* **83**, 115125 (Mar 2011)
- [126] Sukhwinder Singh, Robert N. C. Pfeifer, and Guifré Vidal, “Tensor network decompositions in the presence of a global symmetry,” *Phys. Rev. A* **82**, 050301 (2010)
- [127] F. Alet *et al.*, “The ALPS project: Open Source Software for Strongly Correlated Systems,” *Journal of the Physical Society of Japan* **74**, 30–35 (2005)
- [128] A.F. Albuquerque *et al.*, “The ALPS project release 1.3: Open-source software for strongly correlated systems,” *Journal of Magnetism and Magnetic Materials* **310**, 1187–1193 (2007)
- [129] Ernst Ising, “Beitrag zur Theorie des Ferromagnetismus,” *ZS. f. Physik* **31**, 253–258 (1925)

-
- [130] W. Heisenberg, “Zur Theorie des Ferromagnetismus,” *ZS. f. Physik* **49**, 619–636 (1928)
- [131] F. Bloch, “Zur Theorie des Ferromagnetismus,” *ZS. f. Physik* **61**, 206–219 (1930)
- [132] H. Bethe, “Zur Theorie der Metalle,” *ZS. f. Physik* **71**, 205–226 (1931)
- [133] P. W. Anderson, “New Approach to the Theory of Superexchange Interactions,” *Phys. Rev.* **115**, 2 (1959)
- [134] J. Hubbard, “Electron Correlations in Narrow Energy Bands,” *Proc. R. Soc.* **276**, 238 (1963)
- [135] P. W. Anderson, “The Resonating Valence Bond State in La_2CuO_4 and Superconductivity,” *Science* **235**, 1196–1198 (1987)
- [136] A. W. Sandvik, “Finite-size scaling of the ground-state parameters of the two-dimensional Heisenberg model,” *Phys. Rev. B* **56**, 11678 (1997)
- [137] Steven R. White and A. L. Chernyshev, “Neél Order in Square and Triangular Lattice Heisenberg Models,” *Phys. Rev. Lett.* **99**, 127004 (Sep 2007)
- [138] F. Hébert, G. G. Batrouni, R. T. Scalettar, G. Schmid, M. Troyer, and A. Dorneich, “Quantum phase transitions in the two-dimensional hardcore boson model,” *Phys. Rev. B* **65**, 014513 (Dec 2001)
- [139] G. Schmid, S. Todo, M. Troyer, and A. Dorneich, “Finite-Temperature Phase Diagram of Hard-Core Bosons in Two Dimensions,” *Phys. Rev. Lett.* **88**, 167208 (2002)
- [140] S. Yunoki, “Numerical study of the spin-flop transition in anisotropic spin-1/2 antiferromagnets,” *Phys. Rev. B* **65**, 092402–1 (2002)
- [141] G. V. Chester, “Speculations on Bose-Einstein Condensation and Quantum Crystals,” *Phys. Rev. A* **2**, 256–258 (Jul 1970)
- [142] A. J. Leggett, “Can a Solid Be ”Superfluid“?,” *Phys. Rev. Lett.* **25**, 1543–1546 (Nov 1970)
- [143] G. G. Batrouni, R. T. Scalettar, G. T. Zimanyi, and A. P. Kampf, “Supersolids in the Bose-Hubbard Hamiltonian,” *Phys. Rev. Lett.* **74**, 2527–2530 (1995)
- [144] G. G. Batrouni and R. T. Scalettar, “Phase Separation in Supersolids,” *Phys. Rev. Lett.* **84**, 1599–1602 (Feb 2000)

BIBLIOGRAPHY

- [145] Román Orús, Andrew C. Doherty, and Guifré Vidal, “First Order Phase Transition in the Anisotropic Quantum Orbital Compass Model,” *Phys. Rev. Lett.* **102**, 077203 (2009)
- [146] K. Binder, “Theory of first-order phase transitions,” *Rep. Prog. Phys.* **50**, 783 (1987)
- [147] A.W. Sandvik, “Ground-state parameters, finite-size scaling, and low-temperature properties of the two-dimensional S=1/2 XY model,” *Phys. Rev. B* **60**, 6588 (1999)
- [148] Sandro Wenzel, Leszek Bogacz, and Wolfhard Janke, “Evidence for an Unconventional Universality Class from a Two-Dimensional Dimerized Quantum Heisenberg Model,” *Physical Review Letters* **101**, 127202 (2008)
- [149] L. Fritz, R. L. Doretto, S. Wessel, S. Wenzel, S. Burdin, and M. Vojta, “Cubic interactions and quantum criticality in dimerized antiferromagnets,” *Phys. Rev. B* **83**, 174416 (2011)
- [150] Sven E. Krüger, Johannes Richter, Jörg Schulenburg, Damian J. J. Farnell, and Raymond F. Bishop, “Quantum phase transitions of a square-lattice Heisenberg antiferromagnet with two kinds of nearest-neighbor bonds: A high-order coupled-cluster treatment,” *Phys. Rev. B* **61**, 14607 (2000)
- [151] J. Villain, “Spin glass with non-random interactions,” *J. Phys. C: Solid State Phys* **10**, 1717 (1977)
- [152] L. Huijse, *A supersymmetric model for lattice fermions*, Ph.D. thesis, University of Amsterdam (2010), <http://dare.uva.nl/en/record/341605>
- [153] Paul Fendley, Kareljan Schoutens, and Jan de Boer, “Lattice Models with $N = 2$ Supersymmetry,” *Phys. Rev. Lett.* **90**, 120402 (Mar 2003)
- [154] Paul Fendley, Bernard Nienhuis, and Kareljan Schoutens, “Lattice fermion models with supersymmetry,” *Journal of Physics A: Mathematical and General* **36**, 12399 (2003)
- [155] Paul Fendley and Kareljan Schoutens, “Exact Results for Strongly Correlated Fermions in $2 + 1$ Dimensions,” *Phys. Rev. Lett.* **95**, 046403 (2005)
- [156] Liza Huijse, James Halverson, Paul Fendley, and Kareljan Schoutens, “Charge Frustration and Quantum Criticality for Strongly Correlated Fermions,” *Phys. Rev. Lett.* **101**, 146406 (2008)

-
- [157] M. Beccaria and G. F. De Angelis, “Exact Ground State and Finite-Size Scaling in a Supersymmetric Lattice Model,” *Phys. Rev. Lett.* **94**, 100401 (Mar 2005)
- [158] L Huijse, “Detailed analysis of the continuum limit of a supersymmetric lattice model in 1d,” *Journal of Statistical Mechanics: Theory and Experiment* **2011**, P04004 (2011)
- [159] Paul Fendley and Christian Hagendorf, “Exact and simple results for the XYZ and strongly interacting fermion chains,” *Journal of Physics A: Mathematical and Theoretical* **43**, 402004 (2010)
- [160] Paul Fendley and Christian Hagendorf, “Ground-state properties of a supersymmetric fermion chain,” *Journal of Statistical Mechanics: Theory and Experiment* **2011**, P02014 (2011)
- [161] L Huijse, N Moran, J Vala, and Kareljan Schoutens, “Exact ground states of a staggered supersymmetric model for lattice fermions,” Preprint(2011), [arXiv:1103.1368](https://arxiv.org/abs/1103.1368)
- [162] Fred Cooper, Avinash Khare, and Uday Sukhatme, *Supersymmetry in Quantum Mechanics* (World Scientific, 2001)
- [163] Malte Henkel, *Conformal Invariance and Critical Phenomena* (Springer, 1999)
- [164] Ralph Blumenhagen and Erik Plauschinn, *Introduction to Conformal Field Theory With Applications to String Theory*, Lecture Notes in Physics, Vol. 779 (Springer, 2009)
- [165] Daniel Friedan, Zongan Qiu, and Stephen Shenker, “Conformal Invariance, Unitarity, and Critical Exponents in Two Dimensions,” *Phys. Rev. Lett.* **52**, 1575–1578 (1984)
- [166] Pierre Pfeuty, “The one-dimensional ising model with a transverse field,” *Annals of Physics* **57**, 79 – 90 (1970)
- [167] Zongan Qiu, “Nonlocal current algebra and $N = 2$ superconformal field theory in two dimensions,” *Physics Letters B* **188**, 207 – 213 (1987)
- [168] G von Gehlen, V Rittenberg, and T Vescan, “Conformal invariance and correction to finite-size scaling: applications to the three-state Potts model,” *Journal of Physics A: Mathematical and General* **20**, 2577 (1987)

- [169] I Affleck, D Gepner, H J Schulz, and T Ziman, “Critical behaviour of spin-s Heisenberg antiferromagnetic chains: analytic and numerical results,” *Journal of Physics A: Mathematical and General* **22**, 511 (1989)
- [170] Jean-Marc Vanden Broeck and Leonard W. Schwartz, “A One-Parameter Family of Sequence Transformations,” *SIAM Journal on Mathematical Analysis* **10**, 658–666 (1979)
- [171] M N Barber and C J Hamer, “Extrapolation of sequences using a generalized epsilon-algorithm,” *J. Aust. Math. Soc. B* **23**, 229–240 (1982)
- [172] Nicolas Laflorencie, Erik S. Sørensen, Ming-Shyang Chang, and Ian Affleck, “Boundary Effects in the Critical Scaling of Entanglement Entropy in 1D Systems,” *Phys. Rev. Lett.* **96**, 100603 (Mar 2006)
- [173] John Cardy and Pasquale Calabrese, “Unusual corrections to scaling in entanglement entropy,” *Journal of Statistical Mechanics: Theory and Experiment* **2010**, P04023 (2010)
- [174] Maurizio Fagotti and Pasquale Calabrese, “Universal parity effects in the entanglement entropy of XX chains with open boundary conditions,” *Journal of Statistical Mechanics: Theory and Experiment* **2011**, P01017 (2011)
- [175] Steven R. White, Ian Affleck, and Douglas J. Scalapino, “Friedel oscillations and charge density waves in chains and ladders,” *Phys. Rev. B* **65**, 165122 (2002)
- [176] L Huijse, private communication.
- [177] Carsten Honerkamp and Walter Hofstetter, “Ultracold Fermions and the $SU(N)$ Hubbard Model,” *Phys. Rev. Lett.* **92**, 170403 (Apr 2004)
- [178] M A Cazalilla, A F Ho, and M Ueda, “Ultracold gases of ytterbium: ferromagnetism and Mott states in an $SU(6)$ Fermi system,” *New Journal of Physics* **11**, 103033 (2009)
- [179] A. V. Gorshkov, M. Hermele, V. Gurarie, C. Xu, P. S. Julienne, J. Ye, P. Zoller, E. Demler, M. D. Lukin, and A. M. Rey, “Two-orbital $SU(N)$ magnetism with ultracold alkaline-earth atoms,” *Nat Phys* **6**, 289–295 (04 2010)
- [180] Robert Jordens, Niels Strohmaier, Kenneth Gunter, Henning Moritz, and Tilman Esslinger, “A Mott insulator of fermionic atoms in an optical lattice,” *Nature* **455**, 204–207 (09 2008)

-
- [181] U. Schneider, L. Hackermüller, S. Will, Th. Best, I. Bloch, T. A. Costi, R. W. Helmes, D. Rasch, and A. Rosch, “Metallic and Insulating Phases of Repulsively Interacting Fermions in a 3D Optical Lattice,” *Science* **322**, 1520–1525 (2008)
- [182] E. V. Gorelik and N. Blümer, “Mott transitions in ternary flavor mixtures of ultracold fermions on optical lattices,” *Phys. Rev. A* **80**, 051602 (Nov 2009)
- [183] Shin-ya Miyatake, Kensuke Inaba, and Sei-ichiro Suga, “Three-component fermionic atoms with repulsive interaction in optical lattices,” *Phys. Rev. A* **81**, 021603 (Feb 2010)
- [184] Andreas Läuchli, Frédéric Mila, and Karlo Penc, “Quadrupolar Phases of the $S = 1$ Bilinear-Biquadratic Heisenberg Model on the Triangular Lattice,” *Phys. Rev. Lett.* **97**, 087205 (Aug 2006)
- [185] N. Papanicolaou, “Unusual phases in quantum spin-1 systems,” *Nuclear Physics B* **305**, 367 – 395 (1988)
- [186] Ian Affleck and J. Brad Marston, “Large- n limit of the Heisenberg-Hubbard model: Implications for high- T_c superconductors,” *Phys. Rev. B* **37**, 3774–3777 (Mar 1988)
- [187] J. Brad Marston and Ian Affleck, “Large- n limit of the Hubbard-Heisenberg model,” *Phys. Rev. B* **39**, 11538–11558 (Jun 1989)
- [188] Michael Hermele, Victor Gurarie, and Ana Maria Rey, “Mott Insulators of Ultracold Fermionic Alkaline Earth Atoms: Underconstrained Magnetism and Chiral Spin Liquid,” *Phys. Rev. Lett.* **103**, 135301 (2009)
- [189] Tamás A. Tóth, Andreas M. Läuchli, Frédéric Mila, and Karlo Penc, “Three-Sublattice Ordering of the $SU(3)$ Heisenberg Model of Three-Flavor Fermions on the Square and Cubic Lattices,” *Phys. Rev. Lett.* **105**, 265301 (Dec 2010)
- [190] Ian Affleck, Tom Kennedy, Elliott H. Lieb, and Hal Tasaki, “Rigorous results on valence-bond ground states in antiferromagnets,” *Phys. Rev. Lett.* **59**, 799 (1987)
- [191] A. Kitaev, “Fault-tolerant quantum computation by anyons,” *Ann. Phys.* **303**, 2 (2003)
- [192] Paolo Zanardi and Nikola Paunković, “Ground state overlap and quantum phase transitions,” *Phys. Rev. E* **74**, 031123 (Sep 2006)

BIBLIOGRAPHY

- [193] Tobias J. Osborne and Michael A. Nielsen, “Entanglement in a simple quantum phase transition,” *Phys. Rev. A* **66**, 032110 (Sep 2002)
- [194] A. Osterloh, Luigi Amico, G. Falci, and Rosario Fazio, “Scaling of entanglement close to a quantum phase transition,” *Nature* **416**, 608–610 (04 2002)
- [195] C.W. Helstrom, *Quantum Detection and Estimation Theory* (Academic, 1976)
- [196] C.A. Fuchs and J. van de Graaf, “Cryptographic distinguishability measures for quantum-mechanical states,” *IEEE Trans. Inf. Theory* **45**, 1216 (1999)
- [197] Jan Ivar Korsbakken, K. Birgitta Whaley, Jonathan Dubois, and J. Ignacio Cirac, “Measurement-based measure of the size of macroscopic quantum superpositions,” *Phys. Rev. A* **75**, 042106 (2007)
- [198] K. M. R. Audenaert, J. Calsamiglia, R. Muñoz Tapia, E. Bagan, Ll. Masanes, A. Acín, and F. Verstraete, “Discriminating States: The Quantum Chernoff Bound,” *Phys. Rev. Lett.* **98**, 160501 (2007)
- [199] Andreas Läuchli, Guido Schmid, and Simon Trebst, “Spin nematic correlations in bilinear-biquadratic $S=1$ spin chains,” *Phys. Rev. B* **74**, 144426 (2006)
- [200] I. Affleck, T. Kennedy, E.H. Lieb, and H. Tasaki, “Valence Bond Ground States in Isotropic Quantum Antiferromagnets,” *Commun. Math. Phys.* **115**, 477–528 (1988)
- [201] Daniel P. Arovas, Assa Auerbach, and F. D. M. Haldane, “Extended Heisenberg models of antiferromagnetism: Analogies to the fractional quantum Hall effect,” *Phys. Rev. Lett.* **60**, 531 (1998)
- [202] S.M. Girvin and D.P. Arovas, “Hidden topological order in integer quantum spin chains,” *Phys. Scr.* **T27**, 156 (1989)
- [203] J. Sólyom, “Competing bilinear and biquadratic exchange couplings in spin-1 Heisenberg chains,” *Phys. Rev. B* **36**, 8642–8648 (Dec 1987)
- [204] C Castelnovo, S Trebst, and M Troyer, “Topological Order and Quantum Criticality,” in *Understanding Quantum Phase Transitions*, edited by L. D. Carr (CRC Press, 2010)
- [205] D. Stauffer and A. Aharony, *Introduction to Percolation Theory* (Taylor & Francis, 1994)

- [206] Makoto S. Watanabe, “Percolation with a periodic boundary condition: The effect of system size for crystallization in molecular dynamics,” *Phys. Rev. E* **51**, 3945–3951 (May 1995)

BIBLIOGRAPHY

Curriculum Vitae

Personal data

Name: Roman Bela Bauer
Date of birth: 16.07.1984
Place of birth: Cologne, Germany
Nationality: German

Education

1994-2000 Hildegard-von-Bingen-Gymnasium, Cologne, Germany
2000-2002 Ridley College, Ontario, Canada
Graduated with Ontario Secondary School Diploma
2003-2005 Undergraduate studies University of Leipzig, Germany
Vordiplom
2005-2008 Undergraduate studies ETH Zurich, Switzerland
2008 Diploma thesis at ETH Zurich
"Infinite projected entangled-pair states"
2008-2011 Graduate student at ETH Zurich
in the group of Prof. M. Troyer

Acknowledgements

I'd like to start by thanking my supervisor Matthias Troyer – for pointing me at such an interesting project, for bringing me into contact with so many collaborators, and for his continuous support.

Of course many collaborations have been important for this thesis. But more than to anyone, I'm indebted to Guifré Vidal and Frank Verstraete for sharing innumerable ideas and suggestions. Without your help and suggestions, none of this work would have been possible. And of course thanks for your hospitality when I visited Brisbane and Vienna!

Philippe and Román, I am very much indebted to you for including me in the project about fermions – I still have a lot to make up for that. And of course thanks for all other collaborations and discussions.

I'd like to thank my other collaborators on the projects that make up this thesis: Koni Marti and Markus Reiher on quantum chemistry, Vito Scarola and Hao Wang on indistinguishability, Liza Huijse and Kareljan Schoutens on the supersymmetric lattice fermions, and Adrian Kantian, Alex Kosenkov, Timothée Ewart and Michele Dolfi on the HP2C DMRG code, and Frédéric Mila and Andreas Läuchli on the SU(3) Heisenberg model.

One of the great experiences in working with tensor network states is the open and welcoming community. My particular thanks to David Pérez-García, Ulrich Schollwöck, Ignacio Cirac, Mari-Carmen Bañuls, and Tao Xiang for their hospitality. I've enjoyed valuable discussions with many people, including Thomas Barthel, Garnet Chan, Andrew Daley, Jens Eisert, Glen Evenbly, Adrien Feiguin, Jacob Jordan, Fabian Heidrich-Meissner, Valentin Murg, Tomotoshi Nishino, Norbert Schuch, Steve White.

Much of my work during the last years has not become part of this thesis. I'd like to thank my collaborators on the Optimized Ensembles, Emanuel Gull, Simon Trebst and David Huse, and the VisTrails team, in particular David Koop, Emanuele Santos, Claudio Silva, Juliana Freire. I'd also like to thank the whole ALPS collaboration for their efforts.

And then, to my officemates, Brigitte, Lukas, Sebastiano – thanks for always having an open ear for my little problems and questions and for the daily cof-

fee break discussions about C++ and Swiss politics! And of course thanks to the rest of the group (and its former members, and the other groups) – Adrien, Andreas, Christian, Emanuel, Jan, Juan-Carlos, Lode, Martin, Mingqi, Naoto, Peter, Philipp, Ruben, Sergei, Tama, Zhenya – for making my time at ETH enjoyable.

Und die Wichtigsten am Ende: Mein größter Dank gilt selbstverständlich meiner Familie für ihre Unterstützung und Kristina für ihre Geduld.